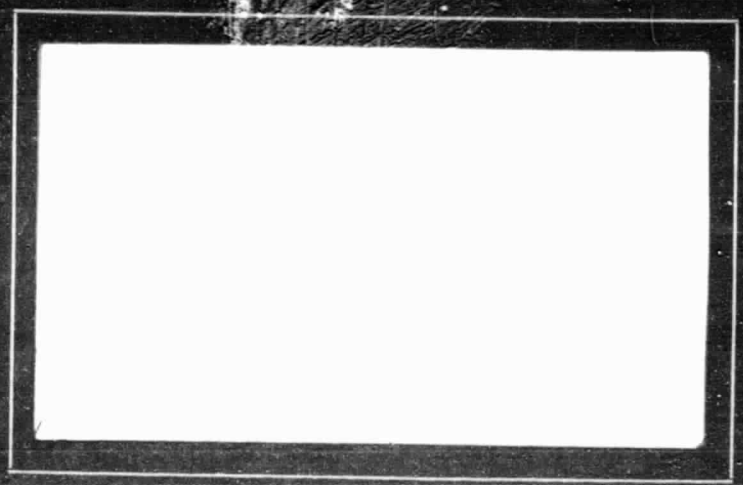

RENSSELAER POLYTECHNIC INSTITUTE

KNOWLEDGE AND THOROUGHNESS

1824

Rensselaer Polytechnic Institute

Troy, New York 12181

INVESTIGATION OF PASSIVE SHOCK WAVE-BOUNDARY LAYER CONTROL FOR TRANSONIC AIRFOIL DRAG REDUCTION

FINAL REPORT

for the period
October 1, 1979 to September 30, 1981

NASA Grant No. NSG 1624

NASA Langley Research Center

by

H.T. Nagamatsu, W.B. Brower, Jr.,
L. Bahi and J. Ross
Department of Mechanical Engineering
Aeronautical Engineering & Mechanics
Rensselaer Polytechnic Institute
Troy, N.Y. 12181

April 1982

TABLE OF CONTENTS

Page

LIST OF TABLES

LIST OF FIGURES

LIST OF SYMBOLS

A	Area cross section
A^*	Minimum area cross section
a	Speed of sound
c	Chord of airfoil
C_p	Pressure coefficient
C_d	Section drag coefficient, $\int_{wake} C_{d'} d(h/c)$
$C_{d'}$	Point drag coefficient
c_p	Specific heat at constant pressure
c_v	Specific heat at constant volume
h	Vertical distance in wake profile
M	Mach number, u/a
P	Static pressure
R_e	Reynolds number
S	Entropy per unit mass
T	Absolute temperature
t	thickness of airfoil
u	speed of flow
x	Abscissa measured along airfoil reference line from airfoil leading edge, or axial distance
y	Vertical distance
z	Ordinate measured normal to airfoil reference line
z_c	Ordinate of airfoil mean line
ρ	Density of flow
ν	Kinematic viscoty

μ	Viscosity
δ	Boundary layer thickness
δ^*	Boundary layer displacement thickness
γ	Ratio of specific heats, c_p/c_v
β	Shock wave angle measured from upstream flow direction
θ	Angle of flow deflection across an oblique shock wave
l	Lower surface
u	Upper surface
o	Total conditions
1	Conditions just upstream of a shock wave
2	Conditions just downstream from a shock wave
∞	Free stream conditions

ACKNOWLEDGMENT

The work presented here was sponsored by NASA Langley Research Center, contract No. NG 1624, under the direction of Mr. Charles Harris and Dr. Richard Barnwell to whom we express our gratitude for their discussions and advices. Mr. Dennis Bushnell and Dr. Richard Whitcomb, who suggested the investigation of the passive drag reduction concept, are acknowledged.

ABSTRACT

An investigation of the passive shock wave/boundary layer interaction control aiming at reducing the drag for conventional and supercritical airfoils at transonic Mach numbers is presented. A 3x 15.4-inch Transonic Wind Tunnel was designed, constructed and calibrated to achieve this objective. Modifications were made in the initial constant area test section to accomodate for the boundary layer growth along the tunnel walls. The boundary layer of the test section bottom wall was removed via a bleed system, so that the new boundary layer began at the airfoil leading-edge stagnation point. A variable porosity test section top wall was used to minimize the wall interference. A manometer board and a Schlieren system were contructed to measure the pressures and obtain Schlieren photographs of the flow field over the different airfoils in the test section.

The passive drag control concept, consisting of a porous surface with a cavity beneath it, was investigated with a 12-percent-thick circular arc and a 14-percent-thick supercritical airfoil mounted on the test section bottom wall. The porous surface was positioned in the shock wave/boundary layer interaction region. the flow circulating through the porous surface, from the downstream to the upstream of the terminating shock wave location, produced a lambda shock wave system and a pressure decrease in the downstream region minimizing the flow separation. The wake impact pressure data showed an appreciably drag reduction with the porous surface at transonic speeds. To determine the optimum size of porosity and cavity, tunnel tests were conducted

with different airfoil porosities, cavities and flow Mach numbers. A higher drag reduction was obtained by the 2.5 percent porosity and the 1/4-inch deep cavity.

PART 1

INTRODUCTION

The increasing cost and future scarcity of fuel for transport and military aircraft create an urgent need to reduce fuel consumption and increase aircraft performance through refinements in aerodynamics, lighter materials, and more efficient jet engines. Several methods of reducing fuel consumption and improving performance are either being planned or under study for existing and future aircraft. The reduction of wing drag is a logical method of achieving this goal, especially at the transonic cruise speeds of jet aircraft.

In this transonic flight regime, where complex nonlinear effects tend to dominate the flow, a dramatic increase in the drag takes place as the drag divergence Mach number is reached. The most common description of a transonic flow is when there is a supersonic "bubble" totally imbedded in a subsonic flow. The supersonic bubble may be terminated by a shock wave producing wave drag, or in certain circumstances, may return to subsonic conditions through an isentropic compression with no wave drag. This wave drag is associated with the increase in entropy across the shock wave. Soon after a shock wave appears in the flow, the drag will increase rapidly with increasing free-stream Mach number leading to the "drag rise Mach number," which is defined as the free-stream Mach number at which this rapid drag rise begins. One of the main objectives of designing a wing for transonic speeds is to obtain as high a "drag rise Mach number" as possible, subject to certain constraints.

The obvious way to reduce the wave drag, at least in the 2-

dimensional case, is to use a supercritical shock-free airfoil section[1] where there is no shock wave and consequently, no wave drag. However, these shock-free airfoils may have undesirable off-design characteristics, such as strong shock waves suddenly appearing when the Mach number is perturbed slightly from its design value. Thus, an important constraint in the design of airfoils is that there should be good off-design behavior.

In wing design with 3-dimensional flow, the design can be altered by spanwise changes in the sweep and twist. This process, however, complicates the design procedure. In principle, the supercritical airfoils are shaped to reduce the drag associated with energy losses caused by shock waves and flow separation, but still there is no generally applicable technique available which gives a net reduction of the total drag at transonic speeds.[2]

For the thick, supercritical airfoils for the proposed flying load-carrying wing with airfoil thickness of 20 to 25 percent of the chord, the increase in the drag at transonic flight Mach numbers is more severe than for the thinner (approximately 10-percent-thick) supercritical airfoil wing. The drag of such a thick wing is reasonably low at the design lift coefficient and Mach number, but the drag increases at higher lift coefficients and Mach number because of the strong shock waves which terminate the imbedded supersonic region.

In the case of fighter aircraft, the performance envelope for maneuvering is limited by the onset of buffet at high subsonic Mach numbers, which is caused by severe unsteady shock wave/boundary layer inter-

action and its effects on the shock wave location. The termination shock waves for the imbedded supersonic regions are very strong at high angles of attack and cause the boundary layer to separate from the wing.

To control the drag increase due to the shock wave/boundary layer interaction for conventional airfoils and for thin and thick supercritical airfoils at transonic Mach numbers, a basic research program on the passive shock wave/boundary layer control for drag reduction was suggested by Mr. Dennis Bushnell and Dr. Richard Whitcomb at the NASA Langley Research Center. The concept of the passive drag reduction consists of having a porous surface with a cavity underneath at the shock wave location. The high pressure downstream of the shock wave will force some of the boundary layer flow into the cavity and out ahead of the shock wave. By this method, the boundary layer will thicken ahead of the shock wave and send compression waves into the supersonic region, thereby decreasing the Mach number for the normal shock wave. By this shock wave/boundary layer interaction process, the increase of entropy across the shock wave will be lower and the boundary layer flow separation will be minimized. Both of these effects tend to decrease the drag at transonic speeds.

In recent experiments on the supersonic jet noise reduction, Maestrello[3] used a porous centerbody plug nozzle jet with a porosity of about 2 percent to eliminate the shock waves for transonic and supersonic jet exhaust velocities. This method provided a shock free flow without the "shock associated noise" and "screeching" and significantly reduced the jet noise. These results were encouraging and indicated the possi-

bility of minimizing the shock wave losses over the airfoils at transonic Mach numbers by placing a porous surface with a cavity underneath the shock wave location.

The effects of surface humping and chordwise slots on the shock waves over supercritical airfoils at transonic Mach numbers were investigated by Lee and Yoshihara.[4] The purpose of the investigation was to decrease the adverse effects of shock wave/boundary layer interaction on severe buffeting at transonic maneuvering flight conditions. Preliminary results did indicate a change in the strength and location of the shock waves, with a slotted configuration showing greater effects. Airfoil static pressure distributions and Schlieren photographs were obtained at transonic Mach numbers and different angles of attack, but no drag measurements were taken for these two concepts.

Other investigators have studied the effects of injection and suction on the control of turbulent boundary layers through transverse and longitudinal slots, holes, and porous plates at subsonic Mach numbers over airfoils. Wilkinson[5] investigated the effects of suction on the incompressible turbulent boundary layer through closely spaced streamwise slots. His drag and mean boundary layer velocity profile measurements showed that the slotted surface had nominally the same suction characteristics as the porous surface. A comprehensive list of references on the effects of suction and injection on the turbulent boundary layer is presented in Ref. 5.

Another technique of reducing the drag at subsonic Mach numbers is laminar boundary layer control, which keeps the flow laminar.

This can be achieved by using different approaches. These include suction, favorable pressure gradient, wall cooling for gases, wall heating for liquids, MHD forces, and compliant walls. Among these approaches, the most promising one is laminar flow control by the use of suction, and suction through porous strips seems to be most appropriate.[6]

Recent advances in computational aerodynamics have made it possible to compute many nonlinear problems, such as the special solution for shock wave/boundary layer interaction flow over airfoils by Nandanan et al.[7] However, this analysis did not include the separation of the boundary layer and the experiments showed the need for the correct treatment of the shock wave/boundary layer interaction in transonic flow. The strong viscous interaction between the shock wave and the boundary layer in the transonic region of mixed subsonic and supersonic flow is still not adequately modeled. Despite some pioneering efforts, the development of methods for calculating the separated flow is still in its infancy. For this, we can refer to one of the techniques in Ref. 8, which presents the calculation of the interaction of the inviscid external flow and the separated boundary layer. The method has been applied to the flow field over a symmetric, biconvex airfoil at zero angle of attack, but has yet to be verified for the lifting airfoils.

Investigations of the shock wave/boundary layer interaction over supercritical airfoils to improve the theoretical analysis capability for airfoils experiencing strong inviscid-viscous flow interactions are being conducted at the Lockheed-Georgia Company[9] and at the NASA Ames Research Center.[10] Because of the trend toward designing thicker and more

highly-loaded airfoils for transport aircraft cruising at transonic speeds, it has become increasingly difficult to predict the performance of these airfoils.

Because of the lack of experimental data and other urgent needs for decreasing aircraft fuel consumption and improving aerodynamic efficiency, the present basic concept of drag reduction has been investigated mostly through experimental studies. The purpose of the research was to investigate the possibility of drag reduction for supercritical airfoils by applying the concept of the passive shock wave/boundary layer control. The experimental investigation was established to satisfy specific objectives which have provided basic information about advanced supercritical airfoil wing design and the passive drag reduction concept over transonic airfoils. These objectives are as follows: (1) to define the flow field for the shock wave/boundary layer interaction over the bottom surface of the transonic wind tunnel, which simulates the supercritical airfoil pressure distribution with a solid surface; (2) to determine the surface pressure distribution and the total drag from the impact surveys with a solid surface; (3) to study the effects of the surface porosity at the shock wave/boundary layer interaction region on the flow field and the total drag from the impact pressure surveys; (4) to investigate the effects of the size of the cavity located below the porous surface on the flow field and the drag; (5) to determine the total drag from wake impact surveys and the flow field at transonic Mach numbers; (6) to study the effect of humidity on the drag reduction and the pressure distribution. Schlieren photographs for the optical information were ob-

tained to define the shock waves with and without the porous surface for the passive drag control concept.

To conduct this research, a blowdown transonic wind tunnel with an atmospheric intake was constructed using the existing dryer, vacuum tank and vacuum pumps used for the Mach 3 Wind Tunnel at Rensselaer Polytechnic Institute. A pressure measuring system, optical instrumentation, and different models were designed, constructed and used to calibrate the flow in the test section. A preliminary mahogany test section with constant area was used and modifications were made to obtain nearly uniform flow over the region where the airfoil model was located. Both Schlieren photographs and pressure distributions over a 10-percent-thick double wedge and 12-percent-thick biconvex airfoils were obtained with the models mounted in the center of the test section. Similar data were obtained with a 3-inch chord circular arc airfoil mounted on the bottom surface of the test section. The details of these preliminary experimental results are presented in Ref. 11. An aluminum test section was later designed and constructed to investigate the concept of the passive drag control. The design of this test section was based on the knowledge gained from the initial mahogany test section, and modifications were made to overcome the observed shortcomings. A 4-inch chord circular arc airfoil and a NASA 14-percent-thick supercritical airfoil (Ref. 12), were investigated in this new aluminum test section with an adjustable porous top wall to study the effects of the porous surface and the cavity size on the shock wave/boundary layer interaction. Schlieren photographs, pressure data and impact pressure wake surveys were obtained at subsonic and transonic speeds.

PART 2

EXPERIMENTAL FACILITY

2.1 Transonic Wind Tunnel

A 3-inch by 15.4 inch transonic wind tunnel was constructed parallel to the existing 4-inch by 4-inch Mach 3 Wind Tunnel to investigate the possibility of reducing the drag of the supercritical airfoils by the application of the concept of the passive shock wave/boundary layer control. The various components of the Transonic Wind Tunnel[11] are discussed below and Figs. 1 and 2 show the overall arrangement of the tunnel.

2.1.1 Entrance Section and Settling Chamber

A rectangular cross section settling chamber with a height of 33.9 inches, a width of 20 inches, and a length of 48 inches was constructed from 0.75 inch thick birch plywood. To smooth the entering airflow, a bellmouth was attached to the entrance of the settling chamber and to the wall of the dryer as shown in Fig. 1.

A honeycomb with a depth of 6 inches and hexagonal flow passages of approximately 0.25 inch was placed at the entrance of the settling chamber as shown in Fig. 1. Fine screens were placed in front and back of the honeycomb section to break up the large eddies into small sizes and to make the flow uniform across the settling chamber. The length of the settling chamber was selected to permit the decay of the small scale turbulent eddies before the flow was accelerated in the contraction section. After the initial tests, another layer of birch ply-

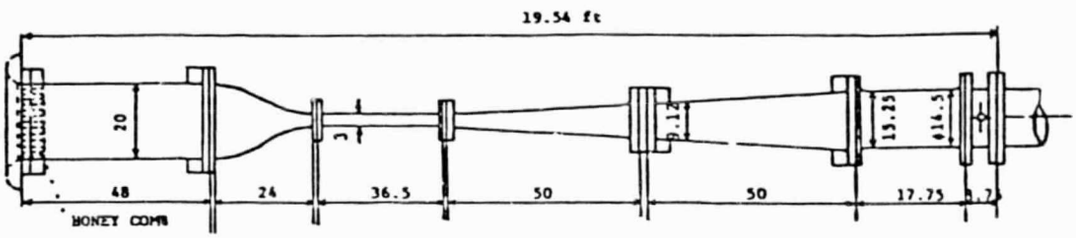

Top view

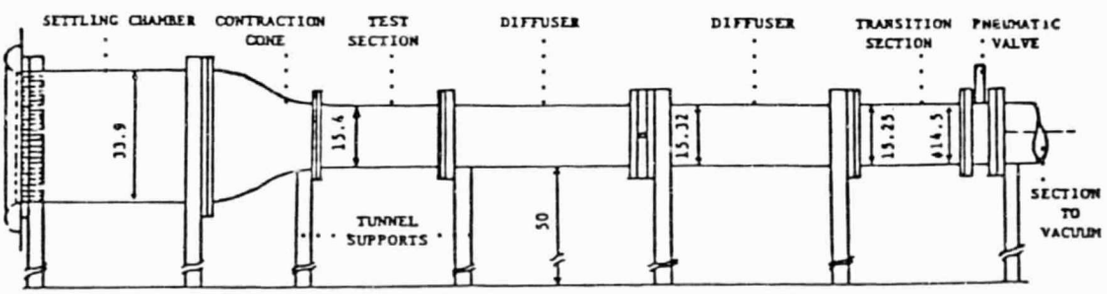

Side view

Fig.1 Scale drawing of 3x15.4 inch Transonic Wind Tunnel

ORIGINAL PAGE
BLACK AND WHITE PHOTOGRAPH

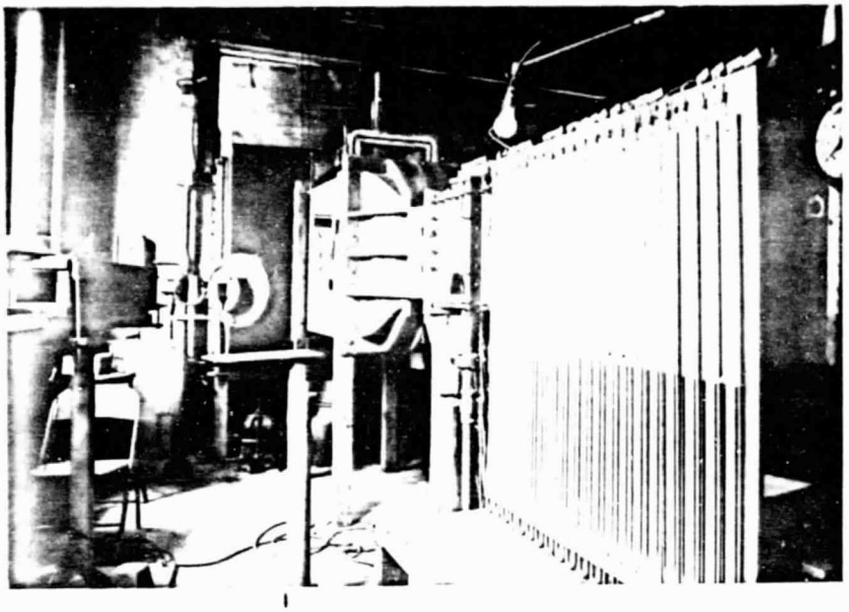

Fig.2a Transonic Wind Tunnel

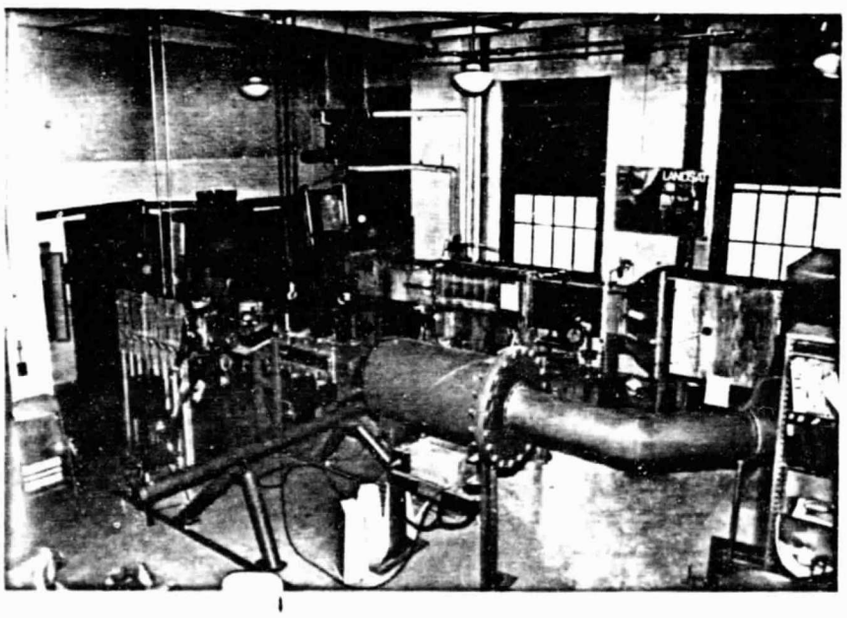

Fig.2b Mach 3 and Transonic Wind Tunnels

wood was added to the settling chamber walls to strengthen the rigidity of the section.

2.1.2 Contraction Section

The dimensions of the entrance to the contraction section were 20 inches wide and 33.9 inches high, and at the exit the corresponding dimensions were 3 inches and 15.4 inches as shown in Fig. 1. A gradual contraction shape was selected towards the exit of the section to achieve uniform flow across the cross section. Multiple layers of thin aircraft plywood, glued together with epoxy, were used to obtain the desired contours for the contraction section. Longitudinal ribs were used to stiffen the plywood pieces as shown in Figs. 1 and 2, and later on epoxy filler was added on the sides of the contraction section exit to make it more rigid. The inside walls were carefully sanded and varnished to produce smooth surfaces for the air to accelerate from low speed to transonic speed at the end of the contraction section.

2.1.3 Test Section

The dimensions of the original test section were 3 inches wide and 15.4 inches high with a length of 36.5 inches as shown in Fig. 3a. For the initial calibration tests, solid mahogany pieces were used for the top and bottom surfaces so as to simplify the changes for these surfaces. The test section had been modified to accommodate for the boundary layer growth in the test section by opening the top and bottom walls at the exit by 0.7 inch and the side walls by 0.15 inch as shown in Fig. 3b. The initial 20 inches of the bottom and top walls were parallel to

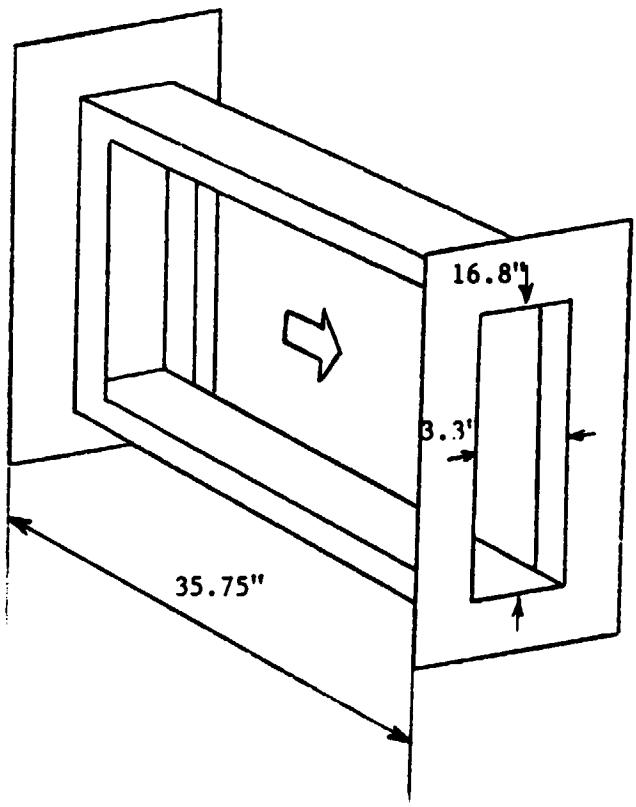

Fig.3a Original test section

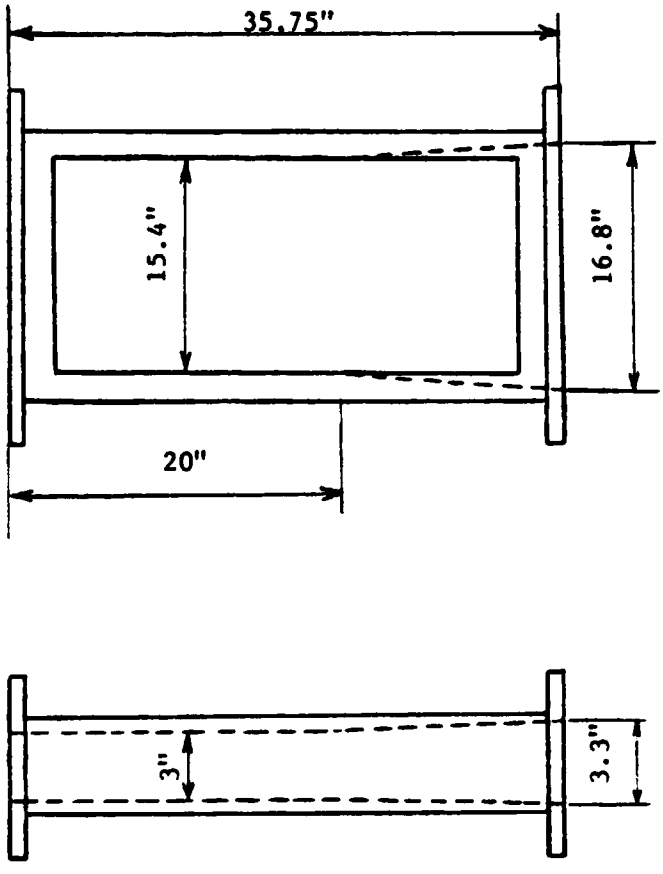

Fig.3b Modified test section

the tunnel axis. For the initial flow field investigation, airfoils were placed in the middle of the flat bottom surface. Later, an aluminum porous wall test section was designed and constructed, cf. Fig. 4. Its design was based on the knowledge gained from the initial mahogany test section.

Although blockage effects are produced in most two-dimensional wind tunnel testings, the full impact of their presence is very evident in the transonic regime. When the free stream Mach number approaches unity, a slight change in area ratio produces a large change in the Mach number. This happens when a model is placed in a test section operating in the transonic regime.

For several years, slotted or perforated test section walls have been proposed to overcome these difficulties.[11] In our aluminum test section, attempts at reducing or eliminating the model blockage effects at transonic speeds have been made through the design and construction of an adjustable porous top wall test section.[13]

In the middle of the flat bottom surface of the test section, a 4-inch chord circular arc and a 14-percent-thick supercritical airfoil with the porous surface and cavity located below the shock wave/boundary layer interaction region, were placed and investigated.

Thick lucite side walls were used to permit the observation of the shock waves and the flow field over the top surface of the circular and supercritical airfoils. Aluminum plates on both side walls were used to minimize the wall deflection. A circular cut was made in the aluminum plates for the optical information. With this arrangement, it

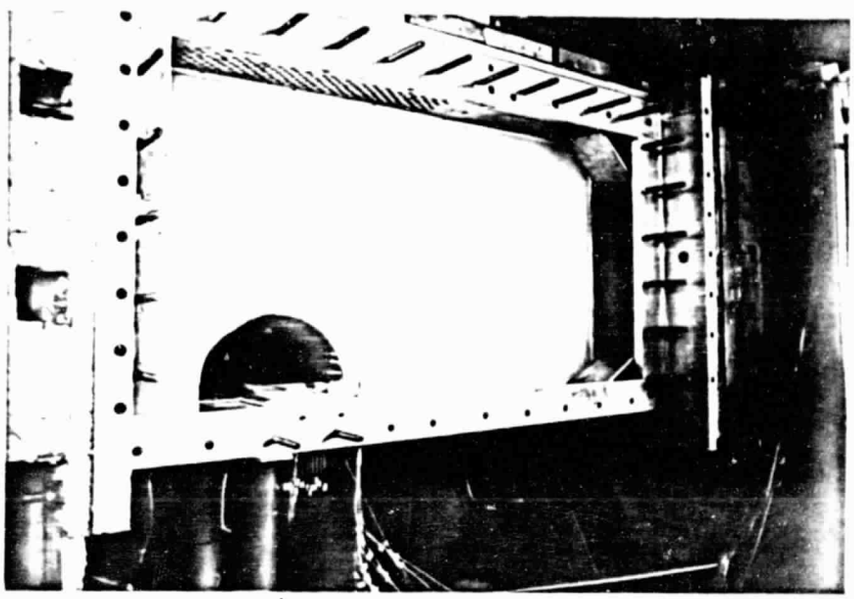

Fig.4 Side view of aluminum test section

was possible to study the shock wave/boundary layer interaction phenomena with and without the passive porous surface for the circular arc and supercritical airfoils over a range of free stream Mach numbers.

The test section boundary layer on the bottom wall was removed via a separate bleed system, so that the new boundary layer would begin at the airfoil leading-edge stagnation point. The boundary layer removal system consisted of a 3-inch transverse slot located at the model leading edge. A 2-inch diameter pipe connected the bleed slot to the vacuum system downstream of the wind tunnel. The removal of the boundary layer, Fig. 8b, was established by opening a valve separating the vacuum inside the pipe from the air flow in the test section at the start of the test.

Two adjustable wedges, one on the bottom surface of the test section and the other on the top, were used to vary the free stream Mach number from low subsonic to transonic speeds as shown in Fig. 3b. This technique of controlling the Mach number in the test section has been effective.

2.1.4 Diffuser Section

The diffuser section consisted of two 50-inch long diverging ducts as shown in Figs. 1 and 2. The original cross section at the entrance was 3 inches by 15.4 inches and these dimensions were increased to 3.3 inches and 16.8 inches as a result of the modifications in the test section, Fig. 3b. The dimensions at the exit of the diffuser were 15.25 inches by 15.25 inches. Two layers of 0.75-inch thick birch plywood were used to construct the diffuser sections in order to withstand the pressure differential across the diffuser surface and to minimize

the noise from the transition shock waves. Between the two diffuser sections a manual control valve was installed as shown in Figs. 1 and 2 to control the free stream Mach number. However, a better control of the Mach number was obtained with the two adjustable wedges at the exit of the test section as shown in Fig. 3b. The test results with transonic flow in the test section have indicated satisfactory performance of the diffuser to meet the design objectives.

A plywood transition piece was constructed to connect the square diffuser exit cross section to a circular 14.5-inch diameter cross section ahead of the quick acting 16-inch diameter pneumatic valve as shown in Figs. 1 and 2. The transition from the square to circular cross section was accomplished by an octagonal section.

2.1.5 Quick Acting Pneumatic Valve

To start the flow through the transonic wind tunnel, a 16-inch diameter quick acting pneumatic valve was mounted between the end of the diffuser section and the flange for the 16-inch diameter vacuum pipe as shown in Figs. 1 and 2. A large 6-inch diameter pneumatic cylinder was attached to the valve for quick opening. House air supply at a pressure of 120 psi was connected to the 6-inch diameter cylinder through a 110-volt solenoid valve. This valve was actuated by a key mounted next to the manometer board, cf. Figs. 1 and 2, to open and close the 16-inch diameter valve rapidly. Tests had confirmed the fast opening and closing of the valve. A timing circuit had been installed to control the valve opening and closing as well as to close the valves on the manometer board for measuring the pressure after a desired flow duration. In the closed

position with 120 psia pressure on the control cylinder, the large valve sealed with practically no leakage to the vacuum tank.

2.1.6 Vacuum System

Six vacuum pumps with 5-hp electric motors were used to evacuate the large vacuum tank located adjacent to the laboratory. All of these pumps could be used simultaneously to evacuate the tank, and could be left operating during a test. It was possible to evacuate the tank to 29.5 inches of mercury pressure difference in a short time.

The Mach 3 Wind Tunnel with a square test section of 4 inches, located parallel to the Transonic Tunnel, as shown in Fig. 2b, utilized the same vacuum system. The discharge from both of these tunnels was connected to the 16-inch diameter pipe.

2.1.7 Air Dryer

The Transonic Tunnel was attached to a large cross section silica gel dryer as shown in Figs. 1 and 2. A sliding door was opened to permit the outside air to go through the dryer before entering the Transonic or the Mach 3 Wind Tunnels. Heating elements were installed to heat the recirculating air through the silica gel bed to 300°F for reactivation. After the silica gel bed was reactivated, a water-cooled heat exchanger was used to bring the bed temperature to ambient conditions.

2.2 Instrumentation

2.2.1 Pressure Apparatus

A mercury manometer board was constructed with 20 U-tubes to

measure the static pressures at various locations along the Transonic Wind Tunnel and over the airfoil models. The same manometers were used to measure the impact pressure from the rake for the wake survey and the total pressure from an impact pressure probe installed in the settling chamber ahead of the contraction section. The free stream Mach number was obtained by taking the average of the vertical static pressures measured on the side of the entrance of the test section ahead of the airfoil model location. Ball valves were used with the U-tubes for the initial calibration of the wind tunnel but the valves were later replaced by an electrically timed solenoid valve system, which is discussed later. The valves were opened before the flow was started and were closed by the timer after the steady pressure was established. Plastic tubing was used to connect the static pressure orifices in the tunnel and over the models to the valves attached to the U-tubes.

2.2.2 Boundary Layer Survey Apparatus

The boundary layer thickness along the side wall and the bottom surface of the initial test section was measured with a small impact pressure probe. The diameter of the stainless steel probe was 0.063 inch with an inside diameter of 0.0365 inch. This probe was attached to a micrometer in order to accurately determine the distance of the impact pressure probe from the tunnel surface. The boundary layer thickness was measured at three axial locations for the side wall and the bottom surface.

2.2.3 Wake Survey Apparatus

A single impact pressure probe was initially used to survey

the wake downstream of the airfoil model. Because of its bending in the flow when the flow was established, it was replaced by a thick rake with ten impact pressure probes. The average probe spacing was 0.181 inch and the average length from the probe centerline was 0.5 inch. The diameter of the stainless steel probe was .039 inch. The rake centerline was located 1.75 inches downstream of the model trailing edge. Later the thick rake was replaced by a thin one to minimize the blockage effect. The thin rake had 8 impact pressure probes with 0.031 inch inside and 0.040 inch outside diameters. The average probe spacing was 0.127 inch. The location on the bottom wall test section was the same as for the thick rake. The survey of the wake was done through a height of 1.70 inches from the bottom surface. The rake taps were connected to the mercury manometer board for measuring the impact pressures within the wake.

2.2.4 Optical System

The optical system was a conventional single-pass Schlieren system consisting of a focussed zirconium light source, two 7.5 inch diameter parabolic mirrors with a focal length Of 5.0 feet, two 9.5 inch diameter flat mirrors, an adjustable knife edge at the focal point, and a film plate holder. A schematic of this optical system is shown in Fig. 5. With this system, it was possible to obtain both Schlieren and shadowgraph photographs of the shock wave and the flow field over airfoil models in the test section. The shadowgraph photographs were taken with the focal plane shutter camera placed next to the test section window. In this report, mainly the Schlieren photographs will be presented.

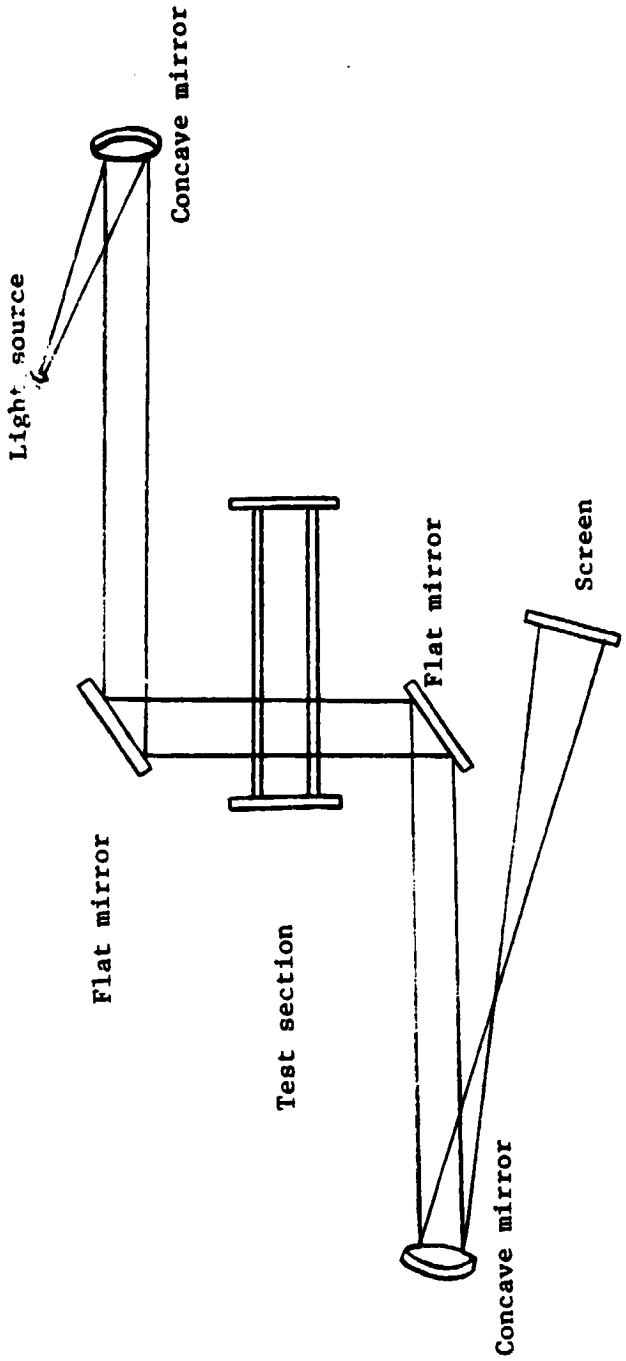

Fig.5 Schematic of the Schlieren optical system

2.2.5 Solenoid Valves and Timer System

Twenty small electrical solenoid valves were used instead of the previous ball valves at the manometer board as shown in Fig. 2. They were normally opened before the flow was started and closed automatically through the use of an adjustable electrical delay timer. At the same time the valves were closed, the timer activated the camera shutter for the Schlieren system.

2.2.6 Temperature Gage

A temperature probe was installed in the settling chamber to measure the total temperature of the flow. The probe was connected to an electronic digital display system which read the temperature and displayed it on a small screen. The temperature gage was connected to the timer system. The temperature was taken at the same time when the valves for the pressure were closed and the camera shutter activated. By this system, the pressures, temperature and the Schlieren photographs were taken at the same test time.

2.2.7 Humidity Gage

A humidity gage was installed in the wall of the dryer chamber. An opening made on the dryer wall allowed the air to flow inside the gage for the readings. The relative humidity was in the ideal range for most of the tests. After the dryer was reactivated, the gage indicated a low relative humidity.

2.3 Design and Construction of Airfoil Models

Different airfoil models were designed and constructed to meet

the requirements for the calibration of the Transonic Wind Tunnel and the investigation of the drag reduction by the concept of the passive shock wave/boundary layer control.

2.3.1 Dobule Wedge Airfoil

A 3-inch chord, symmetrical double wedge airfoil of 10-percent thickness, Fig. 6, which spanned the test section of the 3-inch by 15.4-inch Transonic Wind Tunnel, was designed and constructed. This model was chosen for the wind tunnel test section calibration because experimental data for the same airfoil tested in similar conditions were available.[14] The airfoil model was mounted in the middle of the test section. The pressures over the model and the Schlieren photographs of the shock waves were taken for a range of free stream Mach numbers.

2.3.2 Biconvex Airfoil

A 3-inch chord biconvex airfoil of 12-percent thickness, Fig. 6, was designed next and constructed. The model was tested in the middle of the test section. The biconvex airfoil was chosen basically because it best represented the conventional wing airfoil and also because experimental data were available for comparison, in Refs. 15 and 16. The pressures over the model and the Schlieren photographs were obtained for transonic free stream Mach numbers.

2.3.3 3-Inch Circular Arc Airfoil

A 3-inch chord circular arc airfoil of 12-percent thickness, Fig. 6, was designed, constructed and mounted this time on the bottom surface of the test section to investigate the pressure and the shock

10-percent-thick double wedge airfoil
3-inch chord

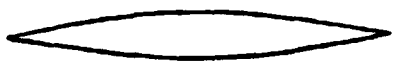

12-percent-thick biconvex airfoil
3-inch chord

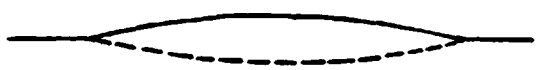

12-percent-thick convex airfoil
3-inch chord

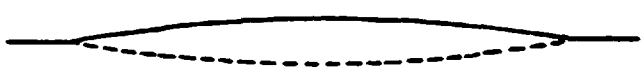

12-percent-thick circular arc airfoil
4-inch chord

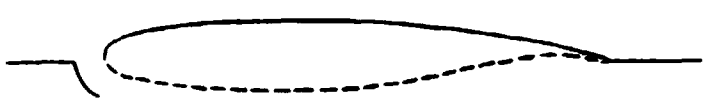

14-percent-thick supercritical airfoil
4-inch chord

Fig.6 Airfoils

wave and to simulate the shock wave/boundary layer interaction over the supercritical airfoil. Similar data, as for the previous models, were taken.

2.3.4 4-Inch Circular Arc Airfoil

A 4-inch chord circular arc airfoil of 12-percent thickness, Figs. 6 and 7a, was constructed and tested on the bottom surface of the test section. The model pressure distribution and the Schlieren photographs of the shock waves over the model were obtained. Based on this information, a porous surface with a cavity underneath it was positioned at the location of the shock wave/boundary layer interaction. Both the porous surface and the cavity were used to investigate the drag reduction by the concept of the passive shock wave/boundary layer control. The porous surface consisted of 12 rows of 38 holes each. The .021-inch diameter holes spanned the airfoil model and the porosity extended from 60 to 90 percent of the chord. The change of porosity was obtained by varying the porous surface length chordwise and by making the holes larger. Based on the model surface area, the porosity could vary from zero to 2.17 percent. Three different values of porosity were investigated: 2%, 1.3% and 1% porosity. The no-porosity case was obtained by plugging the holes.

Holes of 0.021 inch diameter were drilled perpendicular to the model surface, and pressure tubes were connected to these holes. Ten static pressures were distributed along the model centerline with an average spacing of 0.37 inch. The airfoil model was carefully sanded to provide an aerodynamically smooth surface. The initial extent of

Fig.7a 12-percent-thick circular arc airfoil

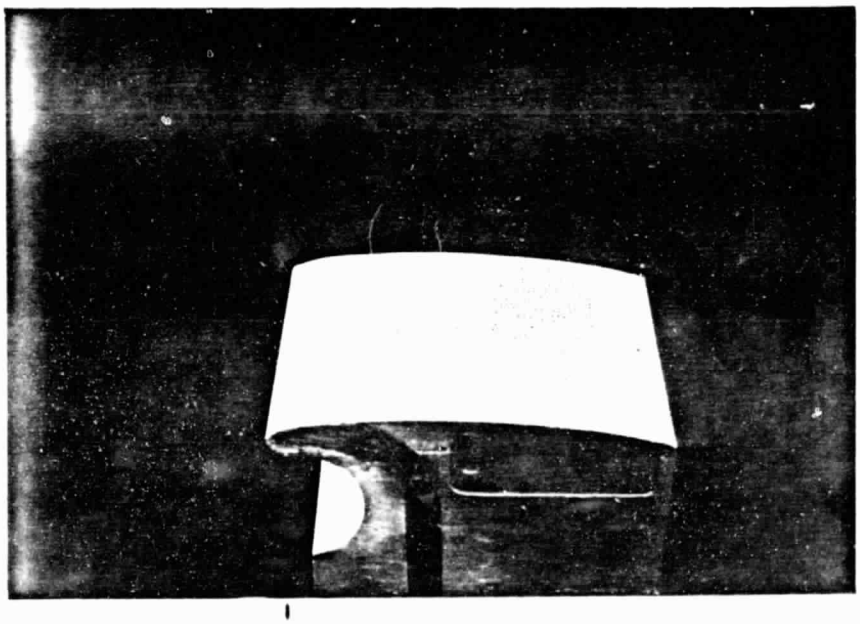

Fig.7b 14-percent-thick supercritical airfoil

the cavity under the porous surface was from 40 to 94 percent of the chord and spanned the airfoil model. Its dimensions were 2.125 inches long, 3 inches wide and 2 inches deep. The length of the cavity was later reduced to the porous surface size with a variable depth going from 2 inches to 0.25 inch, as shown in Fig. 8a. Investigations were conducted to study the cavity depth effect on the drag reduction and the flow field over the model.

2.3.5 Supercritical Airfoil

The basic concepts of supercritical airfoil technology were developed before adequate theoretical design or analysis codes were available. They were developed through an experimentally iterative process by evaluating the experimental pressure distributions at design and off-design conditions and physically altering the airfoil profile to yield the best drag characteristics over a range of Mach numbers. This is what happened at NASA Langley Research Center over the past several years, where "phas I airfoils" were developed and criteria were recognized which provided guidelines for the design of supercritical airfoils.[12] Based on these criteria, a 10-percent-thick[17] and a 14-percent-thick supercritical airfoil[12,18] were designed. The design lift coefficient was 0.7 for both airfoils. An iterative design process was used which consisted of altering the airfoil coordinates until the viscous airfoil analysis program, developed in Ref. 19, indicated that the design criteria for a shock-free flow over the upper surface had been satisfied.

For aircraft flying just below the speed of sound, a wing is at its "critical" Mach number when the air flowing over it accelerates

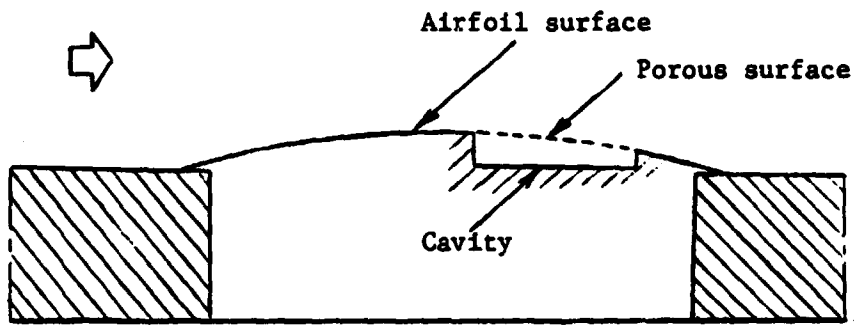

a. Circular arc airfoil

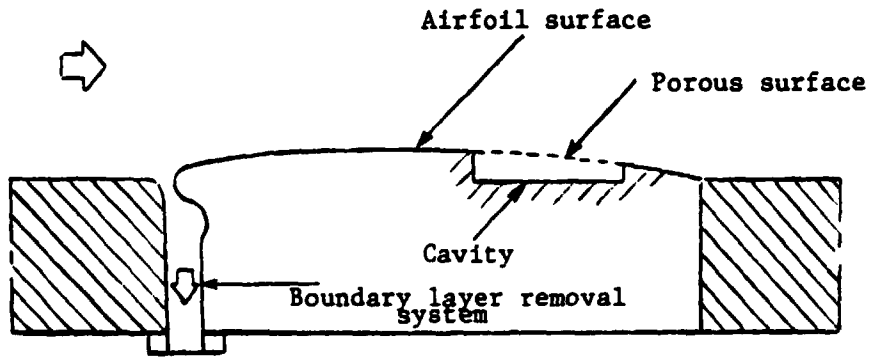

b. Supercritical airfoil

Fig.8 Circular arc and supercritical airfoils in test section

to the speed of sound because of the Bernoulli effect. The air then slows down, producing a shock wave that separates the boundary layer from the wing, increasing drag and decreasing lift. Supercritical wings allow an aircraft to fly faster before this occurs. The large radius at the front of the wing speeds up the air to supersonic velocity sooner, and the flatter top surface sustains the high speed longer over the wing with a more gradual speed reduction. The drag-producing shock wave is moved further back along the wing and is inherently weaker, as shown in Fig. 10.

A 14-percent-thick NASA supercritical airfoil,[18] Fig. 11, was used in the present work to investigate the drag reduction by the concept of the shock wave/boundary layer control. The construction of the model was based on 200 points derived from the coordinates for the upper surface presented in Table 1. A computer program was used to define the model profile. The program was then used on a computerized milling machine to obtain a 14-percent thick aluminum supercritical airfoil. The model had a chord of 4 inches and a span of 3 inches, Fig. 7b. The airfoil was carefully sanded to provide a smooth model surface. Orifices of 0.021-inch diameter were drilled perpendicular to the airfoil surface to measure the model pressure distribution. Seventeen static pressure taps were spaced along the centerline chord. The average spacing was 0.25 inch; however, in the leading edge region, the spacing decreased to 0.18 inch.

For the preliminary tests, the model was investigated with a smooth solid surface. Model pressure distribution, impact pressure wake survey and Schlieren photographs were obtained. Later, a porous surface

was introduced by drilling holes of 0.021-inch diameter on the model surface. It extended from 56 to 83 percent of the chord. The choice of the porous surface location was based on the Schlieren photographs and the pressure data obtained from the investigation of the model with a solid surface. The porous surface location was chosen such that the shock wave/boundary layer interaction region was in the middle of the porous surface. The porosity, based on the model surface, varied from 0 to 2.5 percent. The variation in the porosity was obtained by drilling larger holes or plugging some of them. The solid model surface was obtained by sealing all the holes. The porous surface spanned the airfoil model. Two different porosities of 0.94% and 2.5% were selected to investigate the drag reduction and the optimum porosity size. The cavity used for the boundary layer flow circulation through the porous surface had the same length and width as the porous surface and its depth could vary from 0 to 0.75 inch. Two cavity depths 0.75 and 0.25 inch were selected to study the cavity depth effect on the shock wave/boundary layer interaction and to investigate the optimum cavity depth.

For each porosity, the static pressure distributions, Schlieren photographs and impact pressure wake surveys were obtained over a range of flow Mach number of 0.65 to 0.82.

x/c	$(z/c)_u$	$(z/c)_l$
0.0000	0.0000	0.0000
.002	.0108	-.0108
.005	.0167	-.0165
.010	.0225	-.0223
.020	.0297	-.0295
.030	.0346	-.0343
.040	.0383	-.0381
.050	.0414	-.0411
.060	.0440	-.0438
.070	.0463	-.0461
.080	.0484	-.0481
.090	.0502	-.0500
.100	.0519	-.0517
.110	.0535	-.0533
.120	.0549	-.0547
.130	.0562	-.0561
.140	.0574	-.0574
.150	.0585	-.0585
.160	.0596	-.0596
.170	.0606	-.0606
.180	.0615	-.0616
.190	.0624	-.0625
.200	.0632	-.0633
.210	.0640	-.0641
.220	.0647	-.0648
.230	.0653	-.0655
.240	.0659	-.0661
.250	.0665	-.0667
.260	.0670	-.0672
.270	.0675	-.0677
.280	.0679	-.0681
.290	.0683	-.0685
.300	.0686	-.0688
.310	.0689	-.0691
.320	.0692	-.0693
.330	.0694	-.0695
.340	.0696	-.0696
.350	.0698	-.0697
.360	.0699	-.0697
.370	.0700	-.0697
.380	.0700	-.0696
.390	.0700	-.0695
.400	.0700	-.0693
.410	.0699	-.0691
.420	.0698	-.0689
.430	.0697	-.0686
.440	.0696	-.0682
.450	.0694	-.0678
.460	.0692	-.0673
.470	.0689	-.0667
.480	.0686	-.0661
.490	.0683	-.0654
0.500	0.0680	-0.0646
.510	.0676	-.0637
.520	.0672	-.0627
.530	.0668	-.0616
.540	.0663	-.0604
.550	.0658	-.0591
.560	.0652	-.0577
.570	.0646	-.0562
.580	.0640	-.0546
.590	.0634	-.0529
.600	.0627	-.0511
.610	.0620	-.0493
.620	.0613	-.0474
.630	.0605	-.0454
.640	.0596	-.0434
.650	.0587	-.0413
.660	.0578	-.0392
.670	.0568	-.0371
.680	.0558	-.0349
.690	.0547	-.0327
.700	.0536	-.0305
.710	.0524	-.0283
.720	.0512	-.0261
.730	.0499	-.0239
.740	.0486	-.0217
.750	.0472	-.0195
.760	.0457	-.0173
.770	.0442	-.0152
.780	.0426	-.0132
.790	.0409	-.0113
.800	.0392	-.0095
.810	.0374	-.0079
.820	.0356	-.0064
.830	.0337	-.0050
.840	.0317	-.0038
.850	.0297	-.0028
.860	.0276	-.0020
.870	.0255	-.0014
.880	.0233	-.0010
.890	.0210	-.0008
.900	.0186	-.0008
.910	.0162	-.0011
.920	.0137	-.0016
.930	.0111	-.0024
.940	.0084	-.0035
.950	.0057	-.0049
.960	.0029	-.0066
.970	.0000	-.0086
.980	-.0030	-.0109
.990	-.0062	-.0136
1.000	-.0095	-.0165

Table 1 : Section coordinates for 14-percent-thick supercritical airfoil

1. Supercritical airfoil
2. Porous surface
3. Cavity beneath porous surface
4. Free stream conditions
5. Embedded supersonic region
6. Sonic line
7. Terminating shock wave
8. Flow circulation through the porous surface
9. Wake survey rake

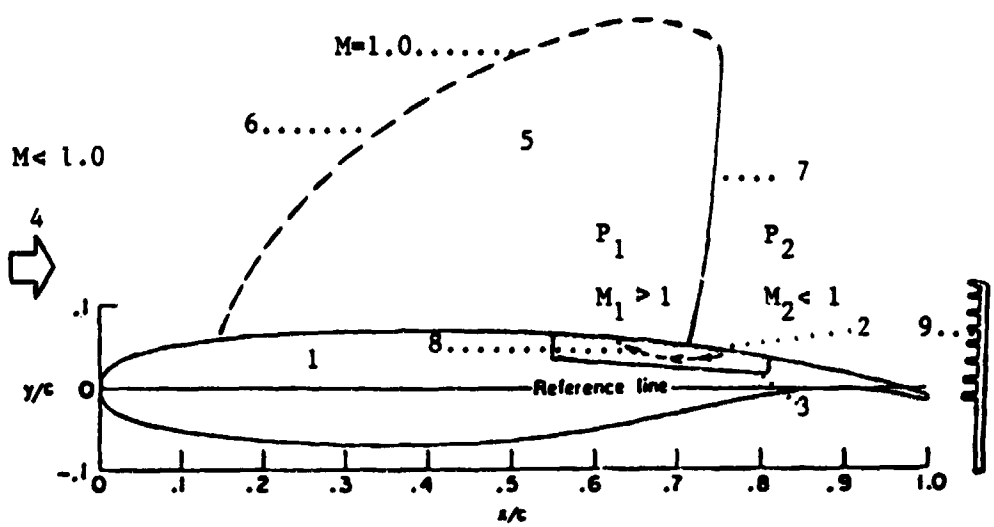

Fig.9 Passive drag control for supercritical airfoil at transonic Mach numbers

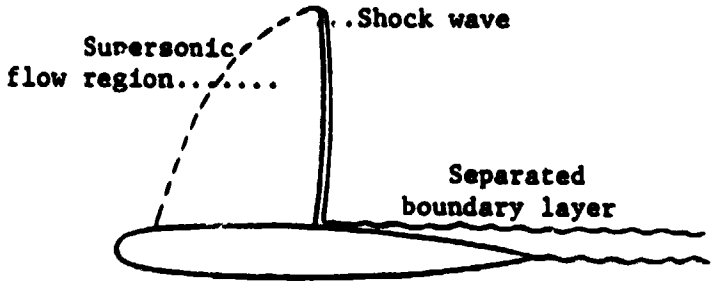

Conventional airfoil

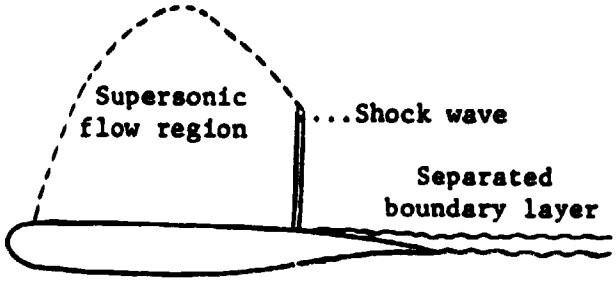

Supercritical airfoil

Fig.10 Conventional and supercritical airfoils

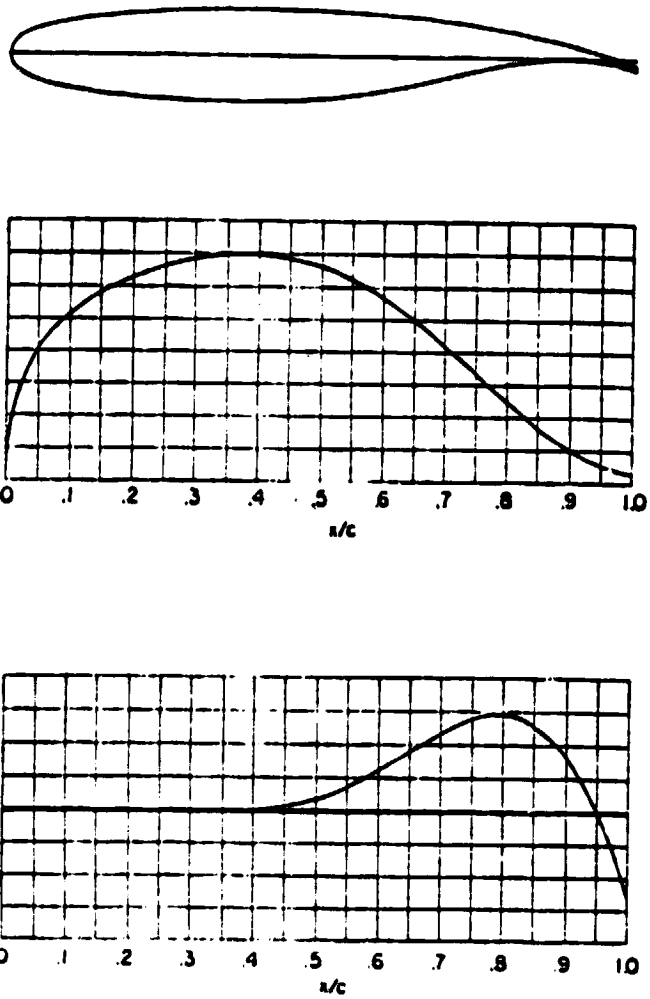

Fig.11 Profile, thickness distribution, and camber line of 14-percent-thick supercritical airfoil

PART 3

CALIBRATION OF THE EXPERIMENTAL FACILITY

For the initial calibration of the Transonic Wind Tunnel with the constant area test section, as shown in Figs. 1 and 3a, axial static pressure distributions and Schlieren and shadowgraph photographs were obtained. Different airfoil models were investigated in the original constant area mahogany test section, and from these preliminary test results it was decided to open the top, bottom, and side walls as shown in Fig. 3b. Experiments were conducted in the modified test section with the double wedge and biconvex airfoils mounted in the center of the test section, as well as with the 3-inch chord circular arc airfoil mounted on the bottom surface as shown in Fig. 6. The results for both the original and the modified test sections with and without the airfoils in the test section are discussed below.

3.1 Constant Area Test Section

3.1.1 Static Pressure Variation with Test Time

The variation of the geometrical area ratio A/A*, with the axial distance is presented in Fig. 12, where A* is the area of the original constant area test section and A is the area corresponding to the axial distance of the wind tunnel. A large area ratio for the settling section was selected to keep a low velocity through the entrance, honeycomb, and screens with corresponding low pressure loss. The large contraction ratio before the test section decreased the turbulence level in the accelerating flow region. To recover as much total pressure as

possible downstream of the test section, the area ratio at the end of the diffuser section was equal to 5, which is the maximum available with the existing 16-inch diameter discharge piping system.

To investigate the steadiness of the flow field and the performance of the different components of the tunnel as well as the test time, the static pressures at selected locations throughout the tunnel and the vacuum tank pressure were taken for various flow durations. The time variations of the static pressure at different axial locations are presented in Fig. 13. The static pressures in the settling chamber, x = 24 inches, and at the end of the test section, x = 109.25 inches, were nearly constant with time, indicating steady flow, but in the diffuser, x = 122 inches, downstream of the test section, the static pressure increased with time as the pressure in the large vacuum tank built up.

With the initial test section area, the steady flow duration in the test section was approximately 9 seconds. This was confirmed later with the aluminum test section by observing the steadiness of the shock wave through a frosted glass in the back of the camera box. A Kistler quartz pressure transducer[20] with a response time of 10 microseconds was installed in the test section to obtain the instantaneous variation of the static pressure with time. The pressure gage output was recorded on an oscilloscope and the result indicated that the flow in the test section was established in 0.4 second and remained constant approximately 9 seconds. This test time was long compared to the test time of 8 milliseconds for the Ludwieg tube used to obtain the pressure

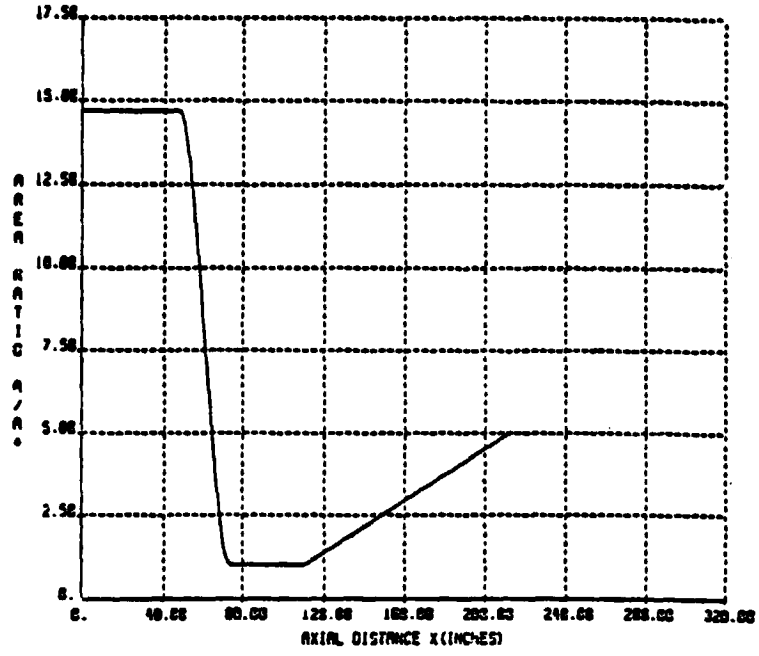

Fig.12 Transonic Wind Tunnel area ratio distribution

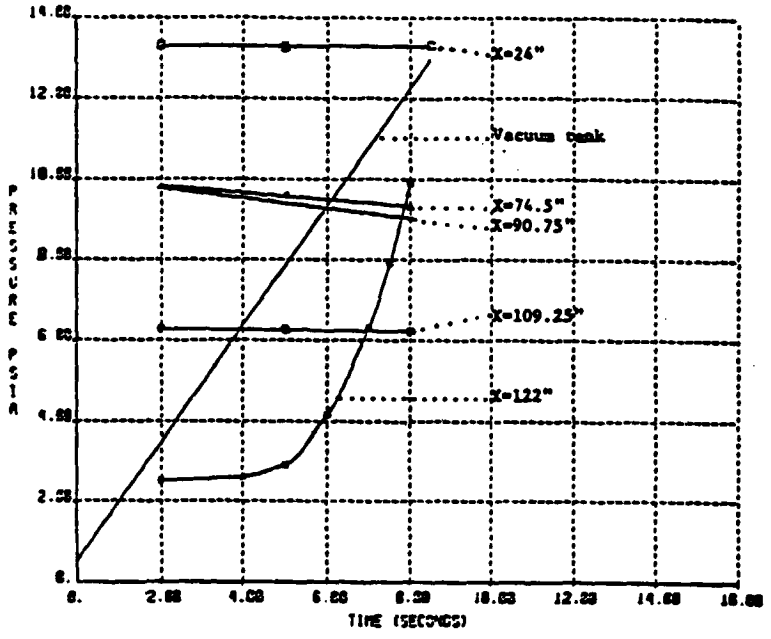

Fig.13 Static pressure variation with flow at various axial locations

distributions and the interferogram photographs at Mach numbers of 0.7 and 0.8 over a 10-percent biconvex airfoils with air, SF_6 and CO_2 gases in Ref. 21.

3.1.2 Axial Static Pressure and Mach Number Distributions

Based upon the nozzle cross sectional area distribution for the original test section presented in Fig. 12, the corresponding theoretical static pressure ratio and Mach number distributions are presented in Figs. 14 and 15, respectively. In the calculations of these flow parameters, the flow was assumed to be adiabatic, inviscid, one dimensional, and steady as discussed in Ref. 22. Subsonic and supersonic flow conditions were calculated downstream of the test section.

The nozzle static pressure ratio distributions for different flow duration time are compared with the theory in Fig. 14. For a flow duration of 2 seconds, the supersonic flow remained attached to the diffuser walls at least to a distance of 11 inches downstream of the test section. This was possible because the vacuum tank pressure for this flow duration was very low, as shown in Fig. 13. As the flow duration increased and brought about a corresponding increase in the vacuum tank pressure, the region of the supersonic flow downstream of the test section became shorter. At a flow duration of 8 seconds, the flow became subsonic slightly downstream of the test section, and the static pressure in the diffuser approached the theoretical subsonic flow values.

The static pressure distribution from the settling chamber to the test section exit remained nearly the same for flow duration of 4 to 8 seconds. The static pressures for the flow duration of 2 seconds were

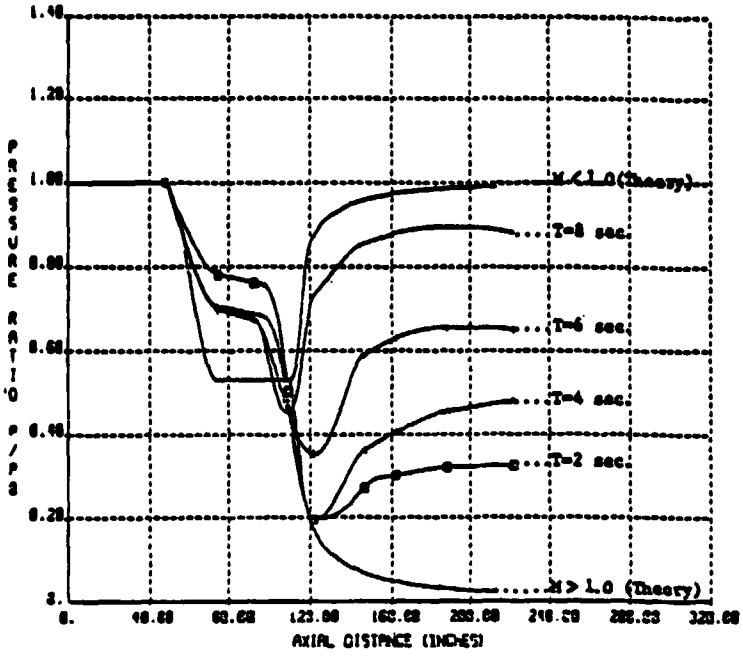

Fig.14 Static pressure distribution for various flow durations

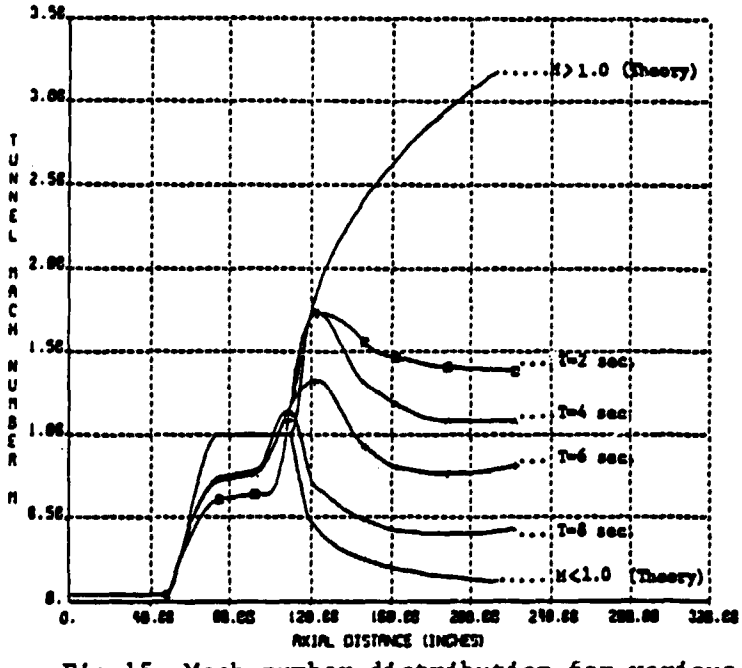

Fig.15 Mach number distribution for various flow durations

slightly higher than the values for longer test times. This difference was caused mainly by the long response time of the mercury manometers with long plastic tubings. A quartz piezoelectric pressure transducer was used for measuring the pressure in the test section to determine the flow establishment time as discussed previously.

The static pressure distributions in the test section were much higher than the theoretical inviscid values. Because of the boundary layer growth along the test section walls with the original constant area, Fig. 3a, the flow was choked near the exit of the test section where the effective flow area was a minimum. Ahead of the choked sonic Mach number location, the flow was subsonic and the static pressure ratio was greater than the sonic value of 0.528. The test section was modified to correct for this boundary layer choking phenomenon, Fig. 3b, and the results will be discussed later.

The axial Mach number distributions for different flow durations are compared with the inviscid theory in Fig. 15. For a test time of 2 seconds with low vacuum tank pressure, the flow accelerated to a Mach number of approximately 1.72 in the diffuser before the flow separated from the walls. Again as the flow duration increased, the maximum supersonic flow velocity and the region of the supersonic flow in the diffuser downstream of the test section decreased. The Mach number distirubtions from the settling chamber to the sonic location in the test section were nearly identical for flow durations of 4 to 8 seconds. This axial Mach number variation was due to the boundary layer growth along the tunnel walls as discussed previously.

3.2 Modified Test Section

The axial static pressure distributions, Fig. 14, for the original constant area test section, indicated the choking of the flow near the exit of the test section due to the boundary layer growth along the tunnel walls. To correct for the boundary layer growth, the following test section modifications, as discussed earlier, were investigated: opened top wall; opened top and bottom walls; opened top, bottom, and side walls, as shown in Figs. 3a and 3b. The Mach number distributions in the test section for these modifications are presented in Fig. 16. The modifications of the test section and the results are discussed below.

3.2.1 Constant Area Test Section

The axial distance at the entrance of the test section was 73.5 inches, while the exit was located at 110.0 inches. With the original 3-inch by 15.4-inch constant area test section, the Mach number increased from 0.72 at the entrance to 1.10 at the exit due to the boundary layer growth along the walls, as shown in Fig. 16. The flow was sonic a few inches before the test section exit and became supersonic at the exit due to the presence of the diverging diffuser walls, which tended to thin the boundary layer at the test section exit.

3.2.2 Test Section with Opened Top Wall

In order to accommodate for the boundary layer growth, the top wall of the test section was opened by tapering the mahogany wall from 15.4 inch opening at the entrance to 16.1 inches at the exit. This modi-

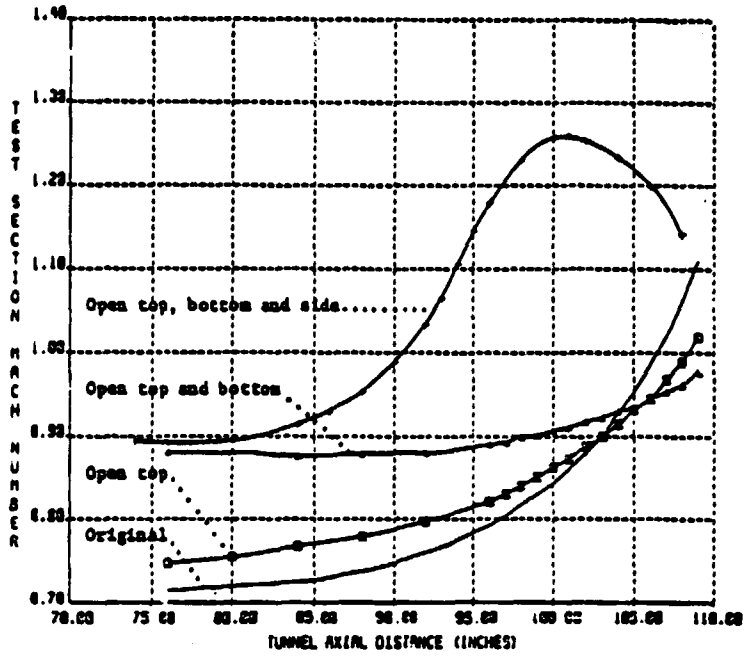

Fig.16 Test section Mach number distribution for different geometries

fication made the Mach number distribution in the test section flatter than that of the original configuration as shown in Fig. 16. The Mach number varied from 0.75 at the entrance to 1.02 at the exit. In addition, the sonic location was closer to the exit than in the original constant area test section.

3.2.3 Test Section with Opened Top and Bottom Walls

The bottom wall was tapered over the rear 16.5 inches from 15.4 inches to 16.1 inches as shown in Fig. 3b. The initial 20 inches of the bottom wall was horizontal to permit the investigation of the shock wave/boundary layer interaction over circular arc and supercritical airfoils with a porous surface. The Mach number distribution with the top and bottom walls opened was very flat over the first 20 inches of the test section as shown in Fig. 16. Along the test section, the Mach number increased from 0.88 to 0.98 at the exit. For this configuration, the flow was choked near the diffuser entrance.

3.2.4 Test Section with Opened Top, Bottom and Side Walls

For further increase of the free stream Mach number, the test section area was enlarged by tapering the side walls from a width of 3.0 inches at 20 inches downstream of the entrance to the test section to a width of 3.30 inches at the exit of the test section as shown in Fig. 3b. The Mach number increased from 0.89 at the entrance to 1.26 at 30 inches downstream and then decreased to 1.13 at the exit. The flow was sonic at approximately 17.5 inches from the entrance. By opening the 4 walls of the test section, the Mach number at the entrance was increased from

0.72 for the original constant area test section to 0.89. The use of mahogany for the top and bottom walls and thick lucite for the side walls had made the modification of the test section to correct for the boundary layer growth fairly easy. Based on the knowledge gained from the calibration of this initial mahogany test section, an aluminum porous top wall test section was designed and constructed. This test section helped in obtaining the flow data without side wall deflection effects, besides being more rigid and durable.

3.3 Boundary Layer Surveys for Test Section Walls

The uniformity of the flow field and the choking Mach number in the test section depended on the growth of the boundary layer along the walls. By correcting for the boundary layer growth, it was possible to control both of these flow phenomena. For this purpose, boundary layer surveys were made at selected locations on the bottom and side walls of the original constant area test section, Fig. 3a. Since the test section was symmetrical, the boundary layer growth was assumed to be the same on the top and bottom surfaces and also on both side walls. Boundary layer displacement thicknesses were calculated for both walls from the impact pressure surveys across the boundary layers.

3.3.1 Bottom Wall Boundary Layer Survey

Locations near the inlet, middle and exit of the test section at corresponding axial distances of x = 76.75, 94.87 and 106.75 inches were selected for the boundary layer survey for the bottom wall. Impact pressures across the boundary layer were measured with a small impact

pressure probe and the results are presented in Fig. 17a. Impact pressure surveys indicated that the boundary was fairly thin at the entrance to the constant area test section and became quite thick at the exit.

From the measured static and impact pressure data for the boundary layer at different axial locations in the test section, the corresponding velocity distributions in the boundary layer were calculated for an assumed adiabatic flow. The velocity in the boundary layer was normalized with respect to the free stream velocity. The vertical distance from the wall was normalized with respect to the boundary layer thickness. The normalized velocity distributions for the three axial locations are presented in Fig. 17b. At all three locations the velocity distribution indicated that a turbulent boundary layer existed over the surface.

3.3.2 Side Wall Boundary Layer Survey

The side wall boundary layer was surveyed on the centerline of the test section at three axial locations of 77, 92.62 and 106.50 inches, which corresponded to near the inlet, middle and near the exit of the test section, respectively. The results of these impact pressure surveys are presented in Fig. 18a. The side wall boundary layer increased with the axial distance, and at the test section exit, x = 106.5 inches, the boundary layer was fairly thick. To correct for this boundary growth, the side walls were widened as indicated in Fig. 3b.

The normalized velocity distributions calculated from the measured static and impact pressures for the three axial location in the test section are presented in Fig. 18b. The side wall boundary layer distributions for axial locations of 77 and 106.5 inches are compared

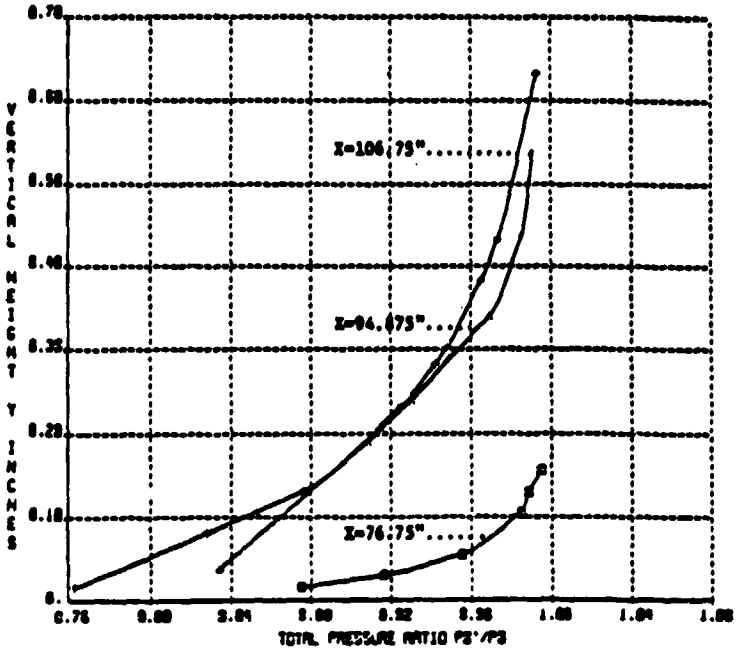

Fig.17a Bottom wall boundary layer surveys at three axial locations

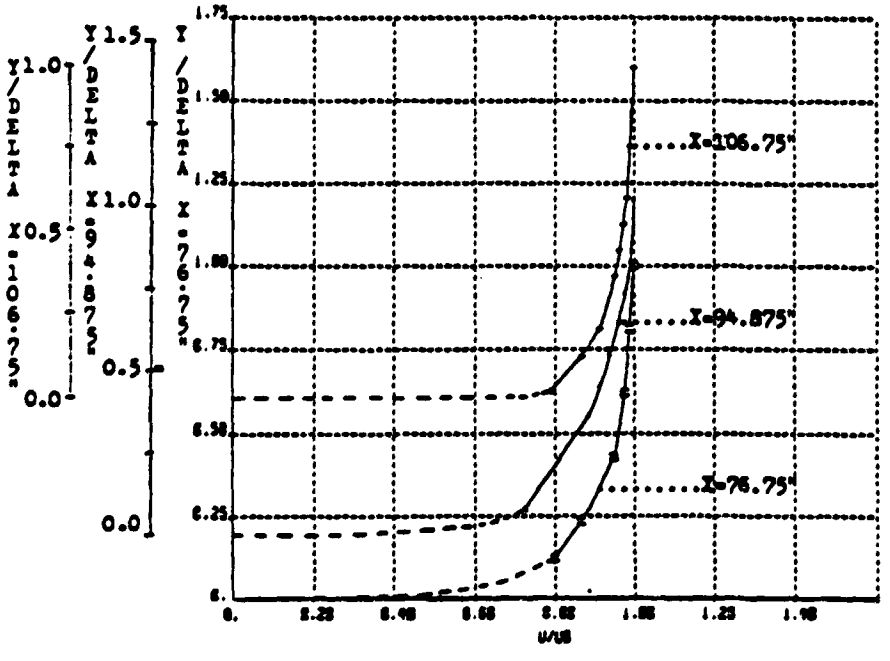

Fig.17b Bottom wall velocity distributions at three axial locations

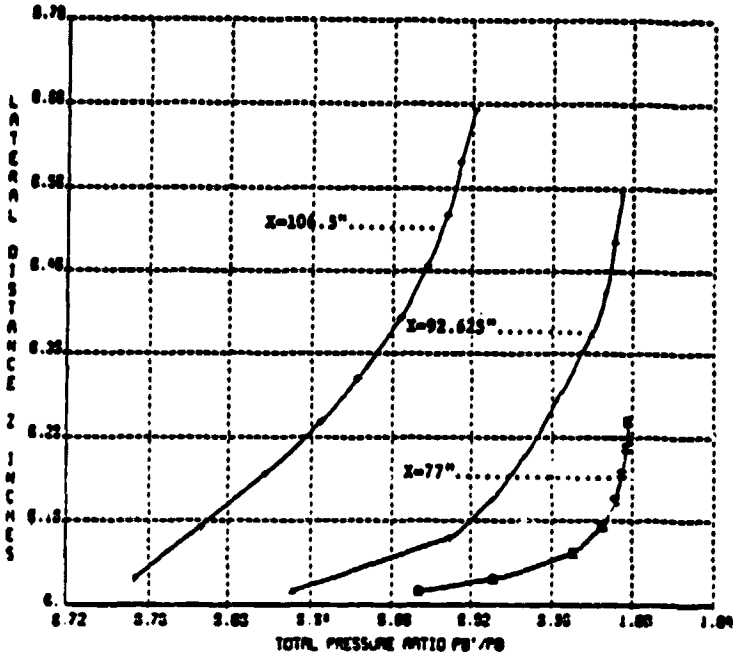

Fig.18a Side wall boundary layer surveys at three axial locations

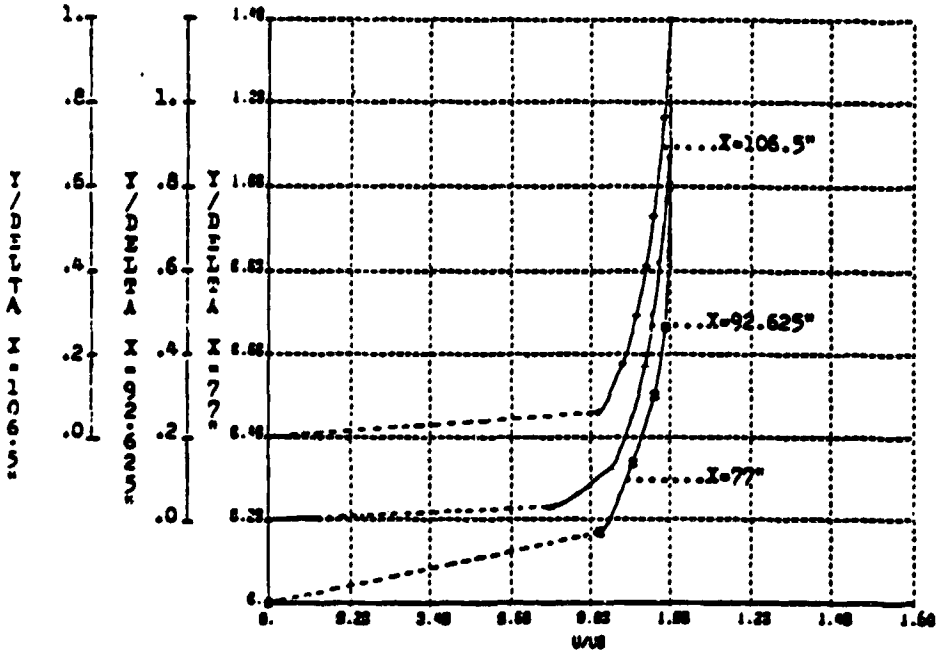

Fig.18b Side wall velocity distribution at three axial locations

with the laminar and turbulent boundary layer velocity distributions in Fig. 18c, and the results indicate the turbulent boundary layer characteristics.

3.3.3 Boundary Layer and Displacement Thickness on Test Section Walls

The boundary layer thickness for the test section bottom and side walls, determined from the impact pressure surveys at three axial locations, Figs. 17a and 18a, are presented in Fig. 19a. It is evident in this figure that the boundary layer thickness and the growth along the bottom and side walls were about the same. The apparent boundary layer thickness near the exit on the side wall was slightly less than on the bottom wall because the impact pressure survey was not extended further from the side wall, as shown in Fig. 18a. The boundary layers on the tunnel walls grew more rapidly over the front part of the constant area test section, Fig. 3a, than over the aft portion.

From the measured impact pressure across the boundary layer and the wall static pressure, the velocity and density were calculated by assuming an adiabatic flow. These values were used to calculate the boundary layer displacement, δ^*, from the equation

$$\delta^* = \int_0^\infty \left(1 - \frac{\rho u}{\rho_e u_e}\right) dy$$

where u is the velocity, ρ the density, and $\rho_e u_e$ is the mass flow rate outside the boundary layer. The calculated displacement thickness for the bottom and side walls are presented in Fig. 19b. For both walls, the displacement thickness grew rapidly over the initial portion of the constant area test section. The displacement thickness on the bottom

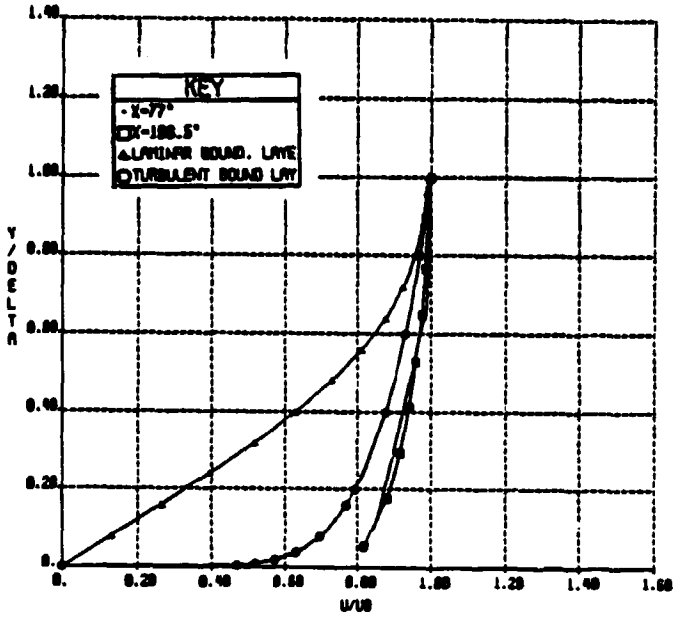

Fig.18c Comparison between side wall and laminar and turbulent velocity distributions

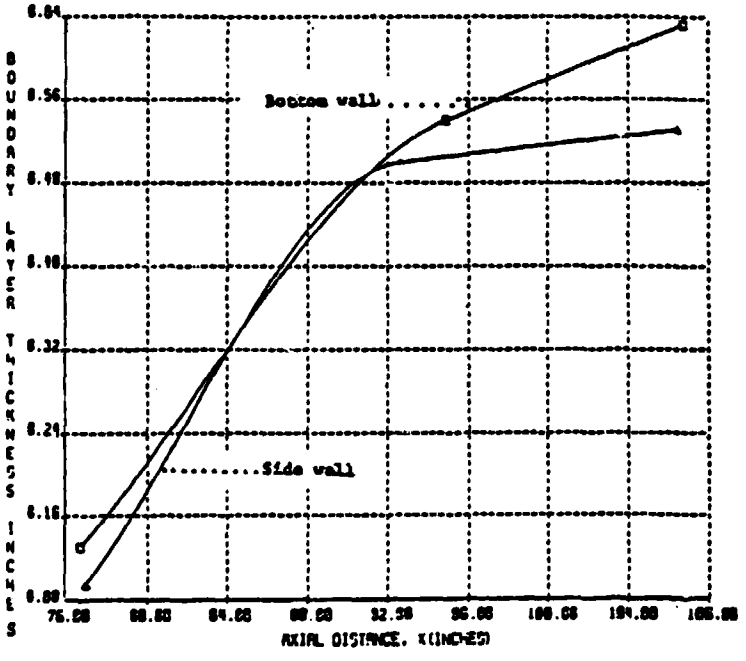

Fig.19a Boundary layer thickness distribution for bottom and side walls

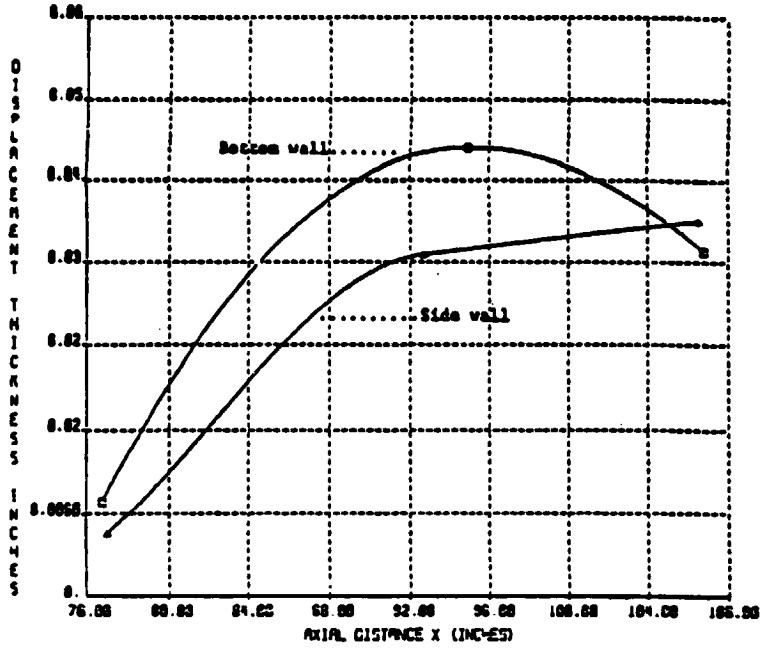

Fig.19b Boundary layer displacement thickness distribution for bottom and side walls

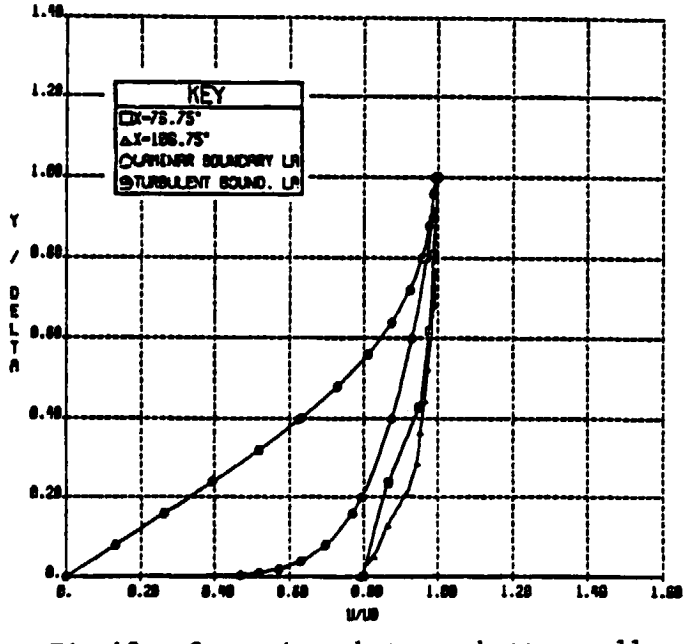

Fig.19c Comparison between bottom wall and, laminar and turbulent velocity distributions

wall near the exit of the test section was less than the value at the axial location of 94.87 inches. This decrease in the displacement thickness was caused by the acceleration of the flow toward the exit of the constant area test section as shown in Fig. 16.

3.4 Flow over Double Wedge, Biconvex and Circular Arc Airfoils

3.4.1 Flow over Double Wedge Airfoil

A 10-percent-thick double wedge airfoil with a chord of 3 inches was constructed out of aluminum to investigate the flow field and the shock wave structure at transonic Mach numbers. The airfoil was mounted in the center of the plexiglass side walls test section at an axial distance of 91.75 inches. Static pressure orifices are located on the top wedge surface at 40, 50 and 60 percent of the chord from the model leading edge.

For these tests, the top, bottom and side walls of the tunnel were opened as shown in Fig. 3b. From the measured static pressures and the reservoir total pressure; the local flow Mach number in the test section and over the model was determined. Ahead of the airfoil the flow Mach number was 0.88. Over the wedge the flow accelerated to a Mach number of approximately 1.26 at a location slightly downstream of the mid-chord as shown in Fig. 20a. Only a few static pressure orifices were installed in this airfoil to obtain the maximum flow velocity over the wedge surface with a simple model.

The Schlieren and shadowgraph photographs of the flow over the 10-percent thick double wedge airfoil were taken to observe the shock

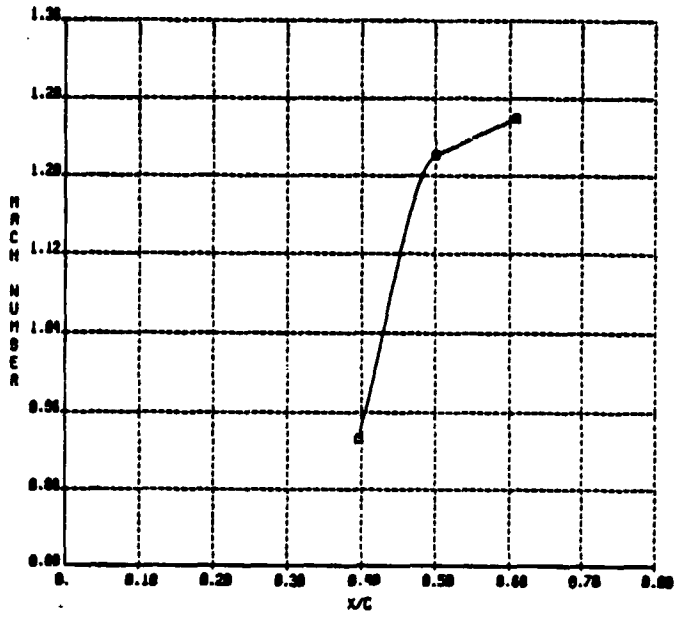

Fig.20a Mach number distribution over 10-percent-thick double wedge airfoil, M_∞=0.88

waves and boundary layer in the transonic flow region over the airfoil. The Schlieren photographs with vertical and horizontal knife edge positions are presented in Figs. 20b and c. In the vertical position, the knife edge was more parallel to the shock waves and made the shock wave and the expansion region more visible, as shown in Fig. 20b. The expansion fan from the maximum thickness region of the airfoil is visible as a dark or light region depending on how the vertical knife edge cut the light beam from left or right. In this region, the density decreased as the flow accelerated through the fan. An oblique shock wave terminated the expansion region and intersected the nearly normal terminating shock wave. In the photographs the stress concentration in the lucite side walls around the model support holes is visible as well as the plastic tubing outside the walls, used for measuring the static pressures on the model.

The Schlieren photograph, with the horizontal knife edge to make the boundary layer over the airfoil and the wake more visible, is presented in Fig. 20c. In this photograph, the boundary layer near the trailing edge and the wake flow are quite visible, but only the oblique shock wave is distinctly visible.

3.4.2 Flow over Biconvex Airfoil

An aluminum, 12-percent-thick, biconvex airfoil with a 3-inch chord was placed in the center of the test section, similar to the double wedge airfoil. Static pressure orifices on the top of the airfoil were located at x/c of 0.21, 0.39, 0.50, 0.62 and 0.79. The Mach number ahead of the model was 0.89. The flow accelerated over the biconvex airfoil to

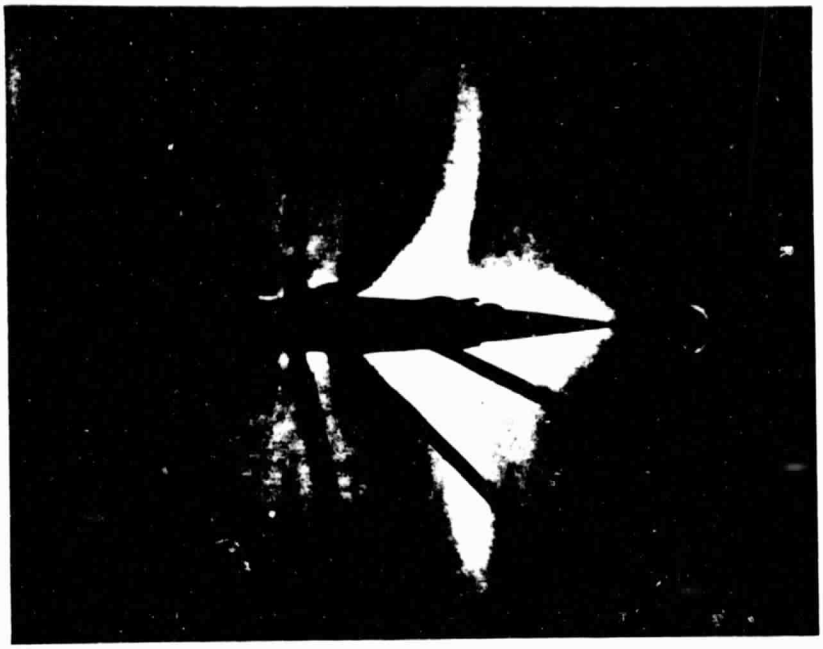

Fig.20b Schlieren photograph of flow over 10-percent-thick double wedge airfoil,vertical knife edge ,M_∞=0.83

Fig.20c Schlieren photograph of flow over 10-percent-thick double wedge airfoil,horizontal knife edge, M_∞=0.83

a maximum value of 1.25 downstream of the mid-chord as shown in Fig. 21a. The Schlieren photograph of the flow over the 12-percent-thick biconvex airfoil shows a nearly normal shock wave, which is more visible on the upper surface. The shock wave location on the upper surface was at 78 percent of the chord, while on the lower surface, it was slightly downstream of this location. The photograph shows also some distortion of the airfoil leading edge, because of the side walls deflection. This shortcoming was overcome later, in the aluminum test section by going to a thicker side wall plexiglass and adding aluminum plates on both sides with a circular cut at the model location to be able to take the flow field and the model photographs. From the shadowgraph photograph, Fig. 21b, the boundary layer and its separation over the 12-percent-thick biconvex airfoil are visible.

3.4.3 Flow over Circular Arc Airfoil

A 12-percent-thick convex airfoil made out of plexiglass was mounted on the test section bottom surface, where the concept of the shock wave/boundary layer interaction control over a 14-percent-thick supercritical airfoil was investigated. Six static pressure orifices were used to obtain the pressure distribution over the model surface, and the Mach number distribution is presented in Fig. 22a. The Schlieren photograph showing the shock wave behavior is presented in Fig. 22b. With the vertical knife edge, the termination shock wave is very distinct in the photograph, due to a maximum flow Mach number of 1.29 over the model. At this high transonic Mach number, the pressure and the density change across the shock wave was appreciable, as indicated in Ref. 22.

The relatively strong shock wave indicated the presence of a large supersonic flow region over the model.[23]

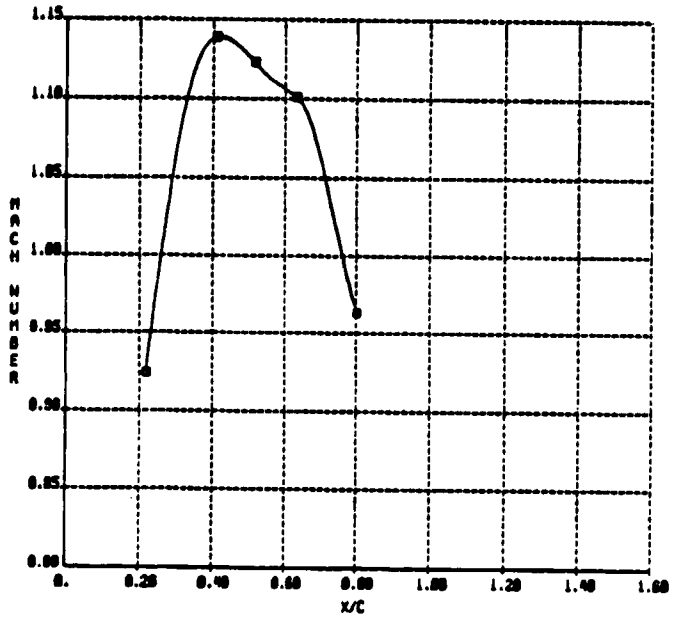

Fig.21a Mach number distribution over 12-percent-thick biconvex airfoil M_∞=0.88

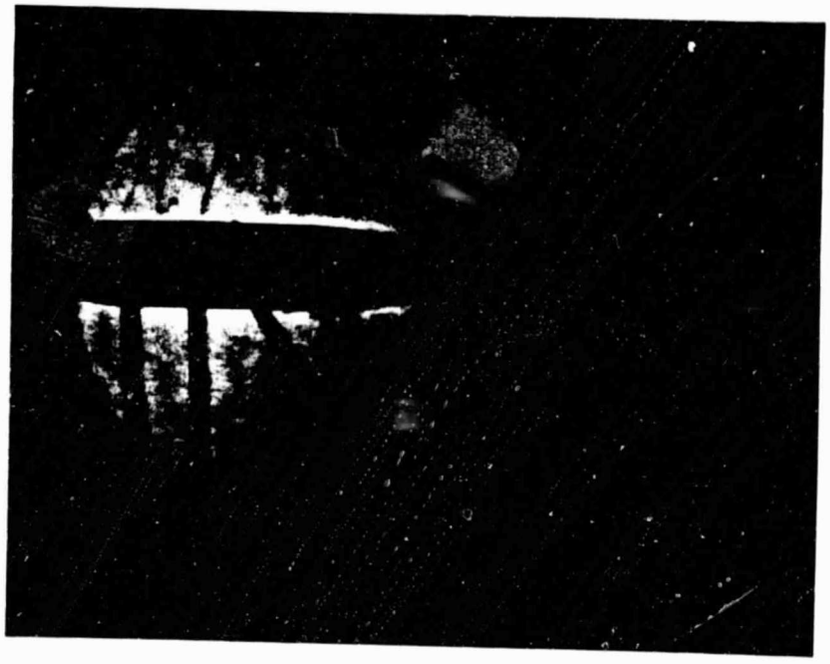

Fig.21b Shadowgraph photograph of flow over 12-percent -thick biconvex airfoil, M_∞=0.83

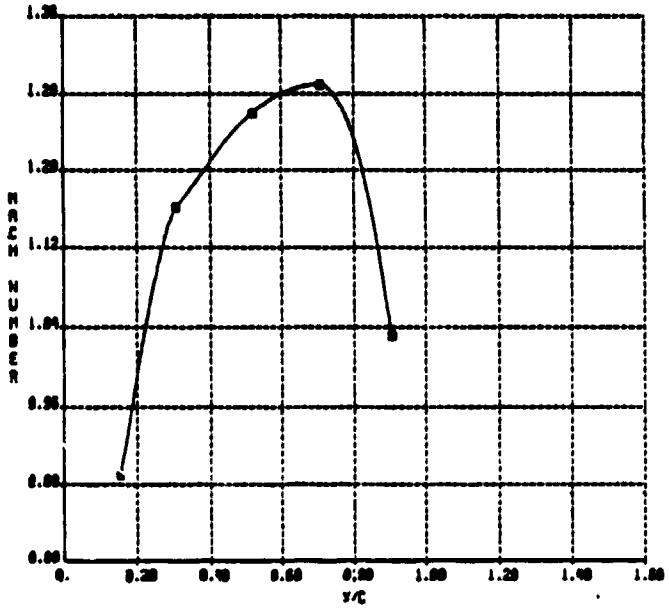

Fig.22a Mach number distribution over 12-percent-thick convex airfoil M_∞ =0.88

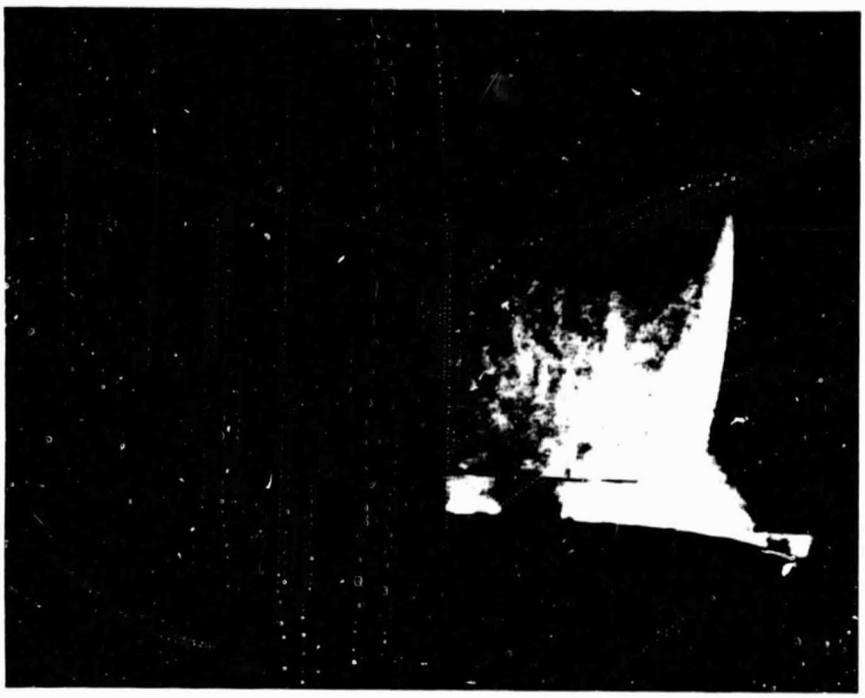

Fig.22b Schlieren photograph of flow over 12-percent-thick convex airfoil, $M_\infty = 0.83$

PART 4

THEORY

The basic equations of compressible flow used in the present research program for the data reduction are as presented in this section for the assumption of steady, perfect gas flow.

4.1 Isentropic Flow Equations

Determination of Mach number

The Mach number in the test section, over the model surface and throughout the tunnel, was obtained from measurements of the static pressure, P, and the total pressure in the settling chamber, P_o. The Mach number is then given by the well known compressible isentropic flow relations

$$\frac{P}{P_o} = \left[1 + \frac{(\gamma-1)}{2} M^2\right]^{-\frac{\gamma}{\gamma-1}}, \qquad (1)$$

where $\gamma = c_p/c_v$ was taken as 1.400.

Determination of Temperature

By reading the total temperature, T_o, in the settling chamber, which turns out to be very close to the room temperature, the temperature, T, at any location in the tunnel can be determined, once the corresponding Mach number is known, through the adiabatic relation:

$$\frac{T}{T_o} = \left(1 + \frac{\gamma-1}{2} M^2\right)^{-1} \qquad (2)$$

Determination of Density

Using the perfect gas relation to get the total density ρ_o,

$$\frac{P_o}{\rho_o} = RT_o, \tag{3}$$

The density at any tunnel location, for a corresponding Mach number, can be derived from the isentropic, perfect gas relation:

$$\frac{\rho}{\rho_o} = \left(1 + \frac{\gamma-1}{2} M^2\right)^{-\frac{1}{\gamma-1}} \tag{4}$$

where P_o and T_o are the total pressure and total temperature measured in the settling chamber.

Determination of Speed of Sound

Knowing the Mach number, the speed of sound can be derived from the adiabatic relation and is given by

$$\frac{a}{a_o} = \left(1 + \frac{\gamma-1}{2} M^2\right)^{-\frac{1}{2}}, \tag{5}$$

where a_o is the speed of sound of the gas at rest. By measuring T_o in the settling chamber, a_o is derived from the speed of sound relation

$$a_o = \sqrt{\gamma RT_o}, \tag{6}$$

and the local velocity sound, a, can also be determined by the same relation

$$a = \sqrt{\gamma RT} \tag{7}$$

once the corresponding T is derived from Eq. (2).

This speed of sound relation can be approximated by

$$a \approx 49\sqrt{T} \text{ ft/sec} \tag{8}$$

for air if T is in degrees Rankine.

Determination of the Flow Velocity

Knowing the Mach number and the speed of sound, the corresponding local velocity can be determined from the Mach number relationship

$$M = \frac{u}{a} \tag{9}$$

Determination of the Pressure Coefficient

The pressure coefficient in compressible flow depends on the Mach number as well as the static pressure and is defined as

$$C_p = \frac{P-P_\infty}{\frac{1}{2}\rho_\infty U_\infty^2} \tag{10}$$

For an isentropic flow, the equation may be rewritten in terms of the local Mach number as

$$C_p = \frac{2}{\gamma M_\infty^2}\left(\left[\frac{2 + (\gamma-1)M_\infty^2}{2 + (\gamma-1)M^2}\right]^{\frac{\gamma}{\gamma-1}} - 1 \right) \tag{11}$$

M_∞ is the free stream Mach number measured ahead of the model and M is the local Mach number obtained from the Eq. (1) by measuring the local static pressure and the total pressure in the settling chamber. The steps between Eqs. (10) and (11) can be found in Ref. 24.

The Area-Mach Number Relation

The area-Mach number relation for a steady, inviscid, compressible and one-dimensional flow is given by

$$\left(\frac{A}{A^*}\right)^2 = \frac{1}{M^2}\left[\frac{2}{\gamma+1}\left(1 + \frac{\gamma-1}{2} M^2\right)\right]^{\frac{\gamma+1}{\gamma-1}} \tag{12}$$

where A* is the throat area.

4.2 Normal and Oblique Shock Wave Relations

Normal Shock Wave Relations

The relation between the Mach numbers upstream and downstream of the normal shock wave is given by

$$M_2^2 = \frac{1 + \frac{\gamma-1}{2} M_1^2}{\gamma M_1^2 - \frac{\gamma-1}{2}}, \tag{13}$$

where M_2 is the Mach number downstream of the shock wave and M_1 is the Mach number upstream. Other useful relations can be derived from the continuity equation, as the ratio of densities

$$\frac{\rho_2}{\rho_1} = \frac{U_1}{U_2} = \frac{(\gamma+1)M_1^2}{(\gamma-1)M_1^2+2} \tag{14}$$

The ratio of the static pressures is often used to define the shock wave strength and is given by

$$\frac{P_2}{P_1} = 1 + \frac{2\gamma}{\gamma+1}(M_1^2 - 1) \tag{15}$$

From the energy equation the temperature jump across the shock wave is given by

$$\frac{T_2}{T_1} = 1 + \frac{2(\gamma+1)}{(\gamma+1)^2} \frac{\gamma M^2+1}{M_1^2}(M_1^2 - 1) \tag{16}$$

The corresponding jumps in density, pressure and temperature are from lower to higher values across the shock wave. The shock is said to compress the flow.

An important result is the increase in the entropy through the shock wave given by

$$\frac{S_2-S_1}{R} = \frac{\gamma+1}{12\gamma^2}\left(\frac{P_2-P_1}{P_1}\right)^3 \tag{17}$$

which means that the increase in entropy is third order in shock strength. The change in entropy can also be related to the total pressures upstream and downstream of the shock wave:

$$\frac{S_2-S_1}{R} = \ln \frac{P_{o1}}{P_{o2}} \tag{18}$$

where the ratio of total pressures is given by

$$\frac{P_{o2}}{P_{o1}} = \left[\frac{\gamma+1}{2\gamma M_1^2-(\gamma-1)}\right]^{\frac{1}{\gamma-1}}\left[\frac{(\gamma+1)M_1^2}{(\gamma-1)M_1^2+2}\right]^{\frac{\gamma}{\gamma-1}} \tag{19}$$

Oblique Shock Wave Relations

The same relations used for the normal shock wave can be applied here for the oblique shock wave with the modification of M_1 and M_2 being replaced by their normal components $M_1\sin\beta$ and $M_2\sin(\beta-\theta)$, respectively. β being the flow inclination to the shock wave and θ is the flow deflection after the oblique shock wave,

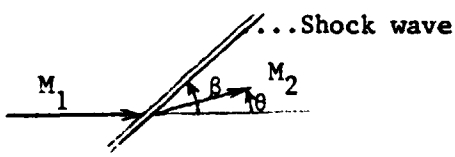

This gives the corresponding relations for the oblique shock:

$$M_2^2\sin^2(\beta-\theta) = \frac{1+\frac{\gamma-1}{2}M_1^2\sin^2\beta}{\gamma M_1^2\sin^2\beta-\frac{\gamma-1}{2}} \tag{20}$$

$$\frac{\rho_2}{\rho_1} = \frac{(\gamma+1)M_1^2\sin^2\beta}{(\gamma-1)M_1^2\sin^2\beta+2} \tag{21}$$

$$\frac{P_2}{P_1} = 1 + \frac{2\gamma}{\gamma+1}(M_1^2\sin^2\beta - 1) \tag{22}$$

$$\frac{T_2}{T_1} = 1 + \frac{2(\gamma-1)}{(\gamma+1)^2}\frac{M_1^2\sin^2\beta - 1}{M_1^2\sin^2\beta}(\gamma M_1^2\sin^2\beta + 1) \tag{23}$$

$$\frac{S_2 - S_1}{R} = \text{Ln}\frac{P_{o1}}{P_{o2}} \tag{24}$$

$$\frac{P_{o2}}{P_{o1}} = \left[\frac{\gamma+1}{2\gamma M_1^2\sin^2\beta - (\gamma-1)}\right]^{\frac{1}{\gamma-1}}\left[\frac{(\gamma+1)M_1^2\sin^2\beta}{(\gamma-1)M_1^2\sin^2\beta + 2}\right]^{\frac{\gamma}{\gamma-1}} \tag{24}$$

4.3 Profile Drag Derivation

The airfoil section profile drag measurements were computed from the wake survey rake measurements by the method of Ref. 25 utilizing the following equations:

$$C_d = \int_{\text{wake}} C_d' d\left(\frac{h}{c}\right) \tag{25}$$

$$C_d' = 2\left(\frac{H}{H_\infty}\right)^{\frac{\gamma-1}{\gamma}}\left(\frac{P}{P_\infty}\right)^{\frac{1}{\gamma}}\left(\frac{1-\left(\frac{P}{H}\right)^{\frac{\gamma-1}{\gamma}}}{1-\left(\frac{P_\infty}{H_\infty}\right)^{\frac{\gamma-1}{\gamma}}}\right)^{\frac{1}{2}}\left[1 - \left(\frac{1-\left(\frac{P_\infty}{H}\right)^{\frac{\gamma-1}{\gamma}}}{1-\left(\frac{P_\infty}{H_\infty}\right)^{\frac{\gamma-1}{\gamma}}}\right)^{\frac{1}{2}}\right] \tag{26}$$

with H_∞ = free stream total pressure
P_∞ = free stream static pressure
H = local total pressure in the wake
P = local static pressure in the wake
C_d' = point drag coefficient
C_d = section drag coefficient

To obtain the section drag coefficients, point drag coefficients were computed for each total pressure measurement in the wake by using Eq. (26).

These point drag coefficients were then summed up according to Eq. (25), by numerical integration across the wake, based on the trapezoidal method.

4.4 Boundary Layer Analysis

Laminar Boundary Layer Along a Flat Plate

Starting from the boundary layer equations for a steady state and incompressible flow and introducing new dimensionless variables we get the following Blasius equation:

$$f\, f'' + 2f''' = 0 \tag{27}$$

where f is a dimensionless stream function defined as:

$$f' \equiv \frac{df}{dn} = \frac{u}{u_\infty} \tag{28}$$

with

$$n = y\sqrt{\frac{u_\infty}{\nu x}} \tag{29}$$

a numerical solution of Eq. (27) by L. Howarth is presented in Ref. 26.

The boundary layer thickness deduced from the numerical solution is given by

$$\delta = 5.0\sqrt{\frac{\nu x}{u_\infty}} \tag{30}$$

and based on the Reynolds number, $R_{e_x} = \frac{\rho u_\infty x}{\mu} = \frac{u_\infty x}{\nu}$, and the boundary layer thickness can be written as

$$\delta = \frac{5.0x}{\sqrt{R_{e_x}}} \tag{31}$$

the dimensionless coordinate η can be written as

$$\eta = y\sqrt{\frac{u_\infty}{\nu x}} = \frac{y}{x}\sqrt{R_{e_x}}$$

which yields

$$\frac{y}{\delta} = \frac{\eta}{5.0} , \tag{32}$$

and the values of y/δ are presented in Ref. 26.

A physically meaningful measure for the boundary layer thickness is the displacement thickness, δ^*. The displacement thickness is that distance by which the external potential flow field is displaced outwards as a consequence of the decrease in velocity in the boundary layer. The decrease in volume flow due to the influence of friction is given by

$$\int_{y=o}^{\infty} (u_\infty - u)dy$$

so that for δ^* we have the definition

$$u_\infty \delta^* = \int_{y=o}^{\infty} (u_\infty - u)dy$$

or

$$\delta^* = \int_{y=o}^{\infty} (1 - \frac{u}{u_\infty})dy \tag{33}$$

From the solution presented in Ref. 26, the displacement thickness δ^* is given by

$$\delta^* = 1.73\sqrt{\frac{\nu x}{u_\infty}} \tag{34}$$

or

$$\delta^* = \frac{1.73x}{\sqrt{R_{e_x}}} \tag{35}$$

Turbulent Boundary Layer Along a Flat Plate

The velocity profile of a turbulent boundary layer for an incompressible flow can be represented by an empirical equation[26]

$$\frac{u}{u_\infty} = \left(\frac{y}{\delta}\right)^{\frac{1}{n}} , \tag{36}$$

and the assumption of a simple $\frac{1}{n}$th-power law agrees with experiment. Based on $\frac{1}{7}$th-power law which is valid for moderate Reynolds numbers, the velocity profile of a turbulent boundary layer over a flat plate at zero incidence is given by

$$\frac{u}{u_\infty} = \left(\frac{y}{\delta}\right)^{\frac{1}{n}} \tag{36a}$$

where $\delta = \delta(x)$ denotes the boundary layer thickness which is a function of distance, x. The velocity distribution is presented in Figs. 18c and 19c. The equation for the local shearing stress is given by

$$\frac{\tau_o}{\rho u_\infty^2} = 0.0225\left(\frac{u}{u_\infty \delta}\right)^{\frac{1}{4}} = \frac{d\theta}{dx} , \tag{37}$$

where θ is the momentum thickness.

Using equation (36a), and the definition of θ in Eq. (37), we obtain

$$\delta^* = \frac{\delta}{8}$$

$$\theta = \frac{7}{72}\delta \tag{38}$$

The differential equation for the boundary layer thickness is given by

$$\frac{7}{72}\frac{d\delta}{dx} = .0225\left(\frac{\nu}{u_\infty \delta}\right)^{\frac{1}{4}} \tag{39}$$

The integration of Eq. (39) yields

$$\delta(x) = .37x\left(\frac{u_\infty x}{\nu}\right)^{-\frac{1}{5}}$$

or

$$\delta = .37x/R_{e_x}^{-2} \tag{40}$$

with

$$R_{e_x} = \frac{\rho_\infty u_\infty x}{\mu_\infty} = \frac{u_\infty x}{\nu_\infty}$$

The displacement thickness, δ^*, from Eq. (38) is given by

$$\delta^* = \frac{.046x}{R_{e_x}^{.2}} \tag{41}$$

Compressibility Effect

The above equations have been derived for an incompressible flow case. For a laminar boundary layer, Fig. 15.6 in Ref. 26 shows that for a free stream Mach number ranging from 0 to 1.00, which corresponds to the present experimental work, the compressibility effects on the velocity distribution within the boundary layer over a flat plate of zero incidence are negligible. Therefore, a comparison of the experimental boundary layer data with the theory of incompressible flow is a good approximation for our objective.

PART 5

DISCUSSION OF THE CALIBRATION PHASE RESULTS

5.1 Transonic Wind Tunnel

A 3-inch x 15.4-inch transonic wind tunnel was constructed (as shown in Figs. 1 and 2) which utilized the existing dryer, vacuum tank and vacuum pumps for the 4-Inch by 4-Inch Mach 3 Supersonic Wind Tunnel. The calibration of the flow through the tunnel was determined from the static pressure distribution throughout the length of the tunnel, the impact pressure in the settling chamber, and the impact pressure surveys in the test section. Schlieren and shadowgraph photographs were taken for a 10-percent-thick double wedge and 12-percent-thick biconvex airfoil mounted in the center of the test section, as well as for a 12-percent-thick circular arc airfoil placed on the test section bottom surface. The flow measurements were taken for different flow durations to determine the time of the flow establishment and the duration of the transonic flow test time.

The honeycomb and screens, Fig. 1, being the best combination for reducing turbulence at the entrance to the settling chamber, as discussed in Ref. 27, caused the flow entering the tunnel to be steady, as indicated by the constant settling chamber impact pressure shown in Fig. 13. The multilayered aircraft plywood with external reinforcement used for the contraction section, see Figs. 1 and 2, performed well for all test section Mach numbers. A gradual contraction profile accelerates the flow which becomes uniform at the entrance to the test section. The thick lucite side walls for the test section made it possible to observe

the shock waves and boundary layer over the airfoil models mounted in the center and on the bottom wall of the test section.

The long gradual diffuser section downstream of the test section performed well as indicated by the good pressure recovery in the diffuser, shown in Fig. 14. This permitted a choked, sonic velocity at the end of the original constant area test section, Fig. 3a, with a small pressure drop across the transonic tunnel, and allowed for a longer test time with the available vacuum tank and pumps.

The pneumatic, 16-inch diameter, quick-acting valve located at the exit of the diffuser section, Figs. 1 and 2, opened and closed in approximately 1.5 seconds with a good vacuum seal. The piezoelectric pressure measurement in the test section indicated that the flow was established in 0.4 second.

5.2 Instrumentation

The technique for the pressure data acquisition with the manometer board, Fig. 2a, was improved by replacing the ball valves with an electrically timed and actuated solenoid valve system. Leakage tests of up to 8 hours in length were conducted with negligible pressure losses in the measuring system. The system test results indicated that the time response was sufficiently short and accurate to obtain reliable pressure data, as did the fact that all of the pressures were taken simultaneously, which was not the case with the ball valves.

From Figs. 20b and 22b, for flows over a 10-percent-thick double wedge, and 12-percent-thick convex airfoils, respectively, it was apparent

that the Schlieren system was capable of obtaining photographs of the shock waves and boundary layers over these models. To observe the shock waves and boundary layer, the knife edge was positioned in the vertical and horizontal positions, respectively.

As can be seen from the shadowgraph photograph shown in Fig. 21b, the shadowgraph system appeared to be functioning satisfactorily. Further improvements of the optical system were made by the use of thicker lucite side walls, reinforced by aluminum plates, to eliminate the wall deflection on the new aluminum test section.[13]

5.3 Tunnel Wall Boundary Layer

As expected, the thickness of the boundary layer over the bottom and side walls for the constant area test section Fig. 3a, was increasing as it progressed from the entrance of the test section to the exit, as seen in Fig. 19a. For all axial locations, the velocity profiles for both walls agreed closely with the fully developed, turbulent boundary layer profile, as shown in Figs. 18c and 19c. On the bottom wall the boundary layer thickness increased from 0.094 inch to 0.53 inch near the exit. This relatively thick boundary layer over the test section walls was the reason for modifying the original constant area test section, as shown in Figs. 3a and 3b. Data from the impact pressure surveys across the boundary layer, were used to calculate the boundary layer displacement thickness for the side and bottom walls. The results are presented in Fig. 19b. The displacement thickness increased steeply over the initial region of the test section, but its growth from the center to the exit was more gradual. The displacement thickness was slightly

greater on the bottom wall, but near the test section exit, the thicknesses were about the same.

5.4 Flow Conditions in the Original and Modified Test Sections

With the original constant area test section shown in Figs. 1 and 3a, the Mach number at the entrance was 0.714 and increased monotonically over the 36.5 inch length to a Mach number of 1.11, as shown in Fig. 16. This increase in the Mach number in the test section was caused primarily by the growth of the boundary layer along the tunnel walls. The sonic velocity occurred close to the exit of the test section. To correct for the boundary layer displacement thickness, the top wall of the test section was opened 0.7 inch at the exit, Fig. 3b. The entrance Mach number increased to 0.75 and the exit Mach number decreased to 1.08, as shown in Fig. 16. By opening the top and bottom walls, Fig. 3b, the Mach number attained a more uniform value of 0.88 throughout most of the test section, except at the exit where the Mach number increased to 0.98, as shown in Fig. 16.

A third test section modification was made to increase the Mach number at the entrance to the test area. This was accomplished by keeping the side walls parallel over the initial 20 inches and then tapering them to 0.15 inch at the exit, Fig. 3b. The Mach number at the entrance increased to 0.89 and reached sonic velocity slightly ahead of the beginning of the diverging side walls, Fig. 16. The flow accelerated to a peak Mach number of 1.26 in the diverging side wall section, and subsequently decreased to a Mach number of 1.14 at the exit. The addition of the side wall modification appeared to have made the geometric area increase faster

than the boundary layer growth along the test section walls. Thus, the flow accelerated to a peak Mach number of 1.26 before the increase in boundary layer growth became greater than the increase in the geometric area.

Following the results of these calibration tests, an aluminum test section with an adjustable top porous wall was designed and constructed.[13] This new test section used many of the features from its mahogany predecessor, but at the same time, modifications were made to overcome some previously observed deficiencies. The lucite side walls were made thicker and aluminum plates were added to the sides to minimize the wall deflection. The variable porous top wall helped to reduce to a minimum the wall interference and the model blockage effect at high subsonic Mach numbers.[28] Other methods of minimizing the wall interference effects use slotted and adaptive walls as discussed in Refs. 29, 30 and 31.

5.5 Flow over Double Wedge and Biconvex Airfoils

The 10-percent-thick double wedge airfoil with a 3-inch chord was mounted in the center of the test section. With a Mach number of 0.88 ahead of the model, the maximum local Mach number over the airfoil reached 1.26. The Schlieren photograph, Fig. 20b, indicates the flow expansion region and the oblique and termination shock waves. The nearly normal termination shock wave was located at 68 percent of the chord. The Schlieren photograph and the pressure data are similar to the results obtained in Ref. 14 for a 10-percent-thick double wedge 3-inch chord airfoil in a 3-inch by 16-inch transonic wind tunnel with solid walls.

For the 12-percent-thick biconvex airfoil with a 3-inch chord and a free stream Mach number of 0.89, the flow accelerated to a peak Mach number of 1.25 downstream of the mid-chord, before decelerating towards the trailing edge. The Schlieren photograph shows a nearly normal shock wave at 78 percent of the chord on the upper surface of the model, while on the lower surface it is slightly downstream. This difference in locations comes from the fact that the angle of attack was not quite zero. On the shadowgraph photograph, Fig. 21b, the boundary layer and its separation are visible. In Ref. 15, the Mach number distributions over a 10-percent-thick biconvex airfoil were obtained over a Mach number range of 0.80 to 0.90 in a solid test section. In this reference the actual Mach number distribution at M_∞ of 0.89 is seen to have a higher local maximum Mach number. This is because of the difference in the thickness between the two models. In Ref. 16, strong shock waves are observed over a 12-percent-thick biconvex 3-inch chord airfoil, for a free stream Mach number of 0.89. The location of these shock waves is the same as the one obtained over the present similar biconvex airfoil. The tests in Ref. 16 were conducted in a 2-inch by 20-inch, solid wall, transonic wind tunnel.

5.6 Flow over Circular Arc Airfoil

The 12-percent-thick circular arc airfoil with a 3-inch chord was placed on the bottom wall of the test section. For a free stream Mach number of 0.88, the maximum local Mach number obtained over the model was 1.29. The model had a similar Mach number distribution as the 10-percent-thick model in Ref. 15, with a slightly higher maximum local

Mach number, because of the difference in the model thickness. The large extension of the strong shock wave into the flow indicates the presence of a large supersonic zone over the airfoil surface, as shown in the Schlieren photograph of Fig. 22b.

5.7 Passive Shock Wave-Boundary Layer Control for Supercritical Airfoils

To investigate the concept of the passive shock wave-boundary layer control for possibly reducing the drag of supercritical airfoils, various surface porosities were tested with different cavity geometries. The preliminary tests of the effects of porosity and cavity size on the shock wave/boundary layer interaction were conducted on a 12-percent-thick circular arc airfoil with a 4-inch chord to determine the effective porous surface configuration. Based on these test results, a 14-percent-thick NASA supercritical airfoil[18] was investigated with selected surface porosities and cavity sizes.

C-2

PART 6

EXPERIMENTAL RESULTS AND DISCUSSION

The following experiments have been conducted in the aluminum porous top wall test section described previously. A 12-percent-thick circular arc profile and a 14-percent-thick supercritical airfoil, both with a 4-inch chord, were investigated on the bottom surface of the test section. Each model was mounted in the middle of the first 20-inch flat surface. Two adjustable wedges installed downstream of the model at the test section exit, Fig. 4, were used to control the free stream Mach number from low subsonic to transonic speeds. The major part of the experiment was conducted with no test section top wall porosity, and a few tests were made to study the wall interference on the flow field.

The experiments which will be described below are aimed at reducing the drag by controlling the shock wave/boundary layer interaction over conventional and supercritical airfoils. The circular arc and supercritical airfoils were selected to achieve the desired objective. Both airfoils were investigated over a range of subsonic and transonic Mach numbers with various model porosities and different cavity sizes located in the region of the shock wave/boundary layer interaction.

The way to achieve passive drag control, as discussed previously, is to install a porous surface with a cavity underneath at the location of the shock wave over the model. By this procedure, because of the pressure difference across the shock wave, a part of the boundary layer flow will be moved from the region downstream to the region upstream of the shock wave through the porous surface and the cavity, as shown in Fig. 9.

This method will thin the boundary layer, downstream of the shock wave, by removing the decelerated flow, thus minimizing the separation. It also produces compression waves ahead of the shock which decreases its strength. The combination of these phenomena helps in reducing the drag of the airfoils in transonic flows, which is the major goal of the current aerodynamic research. Therefore, the research described in this Section is aimed at increasing the technology base for the development of practical means of improving aerodynamic performance and efficiency at high subsonic speeds.

Before initiating the airfoils investigation, the aluminum test section was calibrated with and without the side wall aluminum plates added to the lucite side walls. For the same control wedge setting, the test section with the aluminum plates gives a higher free stream Mach number than without because the deflection of the lucite side walls in the absence of the aluminum plates makes the effective minimum area smaller near the middle of the test section. By assuming the free stream area ahead of the model to be nearly constant and less affected by the deflection of the side walls, the ratio of the free stream area over the minimum area is smaller with the aluminum plates. This leads to a higher free stream Mach number for a subsonic speed range, as shown by the area-Mach number relation, Eq. 12, presented in Fig. 23 and confirmed by the experiments, Figure 24 · Consequently, the Mach number distribution is higher. The test results also show a more uniform free stream Mach number distribution, Fig. 24. To ascertain the extent to which the flow was uniform in the aluminum test section, vertical surveys

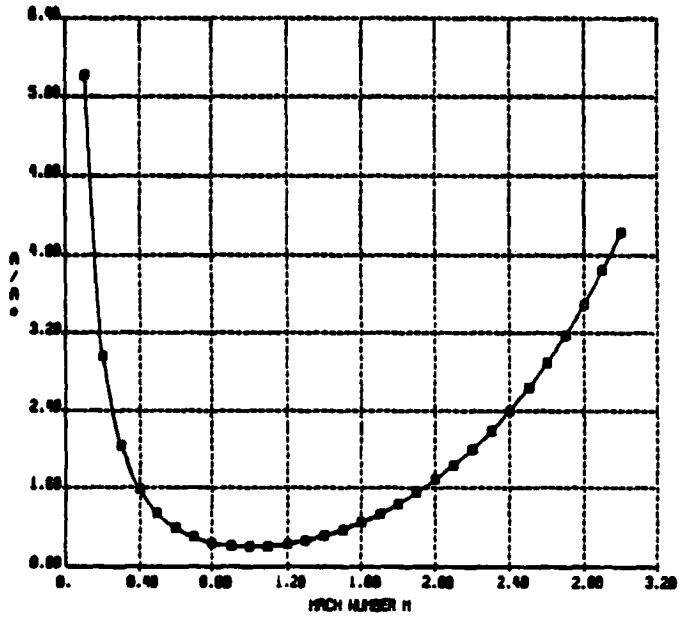

Fig.23 Area - Mach number relation

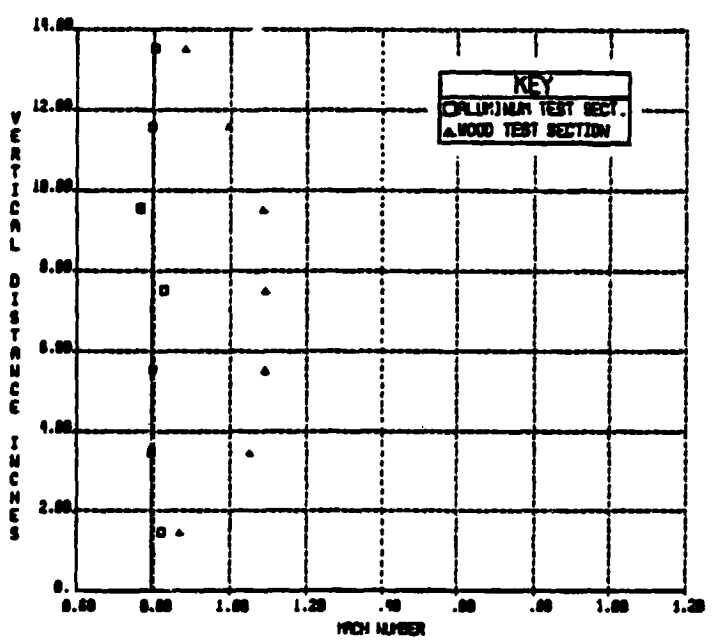

Fig.24 Vertical Mach number distributions in aluminum and wood test sections

taken along the side walls at axial locations of 77.5 and 83.31 inches, were compared with the vertical flow distribution at the same locations in the Mahogony test section. The uniformity of the Mach number distribution is far better with the aluminum test section. Therefore, the investigations over the circular arc profile and the supercritical airfoil were conducted in the aluminum test section with the aluminum plates. The experimental results which were obtained are discussed below.

6.1 Flow over Circular Arc Airfoil

6.1.1 Model Solid Surface Test Results

Before starting the investigation of the model porous surface effect on the flow field, pressure data were obtained with the no model porosity case and compared to Liepmann's results, Ref. 16. Figure 25 shows the comparison between the two experimental results. The overall pressure coefficient distributions are similar with some differences due to the different airfoil chords used in the present study and in Liepman's work. Liepmann used a 3-inch chord airfoil, whereas our model has a 4-inch chord, both with 12-percent thickness.

6.1.2 Preliminary Model Porous Surface

A 12-percent-thick circular arc airfoil with a 4-inch chord was placed in the center of the horizontal bottom wall of the 3-inch by 15.4-inch wooden transonic test section for preliminary investigation. The model surface was made porous, Fig. 7b, with a cavity beneath, in the region extending from 60 to 90 percent of the chord length from the model leading edge. The results of the initial tests with the porous surface,

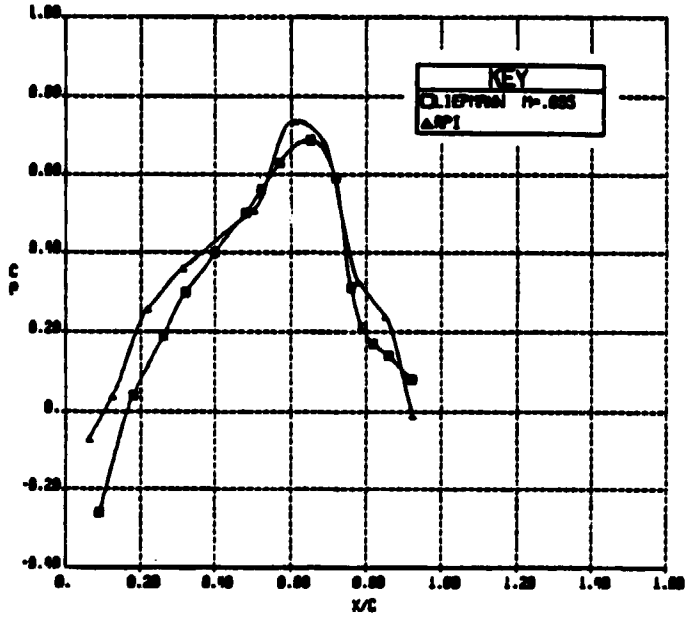

Fig.25 Pressure coefficient distributions over R.P.I and Liepmann 12-percent-thick circular arc airfoils

are presented in Figs. 26a and b, and indicate a change in the shock wave structure from a nearly normal shock wave to a Lambda shock wave, which is a combination of a normal and oblique shock waves. The oblique shock wave, caused by the flow circulation from the downstream to the upstream of the shock wave through the cavity below, starts at the porous surface leading edge and extends upward to meet the normal shock wave at a point in the free stream above the porous surface. The change of the terminating shock wave into a normal one and the appearance of the new oblique shock wave at the porous surface leading edge show the effect of the porous surface and cavity on the flow field at transonic speeds. This effect, partially represented by the area between the oblique and normal shock waves, increases with the free stream Mach number as shown in Figs. 26a and b. These preliminary results were a positive sign and indicated a need for further investigation of the concept of passive shock wave/boundary layer interaction control. Because of its advantages discussed above, the aluminum test section was designed, constructed and used for the rest of the experiments.

6.1.3 Effect of Aluminum Test Section Top Wall Porosity

To study the effects of top wall porosity, Schlieren photographs of the flow field over the 12-percent-thick circular arc profile, mounted in the center of the first 20-inch of the bottom wall, were taken for different wall porosities without the aluminum plates on the side walls of the test section. Figure 27a shows a strong, nearly normal shock wave terminating a large embedded supersonic region for the case of no top wall porosity. For the same control wedge setting at the test section exit,

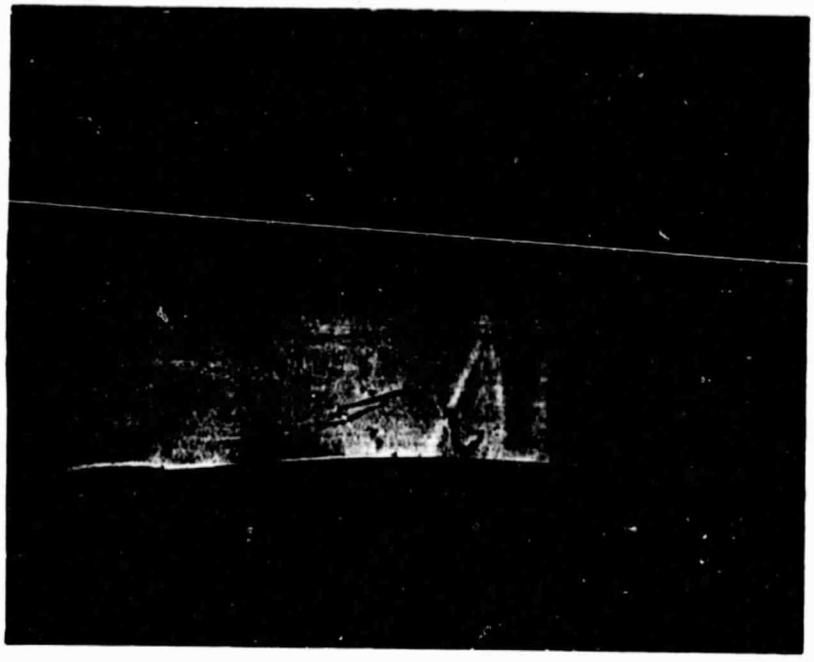

Fig.26a Schlieren photograph of flow over 12-percent-thick circular arc airfoil,with porosity, M_∞=0.84

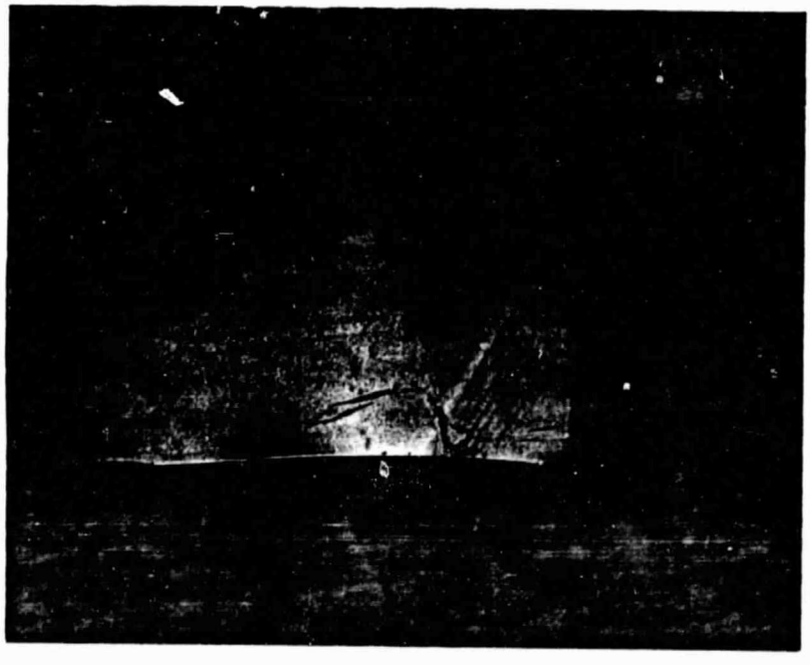

Fig.26b Schlieren photograph of flow over 12-percent-thick circular arc airfoil,with porosity, M_∞=0.87

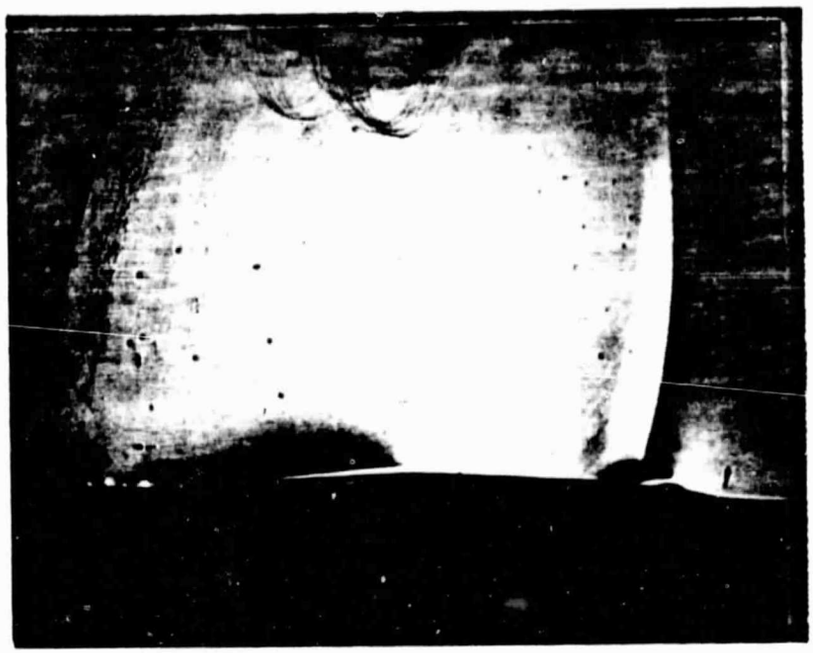

Fig.27a Schlieren photograph of flow over 12-percent-thick circular arc airfoil,without top wall porosity

Fig.27b Schlieren photograph of flow over 12-percent-thick circular arc airfoil,with 5 % top wall porosity

an increase in porosity decreases the size of the embedded supersonic zone and weakens the terminating shock wave and moves it upstream as indicated in Fig. 27b. As the porosity is increased to full top wall porosity of approximately 10-percent, the shock wave vanishes as shown in Fig. 27c. These preliminary tests in the aluminum test section were conducted with no model porosity. To minimize the effects of side wall deflection on the flow field, the aluminum plates were added and the investigation of the passive drag control of the circular arc airfoil was continued.

6.1.4 Effect of Model Porosity With Large Cavity

1.17 Percent Porosity

The model surface was made porous by drilling .021-inch diameter holes perpendicular to the surface. The full porous surface starts at 60 percent of the chord from the model's leading edge and extends downstream to 90 percent. The different porosities were developed through the chordwise variation of the porous surface length, by sealing or opening the appropriate holes, or by enlarging the hole size. This method enabled the investigation of the flow field with various porosities. The tests in this phase were conducted using a large cavity below the porous surface. The cavity was 2.125 inches long, 2.5 inches wide and 2 inches deep. The 1.17 percent porous surface is located between 70 and 90 percent of the chord. Schlieren photographs and pressure distributions along the model centerline were obtained with and without the model porosity.

The Schlieren photographs taken for the 1.17 percent porosity and the large cavity, Fig. 28b, show once again the effect of the model

Fig.27c Schlieren photograph of flow over 12-percent-thick circular arc airfoil, with 10 % top wall porosity

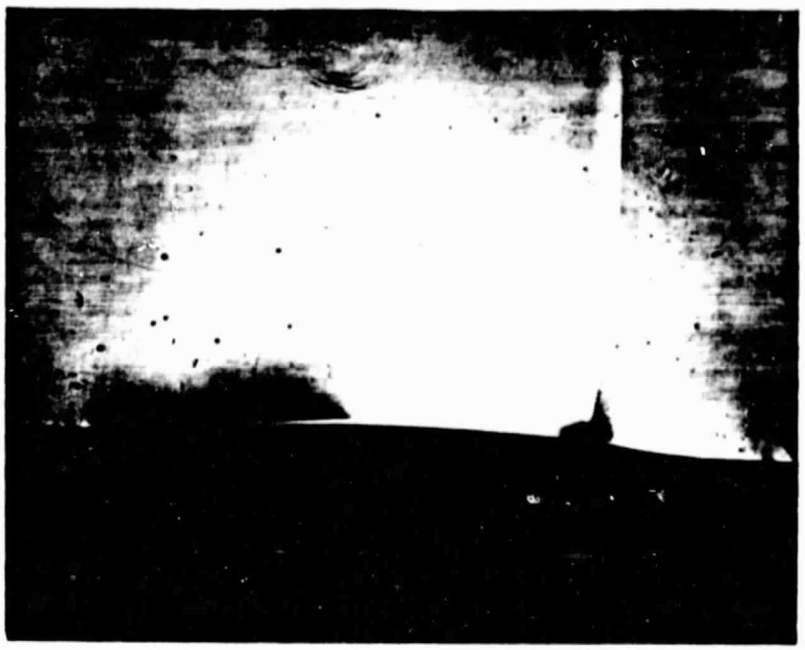

Fig.28a Schlieren photograph of flow over 12-percent-thick circular arc airfoil ,without porosity, M_∞=0.84

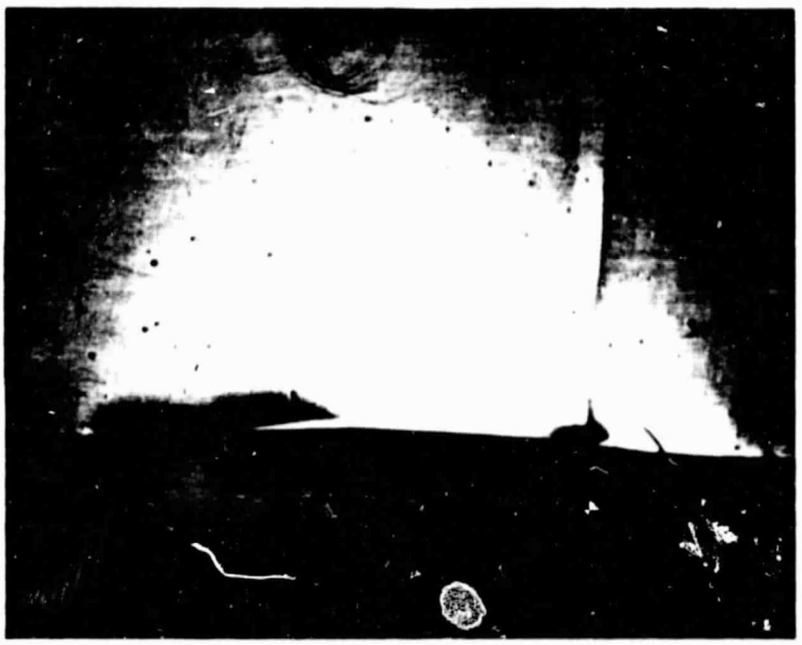

Fig.28b Schlieren photograph of flow over 12-percent-thick circular arc airfoil,with 1.17 % porosity,M_∞=0.84

porosity on the shock wave structure. An oblique shock wave, appearing at the porous surface's leading edge, meets the normal shock wave in a Lambda configuration. The initial shock wave without porosity, Fig. 28a, has been affected and its shape changed into a normal shock wave, Fig. 28b. However, the location of the terminating shock wave remains unchanged. The shadowgraph photograph, Fig. 28c, taken with the 1.17 percent model porosity, shows the same shock wave configuration.

The model Mach number distribution without the porosity and with 1.17 percent porosity indicates that the porosity decreases the local Mach number over the portion of the porous surface upstream of the shock wave location, while increasing the Mach number downstream.

1.6 Percent Porosity

The initial porosity of 1.17 percent was brought to 1.6 percent by increasing the length of the model porous surface, starting at 57 percent of the chord and ending at 80 percent. Experiments were conducted with and without porosity and the large cavity. Schlieren photographs, pressure distributions over the model, and wake surveys, were obtained. The Schlieren photograph of the flow field over the 12-percent-thick circular arc airfoil with and without porosity shows the same results as in the case of 1.17 percent porosity. Because of the porosity effect the shock wave moved slightly forward with a slight decrease in height. A related phenomena obtained from the model pressure measurements shows a decrease of the maximum local Mach number and a shift in the shock wave location, with porosity. The Mach number distribution remains unchanged upstream and downstream of the porous surface. A slight recovery of Mach

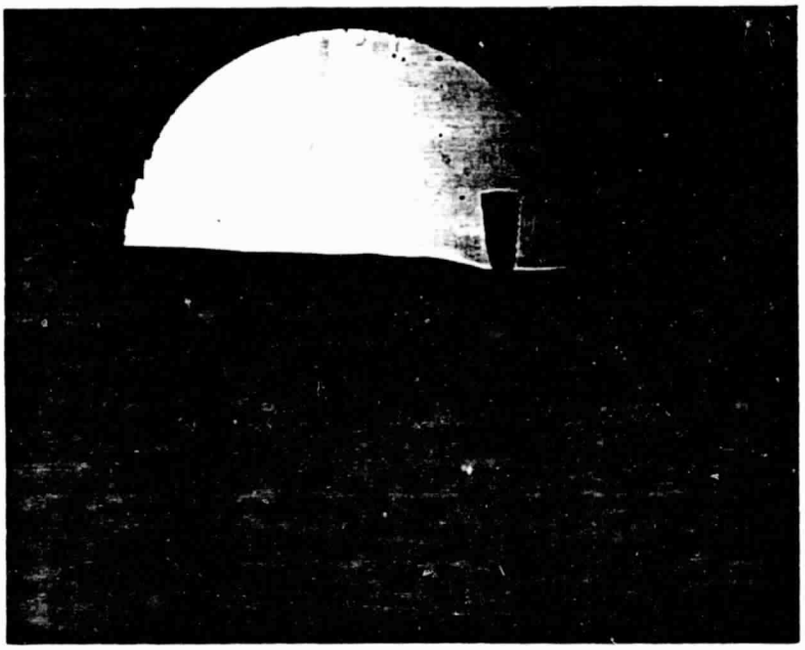

Fig.28c Shadowgraph photograph of flow over 12-percent-thick circular arc airfoil, with 1.17 % porosity, M_∞=0.84

number is noticed over the portion of the porous surface downstream of the shock wave. For a lower free stream Mach number, the surface Mach number distribution is less affected by the porosity than at higher speeds. However, there is still a slight decrease of the maximum local Mach number with porosity.

The wake survey data presented in Fig. 29, were obtained by measuring the impact pressures within the wake with a rake. The rake centerline is located at a distance of approximately 40 percent of the chord downstream of the model's trailing edge, and has 10 impact pressure probes. The wake survey starts at the test section bottom surface and extends upward to around 1.75 inches. The total pressure ratio distribution, shown in Fig. 29, is obtained by measuring the impact pressure at different vertical locations in the wake and dividing it by the total pressure of the potential flow field measured in the settling chamber. Figure 29 shows the effect of the model porosity on the impact pressure distribution. The losses of the total pressures across the shock wave are less with porosity than without, except within the boundary layer between 0 and .30 inch from the bottom surface.

To investigate the effects of model porosity on the free stream Mach number, vertical surveys of the Mach number distributions at two different locations ahead of the model were obtained. The vertical Mach number distributions were determined from the static pressures measured on the test section side wall at different vertical locations. The side wall pressure data with and without porosity, shows that there is no effect of the model porosity on the free stream Mach number.

0.94 Percent Porosity

The porosity was made smaller by decreasing the length of the model's porous surface so that it started at 61 percent of the chord from the leading edge and ended at 71 percent with the same hole size. The investigation of the passive drag control was conducted with the large cavity to study the effects of different porosities on the flow field without changing the cavity size beneath the porous surface. Schlieren photographs obtained without and with 0.94 percent model porosity, show the decrease in the shock wave height due to the effect of the porosity. The same shape Lambda shock wave was expected, but the brightness of the photograph made it impossible to confirm.

0, .94 and 1.6 Percent Porosity

Three of the previous porosity cases are compared for the same free stream Mach number and the result of the model Mach number distributions is presented in Fig. 30. As discussed previously, the no porosity case gives a higher maximum local Mach number. However, the case of 1.6 percent porosity has less effect on the Mach number distribution than the 0.94 percent case for the same cavity size. Upstream and downstream of the porous surface, the distribution is unchanged for all three cases. For the three porosity cases, the differences in the Mach number distributions around the mid-chord get smaller as the free stream Mach number decreases.

6.1.5 Effect of Cavity Length

Keeping the same 2-inch depth, the cavity was made smaller by decreasing its length in the chordwise direction. The length was changed

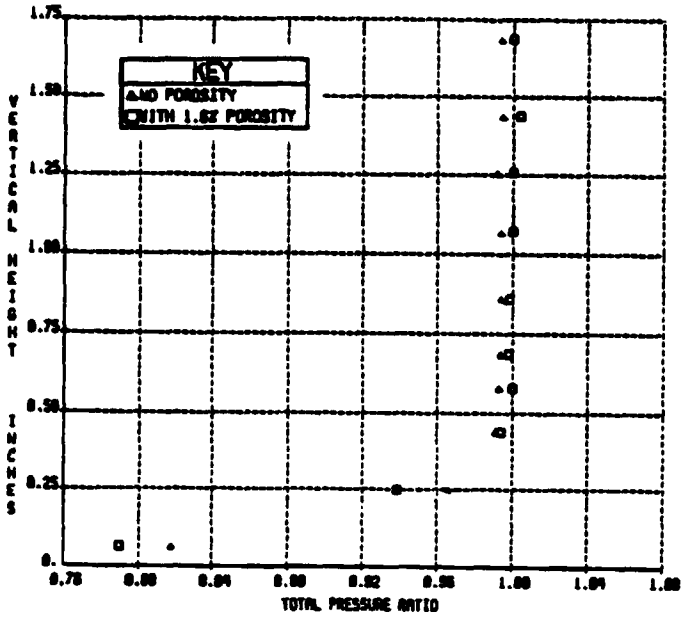

Fig.29 Wake total pressure distributions for 12-percent-thick circular arc airfoil,with and without porosity, M_∞=0.80

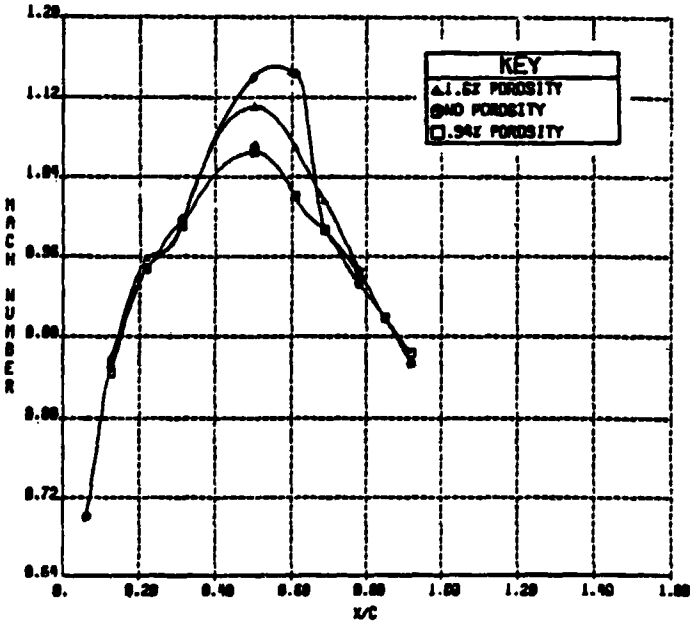

Fig.30 Mach number distributions over 12-percent-thick circular arc airfoil,without, with 0.94 and 1.6 percent porosity,M_∞=0.83

from 2.125 inches to 1.69 inches, making the new cavity dimensions 1.69 inches long by 2.50 inches wide by 2 inches deep. The study of the cavity size is mainly for practical reasons. Since the space within the wing of an airplane where the cavity will be installed is limited, a smaller cavity is preferable. Experimental data from the previous large cavity and the new smaller one are compared for the same model porosity size of 0.94 percent and the same free stream Mach number. The results are presented in Figs. 31a and b. Figure 31a shows the model Mach number distributions for a control wedge deflection at the test section exit of 0 degrees and 0.94 percent model porosity. Both distributions are similar upstream and downstream of the porous surface, but over it and around the model mid-chord, the smaller cavity gives higher distribution which corresponds to a higher lift. Figure 31b shows the impact pressure distribution measured in the wake downstream of the model trailing edge. Compared to the large cavity case, the losses of impact pressure through the shock wave is slightly less with the smaller cavity. Based on these results, the small cavity was selected for further investigation of the passive drag control concept.

6.1.6 Effect of Cavity Depth

The length and width of the small cavity are kept the same, in the following series of experiments, but the depth was changed from 2 inches to 0.25 inch. Schlieren photographs, pressure distributions over the model, and wake surveys were obtained with 0.94 percent porosity to study the effects of the cavity depth on the flow field. Figure 32 shows the Schlieren photograph of the flow field over the 12-percent-thick

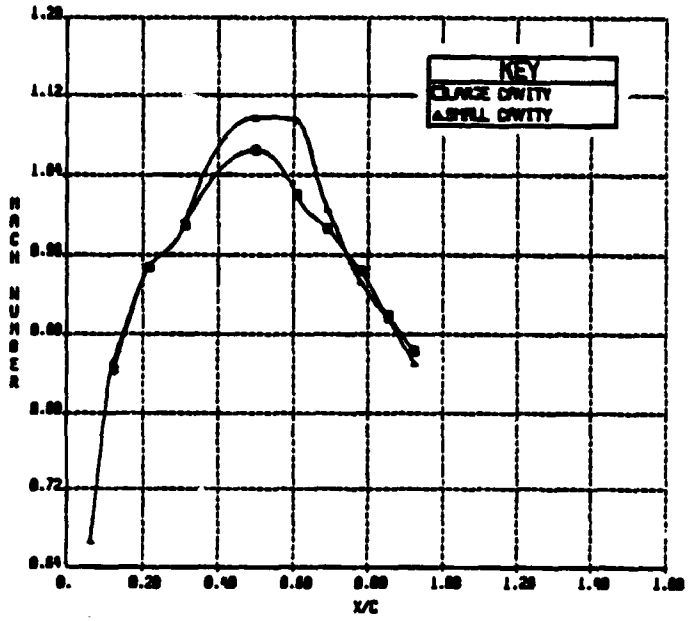

Fig.31a Mach number distributions over 12-percent-thick circular arc airfoil with large and small cavity 0.94 percent porosity, M_∞=0.83

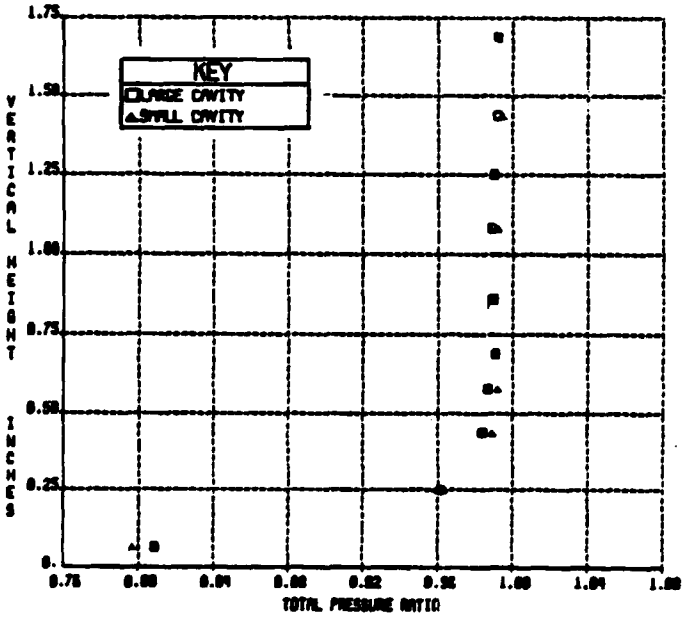

Fig.31b Wake total pressure distributions over 12-percent-thick circular arc airfoil with large and small cavity , 0.94 percent porosity, M_∞=0.83

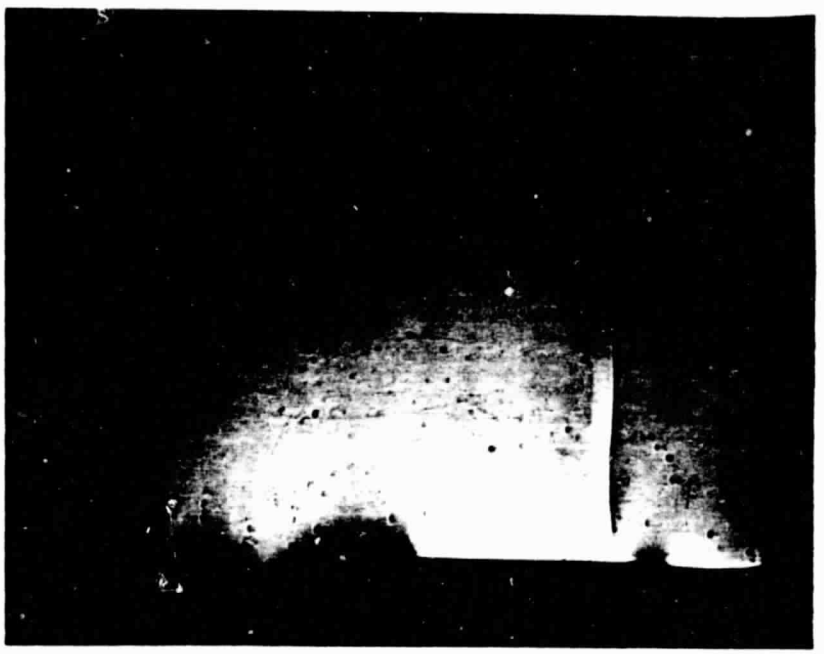

Fig.32 Schlieren photograph of flow over 12-percent -thick circular arc airfoil with 0.94 % porosity and 1/4-inch deep cavity, M_∞=0.83

circular arc. This time the Lambda shock wave shape is quite visible. The shock wave terminating the supersonic region is a straight normal shock wave of approximately 2-inch height. The oblique shock wave rising from the porous surface leading edge extends upward and meets the terminating shock wave at a distance of 0.70 inch from the model surface. The two black marks shown in the picture locate the chord of the airfoil, one mark at the model's trailing edge and one, not quite visible, at the leading edge.

The effect of the cavity depth on the model Mach number distribution is presented in Fig. 33a with a 0.94 percent model porosity and a 5 degree wedge deflection at the test section exit. The 2-inch depth produces a lower Mach number distribution which corresponds to a lift loss. This is a disadvantage in the present investigation because the objective is to achieve drag reduction with minimum lift losses. Figure 33b shows no difference in the impact pressure distribution from the wake survey for both depth cases. The surveys were made with 0.94 percent model porosity and zero degree wedge deflection at the test section exit. Based on these results, the 0.25 inch depth was selected since it minimizes the lift losses with the porous surface model.

6.1.7 Effect of Large Model Porosity with Small Cavity

The 0.94 percent model porosity was increased to 2.04 percent by enlarging the diameter of the porous surface holes from 0.021 inch to 0.031 inch. The pressure distribution over the model as well as the impact pressures from the wake were obtained. The results were compared against the no porosity and the previous 0.94 percent porosity case.

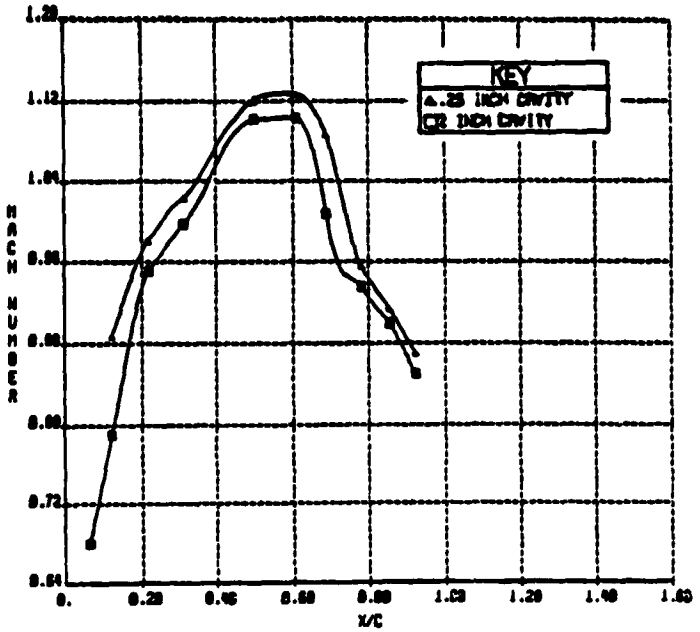

Fig.33a Mach number distributions over 12-percent-thick circular arc airfoil with 0.25 and 2-inch cavity depth, 0.94 percent porosity, M_∞=0.83

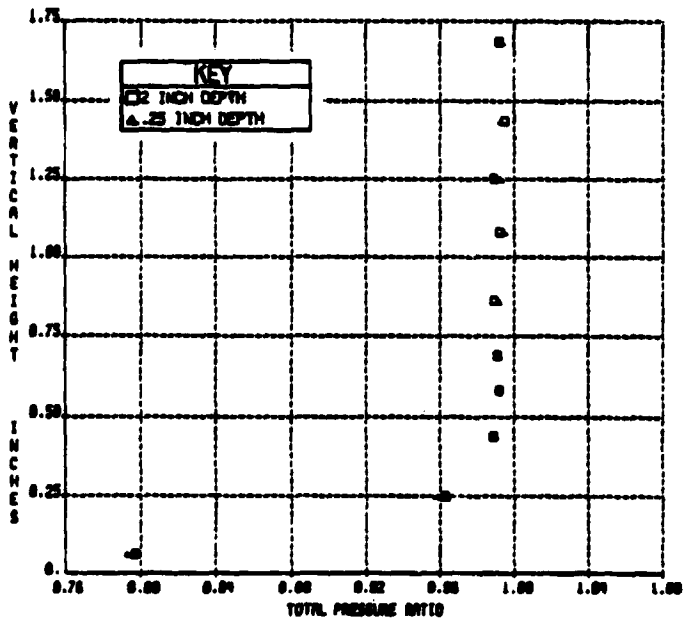

Fig.33b Wake total pressure distributions for 12-percent-thick circular arc airfoil with 0.25 and 2-inch cavity depth, 0.94 percent porosity, M_∞=0.83

Figure 34a shows the pressure coefficient distribution over the model for 0.824 free stream Mach number. From the model's leading edge up to 30 percent of the chord, the pressure distribution remains unaffected by the porosity. Between 30 to 60 percent of the chord, both 0.94 percent and 2.04 percent porosities slightly increase the pressure coefficient values similarly. Beyond that point, the 3 distributions align again with slightly lower values for the 2.04 percent case. The tests were conducted with the removal of the boundary layer so that the new boundary layer would start at the airfoil leading edge stagnation point. A 0.22 inch thick rake with 10 impact pressure probes, was used for the wake survey. Figure 34b shows the point drag distribution for the three model porosities of 0, 0.94 and 2.04 percent. The point drag coefficient is derived using Eq. (26). For a free stream Mach number of 0.827, the porous model surface induces a slight drag reduction; however, increasing the porosity from 0.94 to 2.04 percent has negligible effects on the drag distribution, as shown in Fig. 34b.

6.1.8 Effect of the Rake Blockage

Because of the blockage effects at transonic speeds, where most of the actual tests are conducted, the thick rake was replaced by a thin one so that the effect of the rake would be minimized. The tests indicated the effect of the rake size on the model Mach number distribution. The thinner rake yielded the higher model Mach number distribution, although the distribution remained unaffected over the first 30 percent of the chord. The tests were conducted with a free stream Mach number of 0.828, a model porosity of 2.04 percent, and the small cavity of 0.25

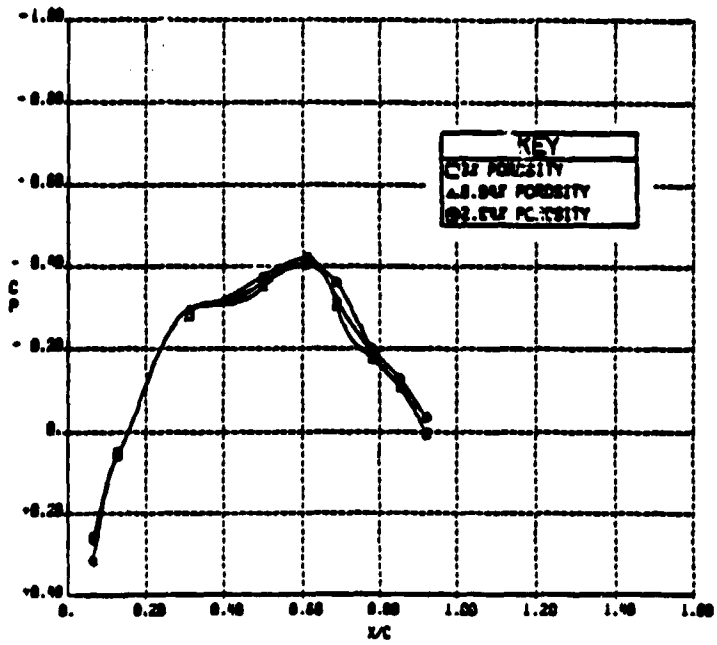

Fig.34a Pressure coefficient distributions over 12-percent-thick circular arc airfoil without,with 0.94 and 2.04 percent porosity,and 1/4-inch deep cavity, M_∞=0.83

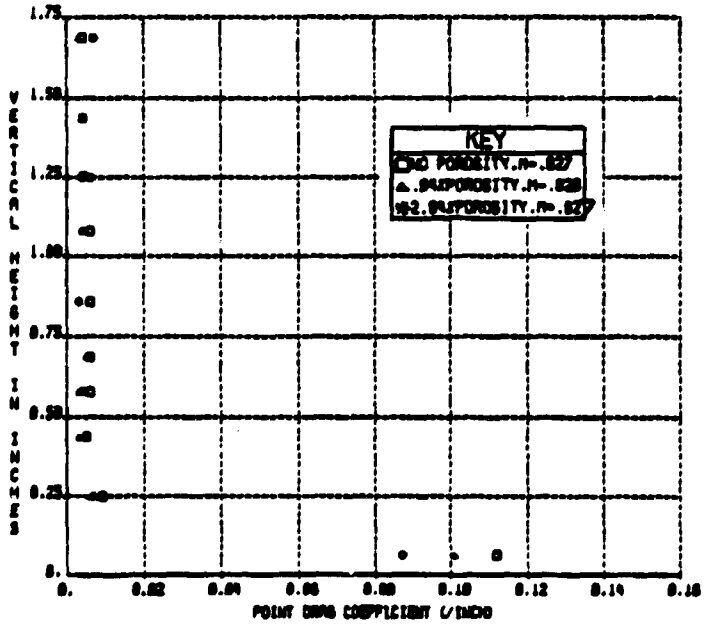

Fig.34b Local drag coefficient distributions for 12-percent-thick circular arc airfoil without,with 0.94 and 2.04 percent porosity,and 1/4-inch deep cavity

inch deep.

6.1.9 Effect of the Thin Rake Position

The thin rake selected for the remaining experimental tests consists of 8 impact pressure probes of .031 inch diameter each, with a total height of .875 inch and a thickness of .063 inch. For the complete experimental data within the wake downstream of the model, the vertical survey was made in 2 steps. The rake was first positioned at the test section bottom surface and then was moved vertically to a position such that it covered the necessary height for a complete wake survey, overlapping a couple of the impact pressure probes between the 2 positions. To check the effect of the rake's vertical position on the flow field, pressure data were obtained with a model porosity of 2.04 percent and with the removal of the boundary layer. The tests showed practically no effect of the rake position on the model Mach number distribution.

6.2 Flow Over Supercritical Airfoil

A 14-percent-thick NASA supercritical airfoil,[12] with a 4-inch chord was constructed and used in the investigation of passive drag control. The supercritical airfoils, now being used for the current generation of aircraft, are shaped to reduce the drag associated with energy losses due to the shock wave and flow separation at transonic speeds. However, despite this advantage of drag reduction over the conventional airfoils, a strong viscous interaction between the shock wave and the boundary layer still occurs, and the need to control it is more necessary today than it has been in the past to achieve a new generation of more

efficient aircraft. The research described in this section will focus on this problem. The present supercritical airfoil, designed for a normal force coefficient of 0.7, was mounted on the middle of the first 20-inch test section bottom surface. Seventeen pressure taps, spread along the model surface centerline, were installed to measure the static pressure distribution. Before the model surface was made porous, preliminary tests were conducted with the smooth surface. Schlieren photographs and pressure distributions, as well as wake surveys, were obtained for a range of free stream Mach numbers. Similar tests, with the exception of the Schlieren photographs, were conducted by NASA on the same type of airfoil with the smooth surface corresponding to the no porosity case. The comparison of the results is discussed in the following section.

6.2.1 Smooth Model Surface Test Results

In the tests conducted in the 3-inch by 15.4-inch RPI test section over the 14-percent-thick supercritical airfoil at a free stream Mach number of 0.84, the boundary layer removal has no effect on the shock wave location, as evidenced by the Schlieren photographs. Figure 35 shows expansion waves in the supersonic region over the model surface, terminated by a strong shock wave of approximately 2.46 inch in height, and located at 77 percent of the chord. The expansion waves, departing from the airfoil surface, meet the sonic line bounding the embedded supersonic zone and are reflected as compression waves back to the model surface. The expansion waves are diverging, while the compression waves are converging. When these compression waves finally coalesce, they form a strong shock

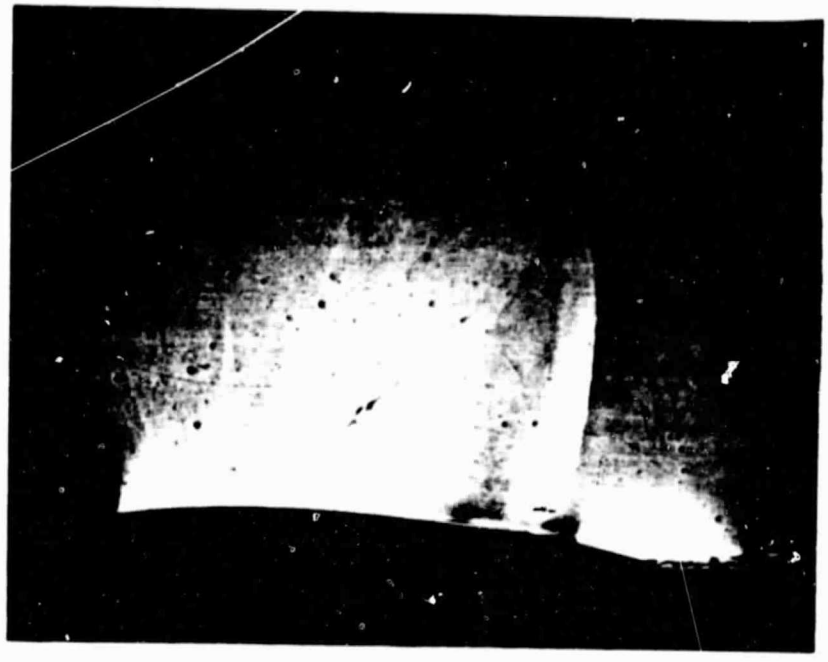

Fig.35 Schlieren photograph of flow over 14-percent-thick smooth surface supercritical airfoil, $M_{\infty}=0.804$

wave which terminates the supersonic region. This strong shock wave of large height and the expansion waves starting within 23 percent of the chord from the leading edge, define a large embedded supersonic region, bounded by the sonic line, the model surface, and the terminating shock wave.

Static pressures were measured on the surface of the model and used to determine the local Mach number distribution for a range of free stream Mach numbers. The surface pressure measurements were obtained from a chordwise row of orifices located along the model centerline. Orifices were concentrated near the airfoil leading edge to define the stagnation point as well as the pressure gradient in this region.

The chordwise Mach number distribution, shown in Fig. 36, indicates the similarity between NASA's results[18] and the present experimental data, with a descrepancy in the similarity around the trailing edge, where the NASA values of the Mach numbers are lower. Both Mach number distributions show the same maximum local Mach number of 1.26 at the same location, and the same shock wave location. NASA experiments in this case were conducted with a free stream Mach number of 0.78 and a normal force coefficient C_n of 0.51. However, with a lower free stream Mach number of 0.74 and a C_n of 0.26, the two Mach number distributions are shown to be more alike, even in the trailing edge region, Fig. 37. Here, the maximum local Mach number is unity, and the graph of the distributions is flatter, indicating a more constant distribution than in the previous case of M_∞ equal to 0.78. The model was mounted on the test section bottom wall, Fig. 8b. Consequently, only the upper surface and the leading edge were

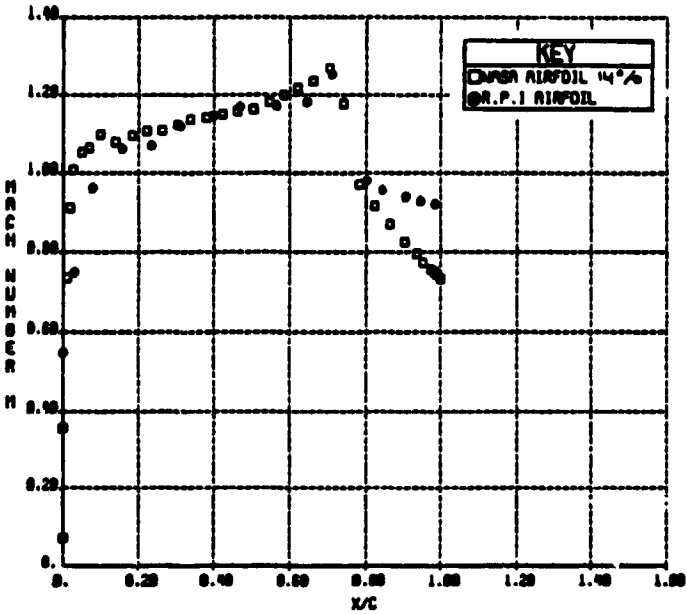

Fig.36 Mach number distributions over R.P.I and NASA 14-percent-thick supercritical airfoils without porosity, M_{∞}=0.80

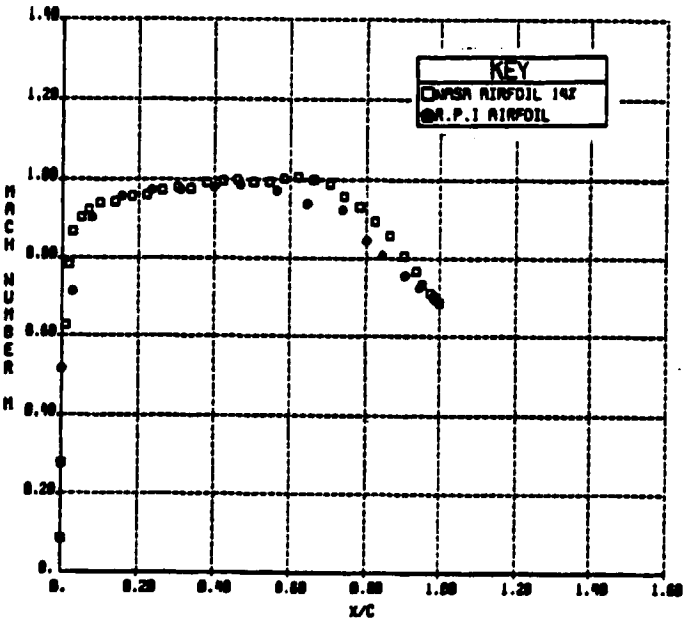

Fig.37 Mach number distributions over R.P.I and NASA 14-percent-thick supercritical airfoils without porosity, M_{∞}=0.74

investigated, with only one pressure measurement taken on the model bottom surface at a distance of 3 percent of the chord from the leading edge. The Mach number at this point was compared to the NASA bottom surface distribution for a free stream Mach number of 0.74. Because of the deficiency in the removal of the boundary layer at the model leading edge, the presently obtained value is higher than NASA's.[18] The removal was not adequate; therefore, the new boundary layer did not start at the model's stagnation point, Fig. 38 .

As the free stream Mach number decreases to .65, Fig. 39 indicates a more constant Mach number value of .81, from near the leading edge to 70 percent of the chord. Compared to NASA's results, both distributions coincide practically from the leading edge to the trailing edge. Again, for a free stream Mach number of 0.65, the value of the pressure coefficient obtained on the airfoil bottom surface near the leading edge is lower compared to the NASA bottom surface results for the same reasons of the boundary layer removal as discussed previously.

Impact pressure data within the wake downstream of the model's trailing edge were obtained for different free stream Mach numbers using the thin rake. To obtain the section drag coefficient, Eq. (25), the point drag coefficients were computed for each total pressure measurement in the wake, by using Eq. (26). These point drag coefficients were then summed by numerical integration across the wake, based on the trapezoidal method. Figure 40a shows a good drag distribution over a wide range of free stream Mach numbers, with no measurable shock losses up to the drag divergence Mach number of approximately 0.76. Figure 40a also

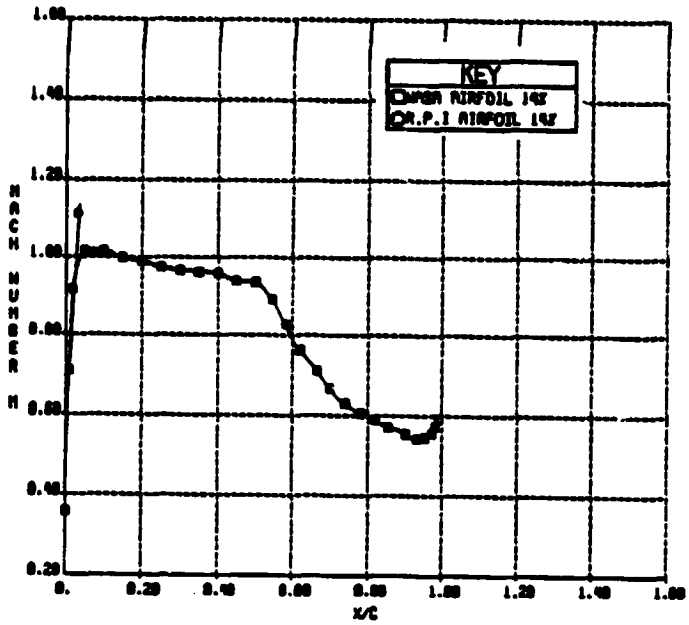

Fig.38 Bottom surface Mach number distributions of R.P.I and NASA 14-percent-thick supercritical airfoils without porosity, M_∞=0.74

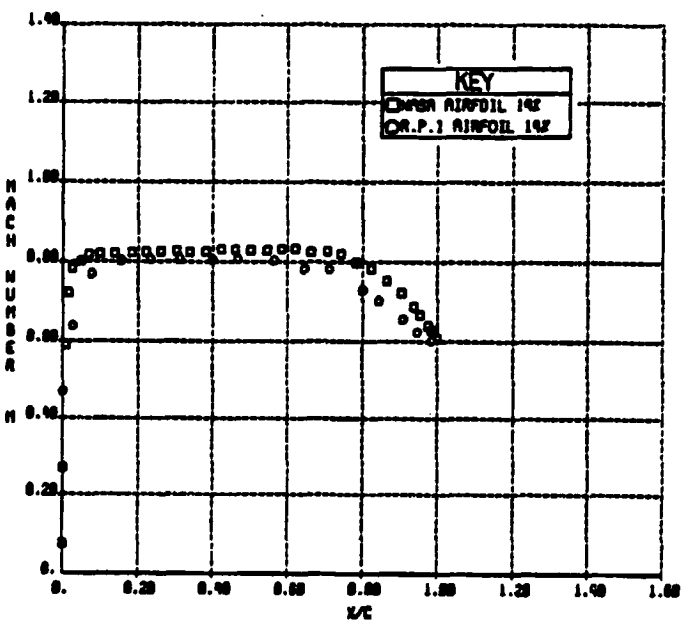

Fig.39 Mach number distributions over R.P.I and NASA 14-percent-thick supercritical airfoils without porosity, M_∞=0.65

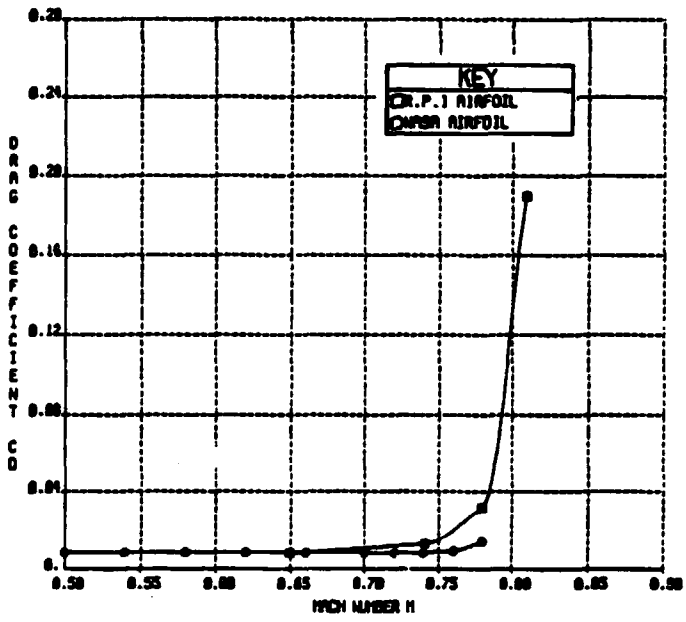

Fig.40a Variation of measured section drag coefficient with Mach number for R.P.I and NASA 14-percent-thick supercritical airfoils

shows the NASA results with a slightly higher drag divergence Mach number. The variation of the section drag coefficient with the free stream Mach number, with and without model porosity is presented in Fig. 40b.

The overall Mach number distributions for a range of free stream Mach numbers show in general good agreement with the results presented in Fig. 18. From these experimental results, the location of the porous surface on the 14-percent-thick supercritical airfoil was selected so that the shock wave would be standing in the middle. The experiments on the previous 4-inch chord circular arc airfoil were used as a guide for this next phase of the supercritical airfoil investigation. Consequently, 2.5 percent porosity with a 3/4-inch cavity beneath it was selected, as well as the thin rake for the wake survey downstream of the airfoil trailing edge. The experimental results are discussed in the following section.

6.2.2 Effect of Model Porosity with Large Cavity

2.5 Percent Porosity

The model's surface was made porous by drilling 0.025 inch diameter holes perpendicular to the surface. The porous surface, consisting of 18 spanwise rows with 38 holes each, is located between 56 percent and 83 percent of the chord from the airfoil leading edge. Based on the model surface area, the porosity is defined as the ratio between the total area of the porous surface holes and the area of the model. Consequently, the corresponding porosity of the above geometry is 2.5 percent. The cavity beneath the porous surface was made 3/4 inch deep, 3 inches wide and 1.08 inches long. The lengths of the cavity and the porous surface, in the chordwise direction, are the same for the case of 2.5 percent porosity. The holes of the porous surface can be either sealed or enlarged to obtain

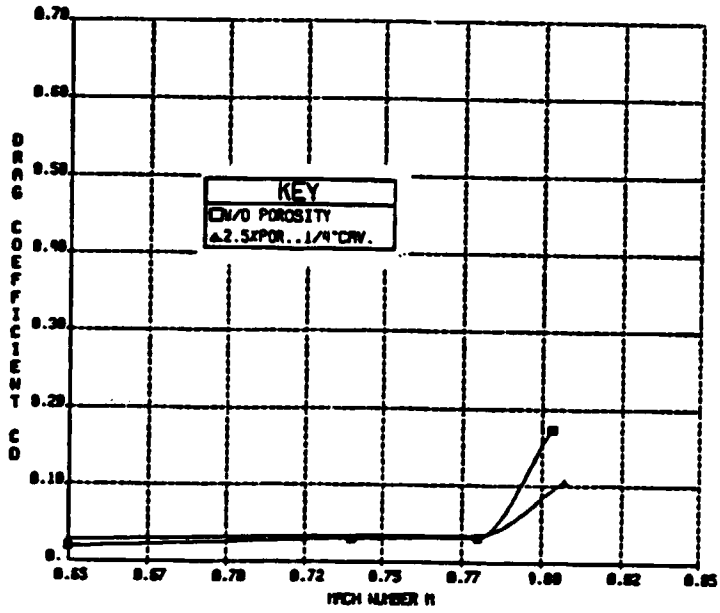

Fig.40b Variation of section drag coefficient with Mach number,with and without porosity

the desired porosity. The model's surface is made non-porous by sealing all the holes. Schlieren photographs, pressure distributions and wake surveys were obtained without and with the 2.5 percent porosity for a range of free stream Mach numbers.

The Schlieren photographs taken with a free stream Mach number of .806, shown in Figs. 41a and b, indicate a sizable change in the shock wave structure due to the effect of the model's porosity. As discussed previously, the porous surface with the cavity permits a part of the boundary layer to move from downstream to the upstream of the shock wave, sending compression waves which produce an oblique shock wave. The oblique shock wave originating from the porous surface leading edge reaches the terminating shock wave at a distance of 1.23 inches from the model surface. The location of the terminating shock wave in the middle of the porous surface, 80 percent from the leading edge, was not affected by the porosity; its shape, however, was changed into a normal shock wave. Expansion waves can be seen in both Schlieren photographs, with and without the porosity, upstream of the shock wave near the model leading edge, indicating the presence of a large embedded supersonic region. The thick black mark in the pictures indicates the location of the model's trailing edge. The leading edge is not quite visible because of the stress concentration in that region of the plexiglass side walls. The two thin black marks approximate the location of the porous surface on the model.

As the free stream Mach number decreases to 0.78, the Schlieren photographs, Figs. 42a and b, without and with the 2.5 percent porosity respectively, show the effect of the porosity on the location of the shock

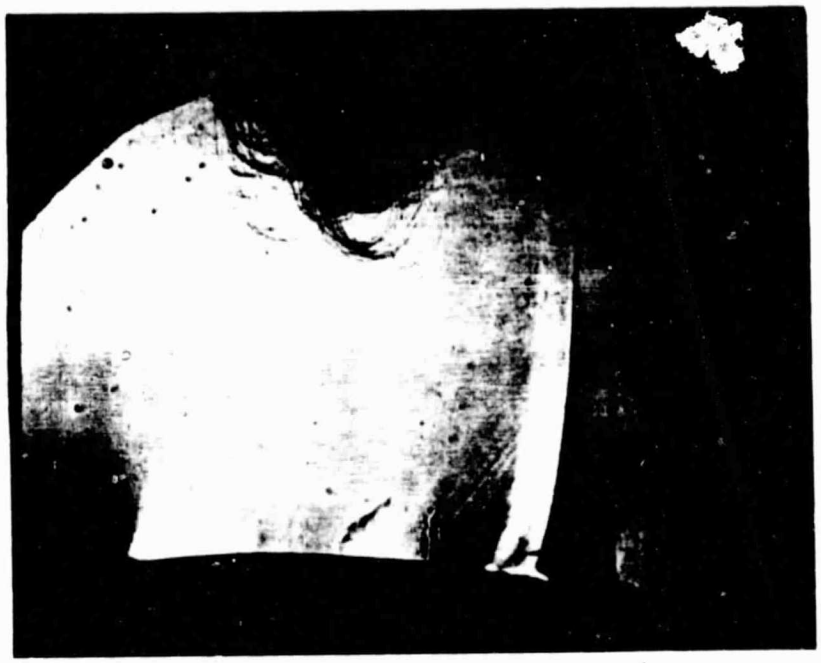

Fig.41a Schlieren photograph of flow over 14-percent-thick supercritical airfoil,without porosity,M_∞=0.806

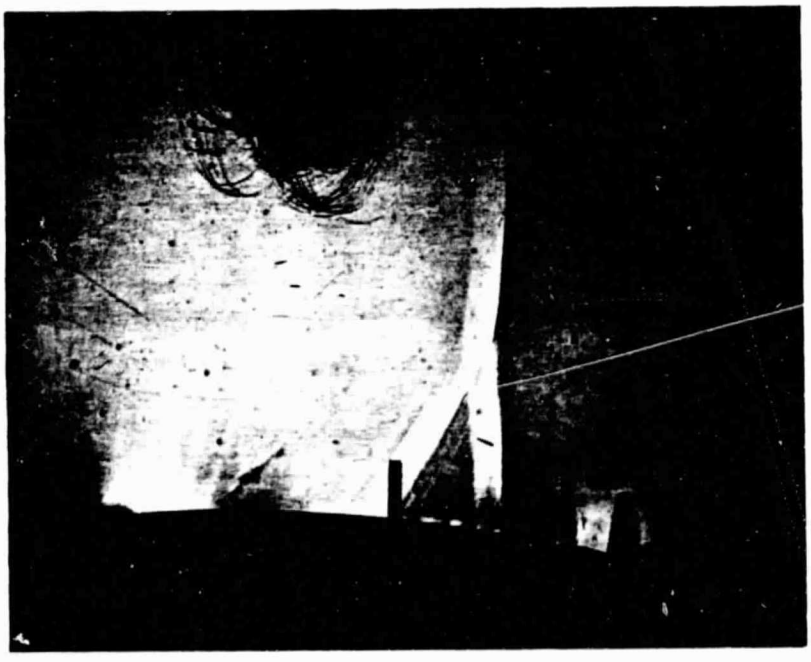

Fig.41b Schlieren photograph of flow over 14-percent-thick supercritical airfoil,with 2.5% porosity,3/4-inch cavity,M_∞=0.806

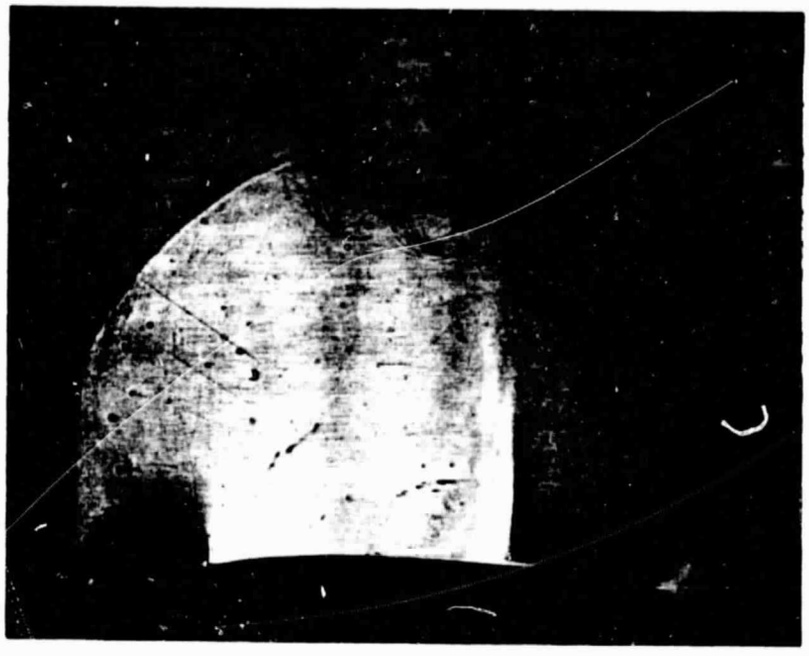

Fig.42a Schlieren photograph of flow over 14-percent-thick supercritical airfoil,without porosity,M_∞=0.78

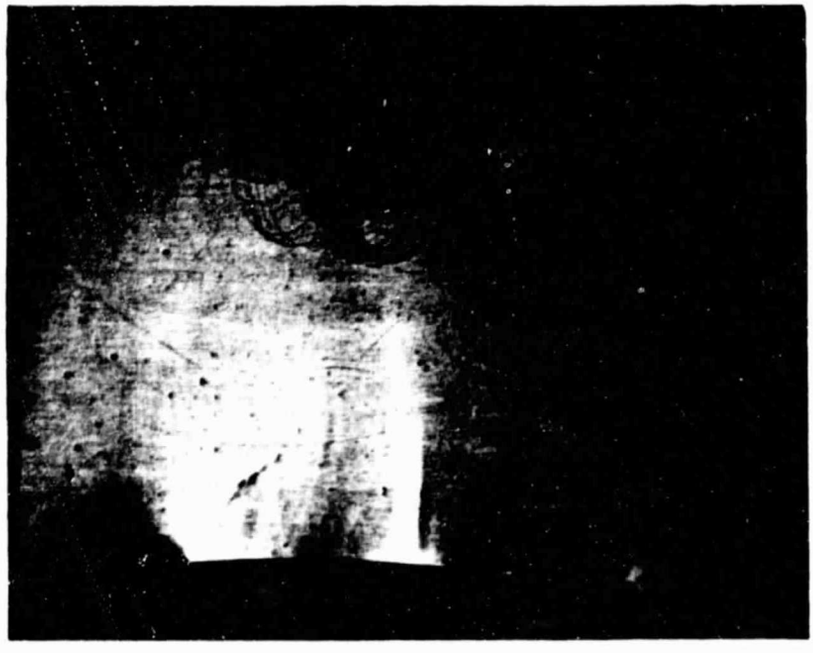

Fig.42b Schlieren photograph of flow over 14-percent-thick supercritical airfoil,with 2.5% porosity,3/4-inch cavity, M_∞=0.78

wave and its strength. The shock wave moved upstream from 62 to 57 percent of the chord. Its shape, however, remained a single normal shock wave with a decrease in the height from 1.23 to 1.10 inches, corresponding to a reduction in its strength, as well as a reduction in the size of the embedded supersonic region. The shock wave was still over the porous surface. With further reductions in the free stream Mach number, the shock wave disappeared, as shown in Fig. 43 for a Mach number of 0.74.

The Mach number distributions were obtained from the pressure measurements over the model surface. The distributions with 2.5 percent porosity and without porosity, at, respectively, 0.806 and .803 free stream Mach numbers, were compared. The Mach number distribution remained unaffected by the porosity up to the mid-chord location. The porosity effects began to appear when the values of the Mach number were decreased up to the location of the shock wave at nearly 80 percent of the chord. The maximum Mach number, located close to the mid-chord, was decreased from 1.23 to 1.18. Downstream of the shock wave, the Mach number was higher with the porosity than without, which corresponded to a decrease in the local pressure, and led to a reduced flow separation. For better comparison the Mach number distributions of 2.5 percent and no porosity cases were compared again, but this time for the same free stream Mach number of 0.806, as shown in Fig. 44a. The same observations as before were made here, except that the no porosity case gave a higher maximum Mach number of 1.26 instead of 1.23 due to a higher M_∞, and that the two distributions aligned at the model's trailing edge. The corresponding pressure coefficient distributions are shown in Fig. 44b.

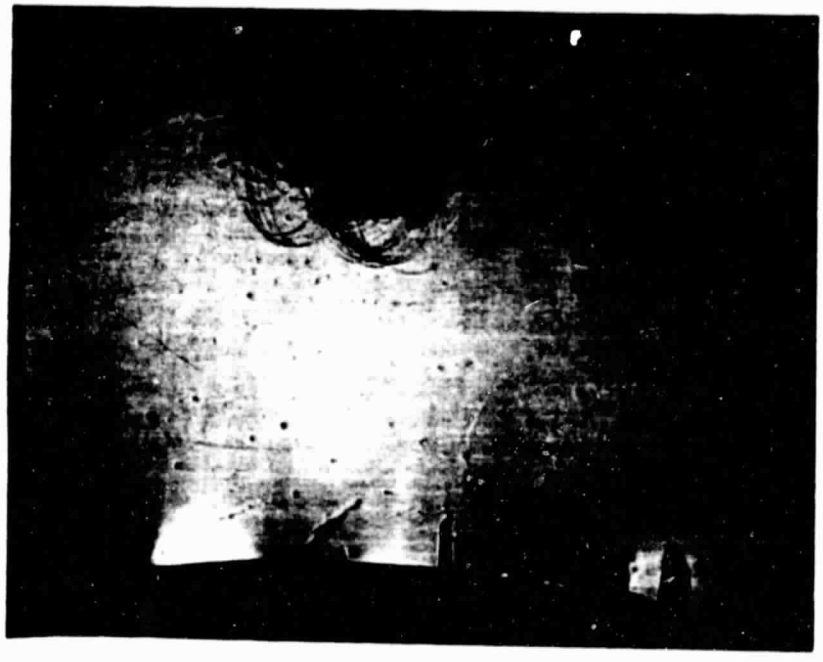

Fig.43 Schlieren photograph of over 14-percent-thick supercritical airfoil without porosity, M_∞=0.74

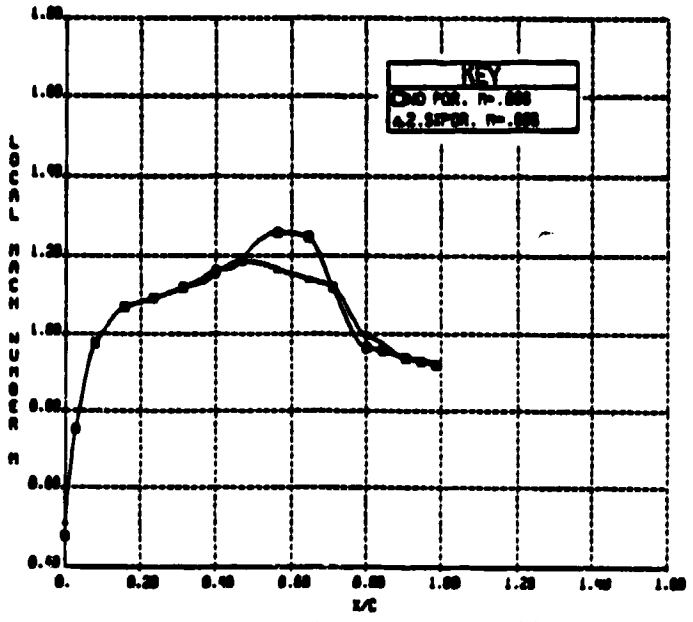

Fig.44a Mach number distributions over 14-percent-thick supercritical airfoil without and with 2.5 percent porosity,3/4-inch deep cavity. M_∞=0.806

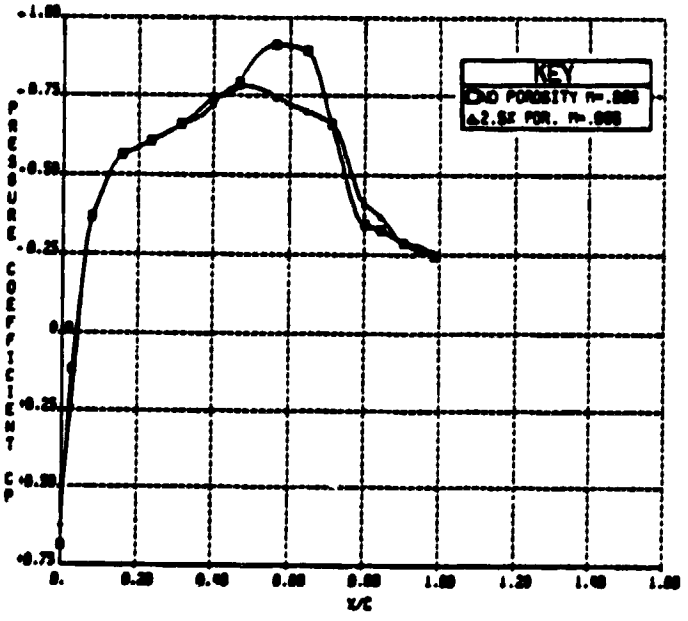

Fig.44b Pressure coefficient distributions over 14-percent thick supercritical airfoil without and with 2.5 percent porosity,3/4-inch deep cavity, M_∞=0.806

For a Mach number of 0.78, the results presented in Fig. 45a show similar effects of the porous surface on the Mach number distribution, as well as for the higher free stream Mach number of 0.806. The distribution remained unaffected from the leading edge to the model mid-chord, and then decreased over the porous surface upstream of the shock wave location at around 60 percent of the chord. Downstream of the shock wave, the porosity increased the Mach number and minimized the flow separation phenomenon.

For a Mach number of 0.74, the effects of the porosity on the Mach number distribution started 25 percent farther upstream than the case of higher Mach number and extended downstream to the end of the porous surface. The effects were then insignificant until the trailing edge, where the Mach number became higher with porosity, as shown in Fig. 45b. The flow was fully subsonic over the model surface, with a relatively constant Mach number distribution between 20 and 50 percent of the chord.

As the free stream Mach number was decreased to 0.65, the Mach number distributions, shown in Fig. 45c, became flatter between 17 and 60 percent of the chord, with a nearly constant value of 0.81 for the no porosity case, and 0.79 for the 2.5 percent case. The comparison between the two distributions remained the same as in the previous higher Mach number condition.

To investigate the effect of the airfoil porous surface on the drag reduction, drag coefficient distributions were obtained from impact pressure measurements in the wake downstream of the model trailing edge as shown in Figs. 4 and 9. The experiments were conducted for a series

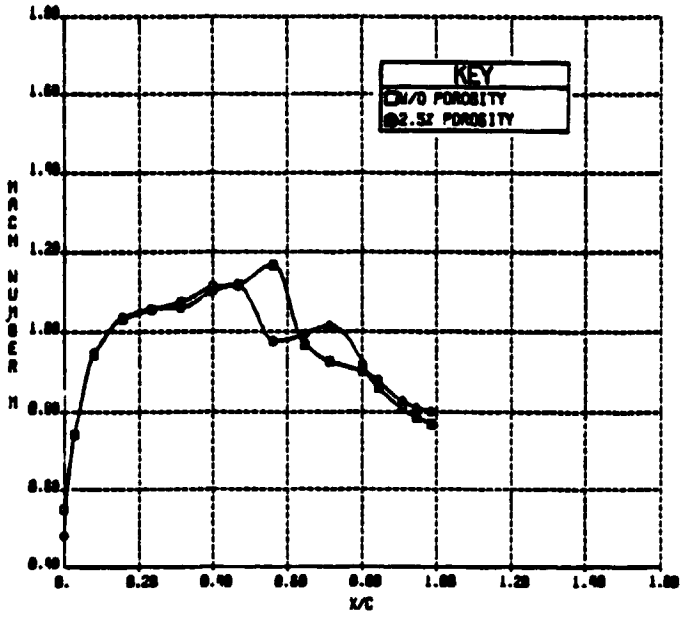

Fig.45a Mach number distributions over 14-percent-thick supercritical airfoil without and with 2.5 percent porosity, 3/4-inch cavity, M_∞=0.78

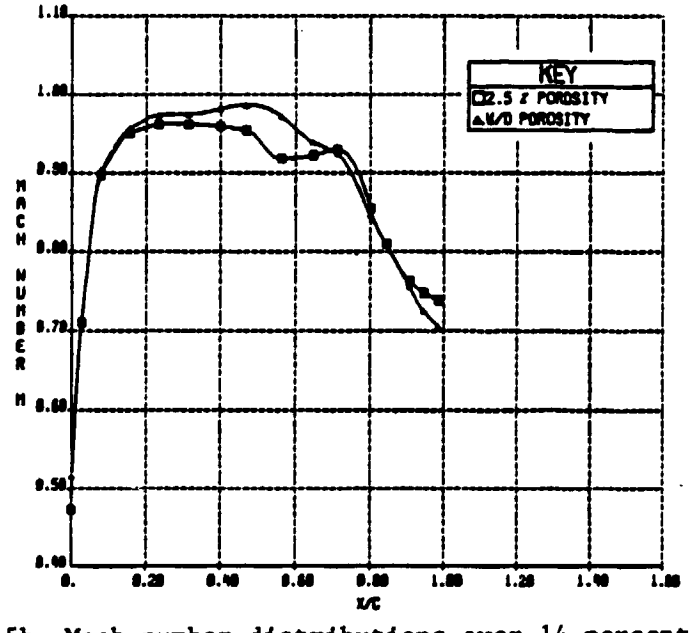

Fig.45b Mach number distributions over 14-percent-thick supercritical airfoil without and with 2.5 percent porosity, 3/4-inch cavity, M_∞=0.74

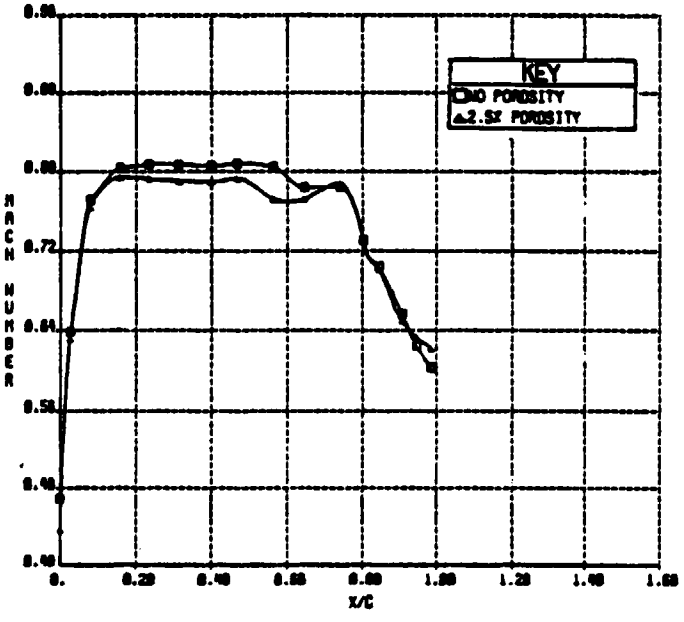

Fig.45c Mach number distributions over 14-percent-thick supercritical airfoil without and with 2.5 percent porosity, 3/4-inch deep cavity, M_∞=0.65

of free stream Mach numbers. For a free stream Mach number of 0.807, the point drag coefficient distributions,[25] indicated a lower drag distribution with 2.5 percent porosity than with the no porosity case throughout the survey height, except within the boundary layer between 0 and 0.25 inch. The difference in the local drag of the porous and non-porous surfaces decreased as the height increases. The two drag distributions finally align at a height of approximately 1.75 inches. The numerical integration of the point drag coefficients across the 1.75 inch height showed a net drag reduction due to the airfoil porous surface. The tests, repeated for approximately the same free stream Mach number of 0.806, showed similar drag coefficient distributions, with a drag reduction. The same observation was obtained, from Fig. 46a, with the free stream Mach number of 0.803 for the no porosity case and 0.806 for the 2.5 percent porosity one. Even though the Mach number with the no porosity case was lower than with the 2.5 percent case, there was still a net drag reduction over the airfoil upper surface of 15 percent due to the model porosity. The corresponding impact pressure distributions are shown in Fig. 46b.

As the free stream Mach number was decreased to 0.78 for both cases, with and without porosity, there was a drag reduction with porosity, except within the first 0.25 inch of the wake survey height where the drag was higher, Fig. 46c . The point drag distribution decreased as the height increases and finally vanished at a height of 0.80 inch for both with and without porosity cases. At this free stream Mach number of 0.78, the net drag was higher with the porous surface.

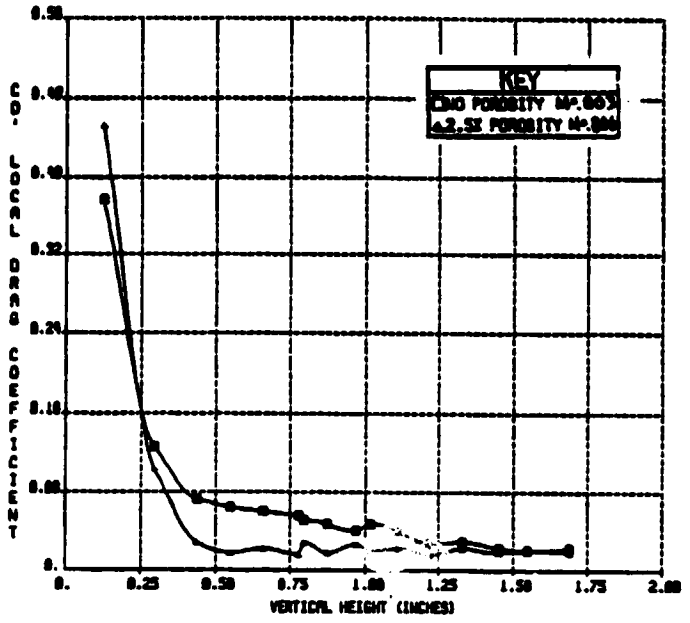

Fig.46a Local drag coefficient distributions for 14-percent-thick supercritical airfoil without and with 2.5 percent porosity,3/4-inch deep cavity

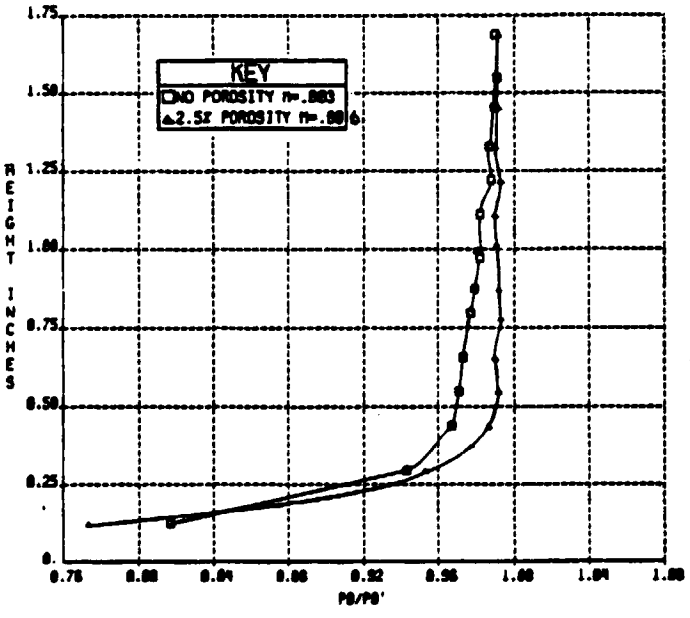

Fig.46b Wake total pressure distributions for 14-percent-thick supercritical airfoil without and with 2.5 percent porosity,3/4-inch deep cavity

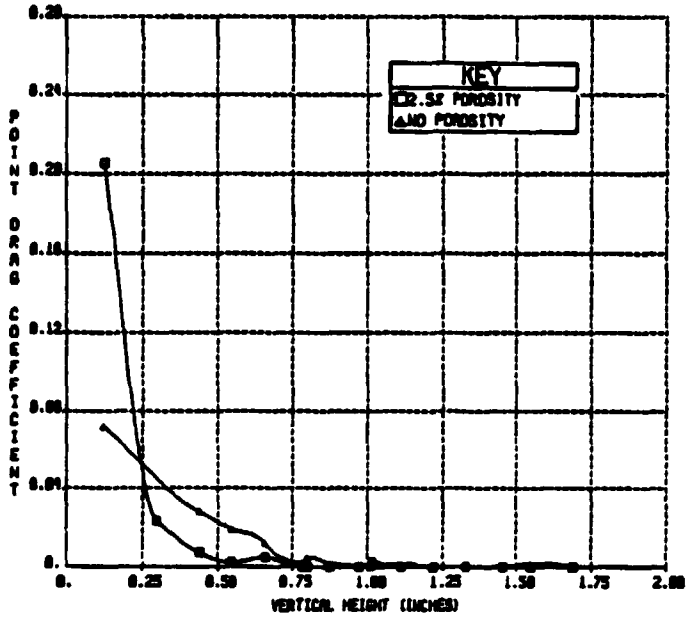

Fig.46c Local drag coefficient distributions for 14-percent-thick supercritical airfoil without and with 2.5 percent porosity, 3/4-inch deep cavity M_∞=0.78

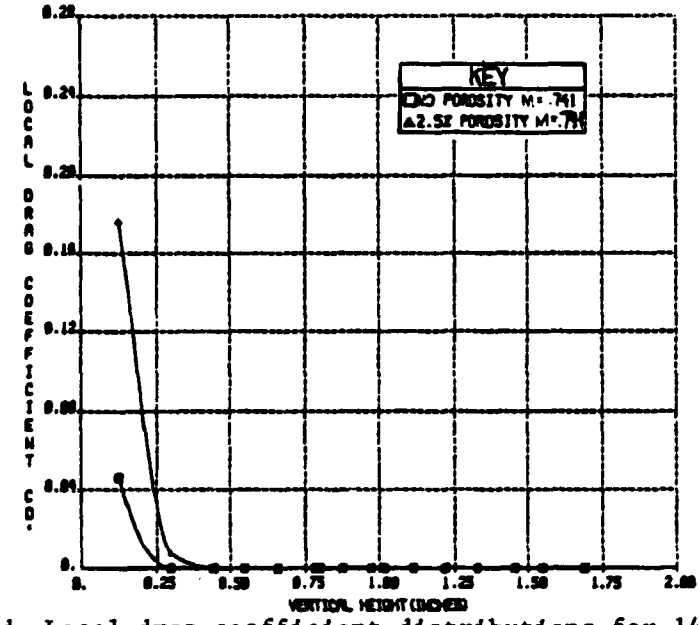

Fig.46d Local drag coefficient distributions for 14-percent-thick supercritical airfoil without and with 2.5 percent porosity, 3/4-inch deep cavity M_∞=0.741

At a Mach number of 0.741, the results presented in Fig. 46d indicated a higher drag with the porous surface. The two point drag coefficient distributions decreased rapidly within the first 0.25 inch and vanish for approximately the rest of the height, indicating a shock-free flow over the model as shown in the corresponding Schlieren photograph, Fig. 43, discussed earlier.

Consequently, at transonic Mach numbers inducing a strong shock wave, the 2.5 percent model porous surface with a 3/4-inch cavity does reduce the profile drag over the airfoil. However, at subsonic speeds at which the shock wave vanishes and where there is no wave drag, the drag is higher.

More data with the 3/4-inch deep cavity were obtained, but for a smaller porous surface of 1.25 percent, the results are presented in the following section.

1.25 Percent Porosity

To investigate the effect of porosity size on the shock wave/boundary layer interaction and on the flow field, the 2.5 percent surface porosity was reduced to 1.25 percent by sealing every other hole. The cavity dimensions were kept the same. Experimental tests were conducted for a series of free stream Mach numbers ranging from transonic to subsonic speeds. Schlieren photographs, pressure distributions and wake surveys were obtained with the new porosity and same cavity size.

The Schlieren photograph taken for M_∞ of 0.807, shows a normal shock wave with a 2.4 inch height, terminating the local supersonic region at 80 percent of the chord. A series of compression waves emanating from

the porous surface met the terminating shock wave within a height of 1.22 inches. Expansion waves were also seen within the supersonic zone downstream of 24 percent of the chord. Their expansion into the flow field as well as the height of the terminating shock wave indicated the presence of a large local supersonic region. Compared to the no porosity case, Fig. 47a, the change of the shock wave shape into a normal one and the appearance of the compression waves over the porous surface, indicated the effect of the porosity on the flow field. However, the effect on the terminating shock wave location was negligible.

For a slightly lower free stream Mach number of 0.804, the effect of the compression waves originating from the porous surface on the shape of the terminating shock wave was noticeable, as shown in Figs. 47a and b. Beside the change into a normal shape, the compression waves had a tendency to pull upstream the point of intersection with the terminating shock wave. Expansion waves close to the model leading edge and a normal terminating shock wave of 2.34 inches height located at 78 percent of the chord indicated the presence of a large local supersonic region embedded in a subsonic flow. The effect of the porous surface on the terminating shock wave location was negligible, as indicated in Figs. 47a and b.

For a subsonic free stream Mach number of 0.78, the porosity effect on the terminating shock wave location, at the beginning of the porous surface, was negligible. However, a decrease in the height from 1.43 to 1.17 inches was produced as shown in Figs. 47c and 42a. Expansion waves between the 37 percent chord point and the normal shock wave defined

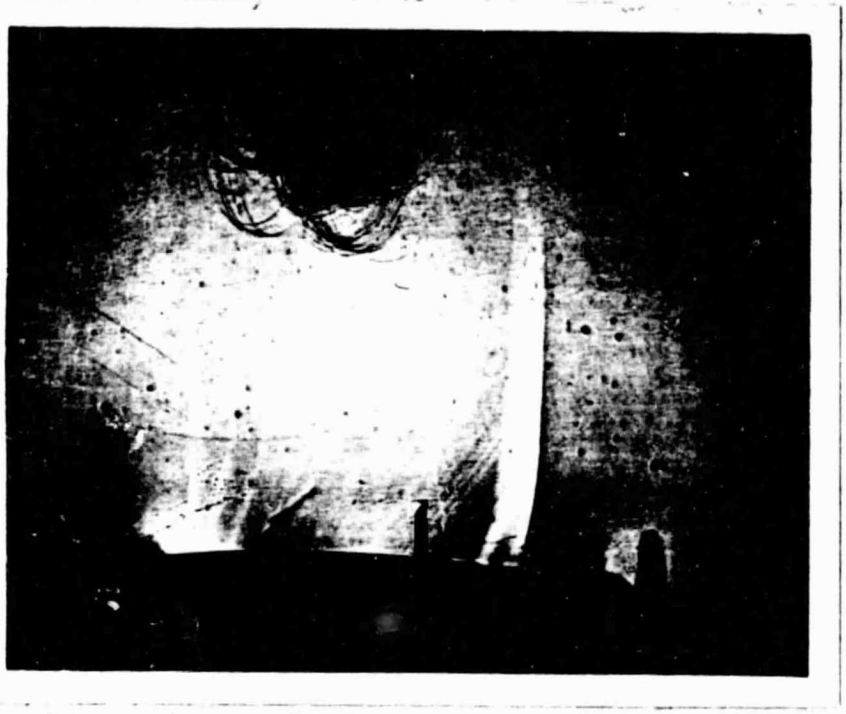

Fig.47a Schlieren photograph of flow over 14-percent-thick supercritical airfoil,without porosity,3/4-inch cavity, M_∞=0.803

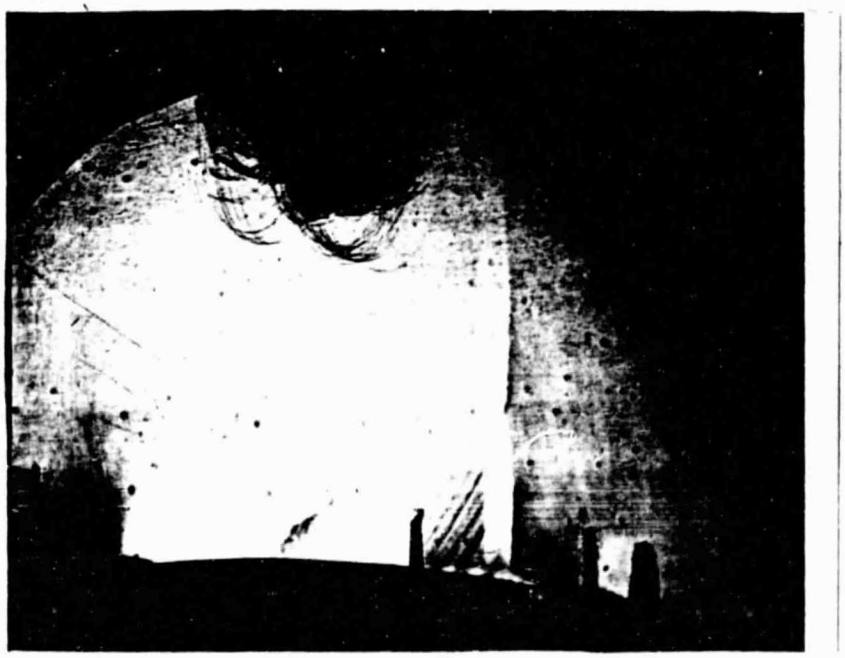

Fig.47b Schlieren photograph of flow over 14-percent-thick supercritical airfoil,with 1.25% porosity,3/4-inch cavity,M_∞=0.804

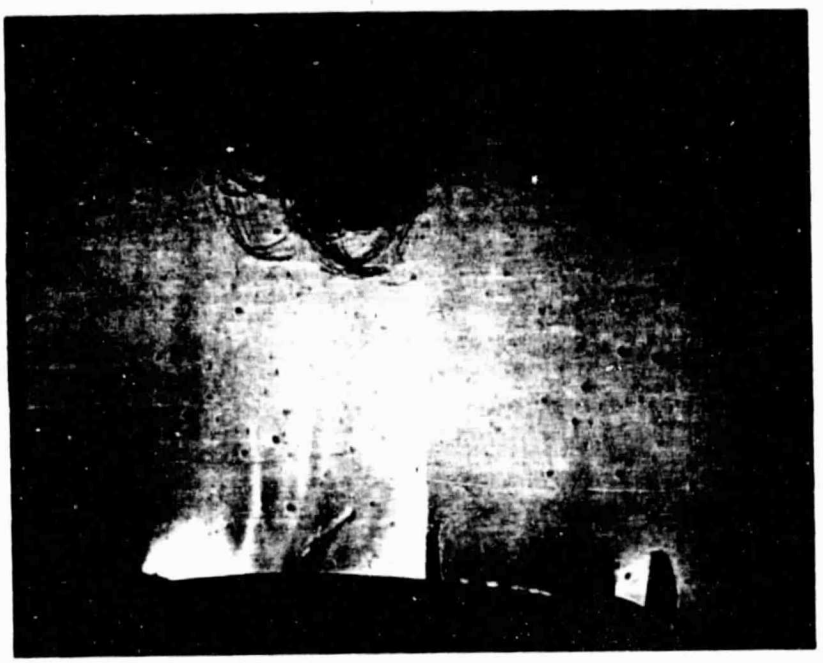

Fig.47c Schlieren photograph of flow over 14-percent-thick supercritical airfoil, with 1.25% porosity and 3/4-inch deep cavity, M_∞=0.78

a small local supersonic region as indicated in Fig. 47c. Hence, for a lower free stream Mach number of 0.78, the shock wave became weaker under the porosity effect, but did not take on the Lambda configuration. Also, its location remained approximately the same. At 0 Mach number of 0.743, the flow was entirely subsonic over the model without any shock wave.

The data of the model Mach number distribution for different free stream Mach numbers were obtained. Fig. 48a shows the distributions for M_∞ equal to .803 and .807, without and with 1.25 percent porosity, respectively. The distribution remained unaffected by the porosity from the model leading edge to 65 percent of the chord. In this region the Mach number increased over the model surface up to a maximum value of 1.23 near the mid-chord. The sudden decrease in the Mach number through the shock wave, located at approximately 78 percent of the chord, was less using the porous surface, which corresponds to a lower static pressure jump through the shock wave. Referring to Eq. (15), the ratio of the static pressures before and after the shock wave defined its strength. Since the Mach number ahead of the model is the same with and without porosity, a lower static pressure ratio indicates a weaker shock wave. The same conclusion can be drawn from Eq. (16). The static pressure difference p_2-p_1 through the shock wave was less with the porosity than without. For the same static pressure, p_1, the corresponding increase in the entropy will be less according to Eq. (17). This means that the porous surface induced a weaker shock wave over the airfoil.

The pressure distributions data for the cases of no porosity and of 1.25 percent porosity with a 3/4-inch cavity, were obtained for

free stream Mach numbers of 0.803 and 0.804, respectively. The results in terms of pressure coefficients are presented in Fig. 48b. The distribution over the model remained unaffected up to the mid-chord point; then the porous surface slightly increased the pressure coefficient between approximately the model mid-chord and the shock wave location at 78 percent of the chord. Downstream of the shock wave to the trailing edge, the porosity induced a slightly lower pressure coefficient, C_p, compensating for the gain in C_p upstream of the shock wave.

The drag data for the 14-percent-thick supercritical airfoil,[18] with 1.25 percent porosity and without porosity, at respectively M_∞ of 0.807 and 0.803, are presented in Fig. 48c. Notice that the point drag coefficient distributions decreased rapidly within the first 0.50 inch height, with slightly higher values for the 1.25 percent porosity. However, between 0.50 inch and the rest of the survey height, the local drag coefficient was lower, corresponding to a reduction in the wave drag. Although the free stream Mach number was higher with porosity than without, the integration of the point drag coefficients showed a slight net drag reduction with the porous surface.

To investigate the porosity size effect on the shock wave, pressure distribution and the wake impact pressures, the two previous cases of different porosities were compared for the same 3/4-inch cavity size. The results are discussed below.

2.5 Percent and 1.25-Percent Porosity

The data for the full porosity case corresponding to 2.5 percent and of the 1.25 percent case were compared for the same cavity size

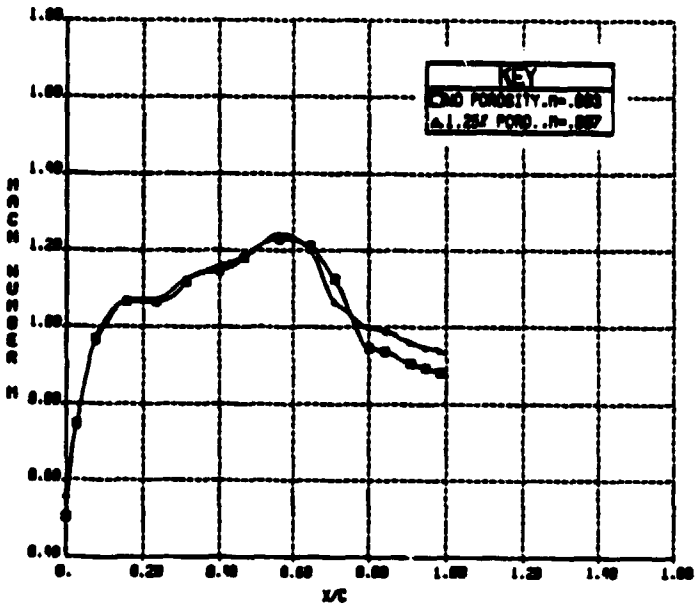

Fig.48a Mach number distributions over 14-percent-thick supercritical airfoil without and with 1.25 percent porosity,3/4-inch deep cavity

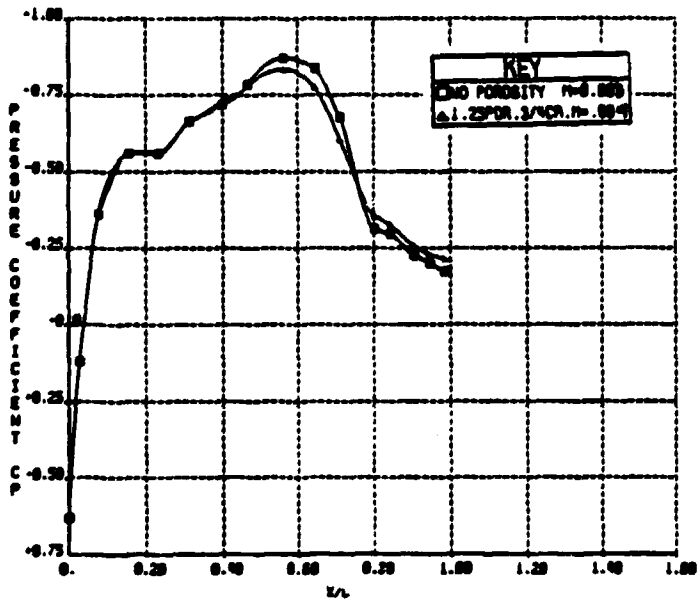

Fig.48b Pressure coefficient distributions over 14-percent thick supercritical airfoil without and with 1.25 percent porosity,3/4-inch deep cavity

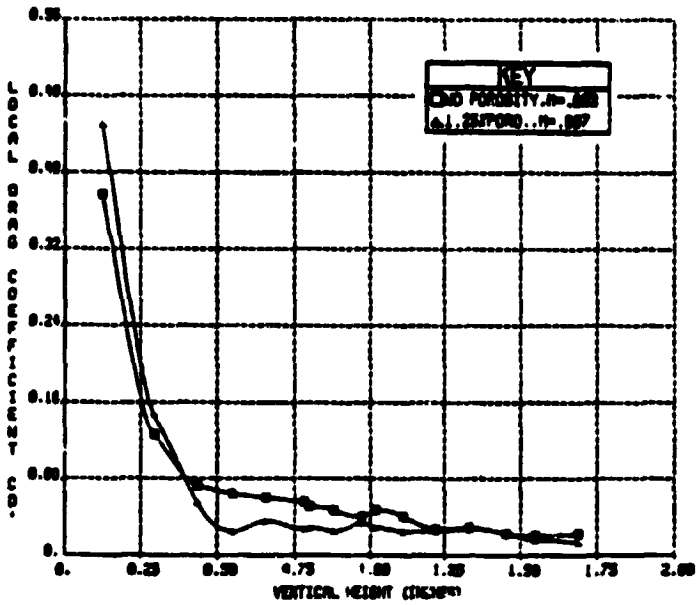

Fig.48c Local drag coefficient distributions for 14-percent-thick supercritical airfoil without and with 1.25 percent porosity, 3/4-inch deep cavity

of 3/4-inch depth. The two Mach number distributions for M_∞ of 0.806 presented in Fig. 49a, indicate that the 2.5 percent porosity has lower Mach number values over the porous surface and downstream, except for the area between 70 and 80 percent of the chord, where the 1.25 percent case was slightly lower. Consequently, the increase in porosity decreased the local maximum Mach number.

The point drag coefficient distributions from the wake survey, shown in Fig. 49b for a free stream Mach number of 0.806, indicated a lower drag with the 2.5 percent over the 1.25 percent porosity throughout the wake survey height.

The experimental results of the no porosity case, as well as the 2.5 percent and 1.25 percent porosity cases with 3/4-inch cavity, are compared for different free stream Mach numbers in the following section.

Zero Percent, 2.5 Percent and 1.25 Percent Porosity

The data concerning the Mach number distribution and drag were compared between the three porosity cases of zero percent, 2.5 percent and 1.25 percent porosity for a range of free stream Mach numbers.

Figure 50a shows the Mach number distribution obtained with M_∞ of 0.803, 0.804 and 0.806 for zero, 2.5 and 1.25 percent porosity, respectively. The porosity did not affect the distribution over the first half of the model surface. Between 50 percent and approximately 70 percent, corresponding to the porous region upstream of the shock wave, the porosity decreased the Mach number; the higher the porosity, the lower the Mach number. However, downstream of the shock wave location, between 78 percent of the chord and the model trailing edge, the porosity slightly

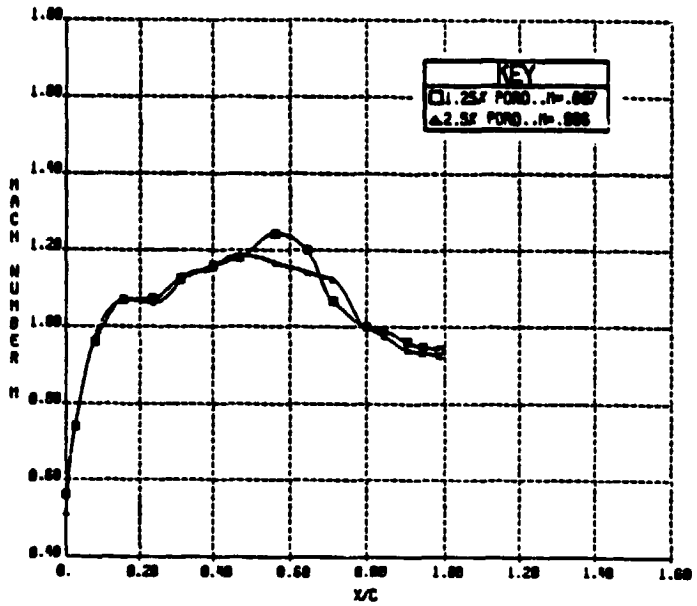

Fig.49a Mach number distributions over 14-percent-thick supercritical airfoil with 1.25 and 2.5 percent porosity,3/4-inch deep cavity

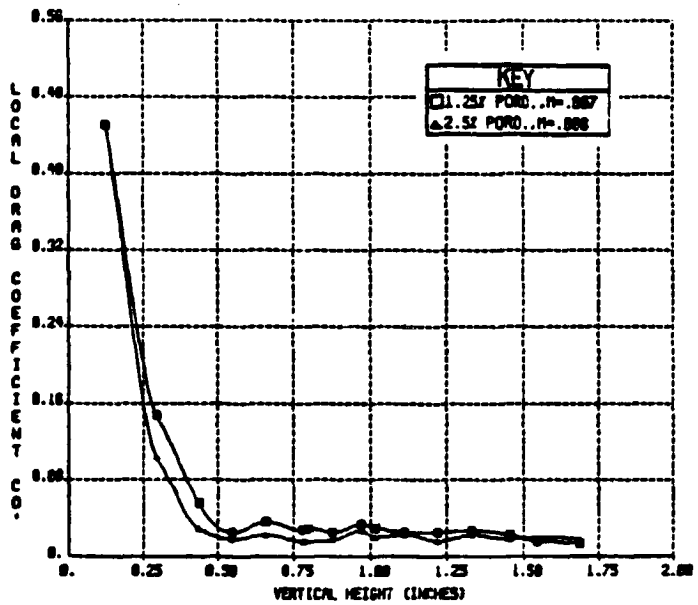

Fig.49b Local drag coefficient distributions for 14-percent-thick supercritical airfoil with 1.25 and 2.5 percent porosity,3/4-inch deep cavity

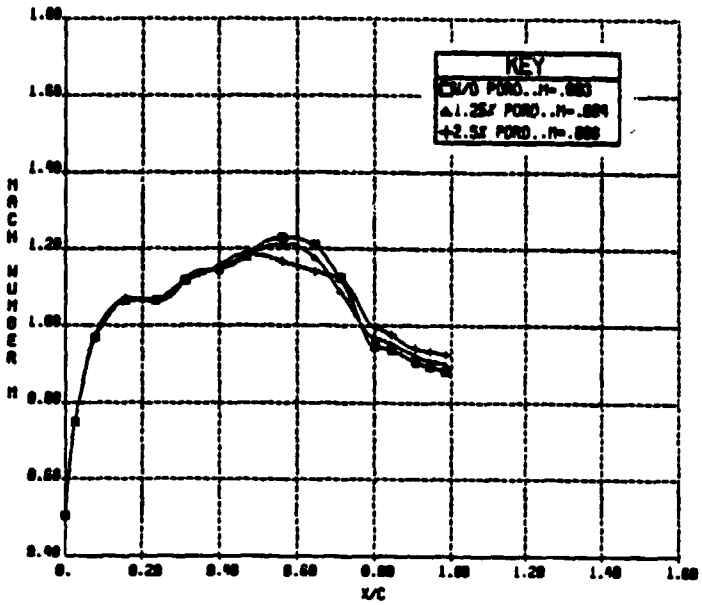

Fig.50a Mach number distributions over 14-percent-thick supercritical airfoil without,with 1.25 and 2.5 percent porosity,3/4-inch deep cavity

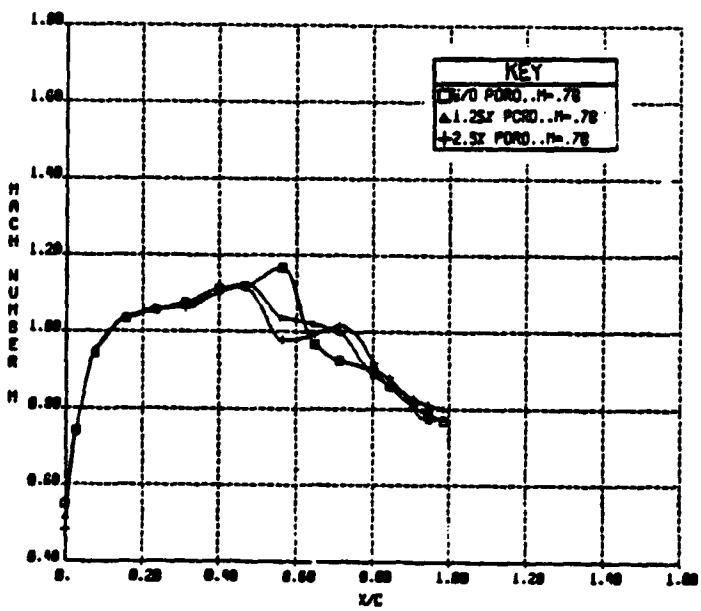

Fig.50b Mach number distributions over 14-percent-thick supercritical airfoil without,with 1.25 and 2.5 percent porosity,3/4-inch cavity

increased the Mach number; the higher the porosity, the higher the Mach number. The Mach number distributions showed virtually no effect of the porosity on the shock wave location.

The Mach number distributions for the three previous porosity cases were obtained with the same free stream Mach number of 0.78. As shown in Fig. 50b, the distribution remained unaffected up to approximately the beginning of the model porous surface which is located between 56 and 83 percent of the chord. Over the section of the porous surface upstream of the shock wave, the increase in porosity decreased the Mach number. However, over the section downstream from the shock wave, the increase in porosity increased the Mach number. Downstream from the porous surface, the distributions of the three porosity cases coincided, although the 2.5 percent case did have a slightly higher value. The shock wave moved upstream from approximately 62 percent of the chord with no porosity to 58 percent with porosity. The same observation was obtained from the corresponding Schlieren photographs. Consequently, the partial movement of the decelerated flow from the back of the shock wave to the front increased the Mach number downstream from the shock wave, and sent compression waves ahead of the shock wave, which decreased the upstream Mach number. As the porosity increased the amount of the displaced flow was larger, thereby increasing its effect on altering the values of the Mach numbers, as seen in Fig. 50b.

At $M_\infty = .74$, the flow over the model was entirely subsonic, as shown in Fig. 50c. The Mach number distribution remained unaffected by the porosity for the first 50 percent of the chord. Between approximately

50 and 70 percent of the chord corresponding to the upstream portion of the porous surface, the increase in porosity decreased the Mach number. However, over the rest of the porous area, the Mach number was slightly higher with 2.5 percent porosity, and remained unaffected with 1.25 percent porosity. Downstream from the porous surface, over the region located between 87 percent of the chord and the airfoil trailing edge, the increase in porosity increased the Mach number. Even in the absence of the shock wave, the flow over the downstream portion of the porous surface carried a higher pressure than the flow over the upstream part. Therefore, a circulation of part of the flow within the boundary layer was established between the downstream and the upstream portions of the porous surface. This circulation through the porous surface, which moved a decelerated flow from one side and injected it into the boundary layer ahead of the shock wave, induced respectively an increase and a decrease in the existing Mach numbers over these regions. By this process, the boundary layer separation was minimized, leading to an increase in the Mach number near the trailing edge, as shown in Fig. 50c.

The experimental data for the drag, obtained from the impact pressure wake surveys for the three porosity cases of 0, 1.25 and 2.5 percent, are presented in Fig. 51a. The tests were conducted with the 3/4-inch cavity and free stream Mach numbers of 0.803, 0.804 and 0.806 respectively. Within the first 0.25 inch of the boundary layer, the porosity led to a slightly higher local drag coefficient, with no difference between the 1.25 and 2.5 percent cases. However, for the rest of the wake survey height, the increase in porosity decreased the local drag coefficient.

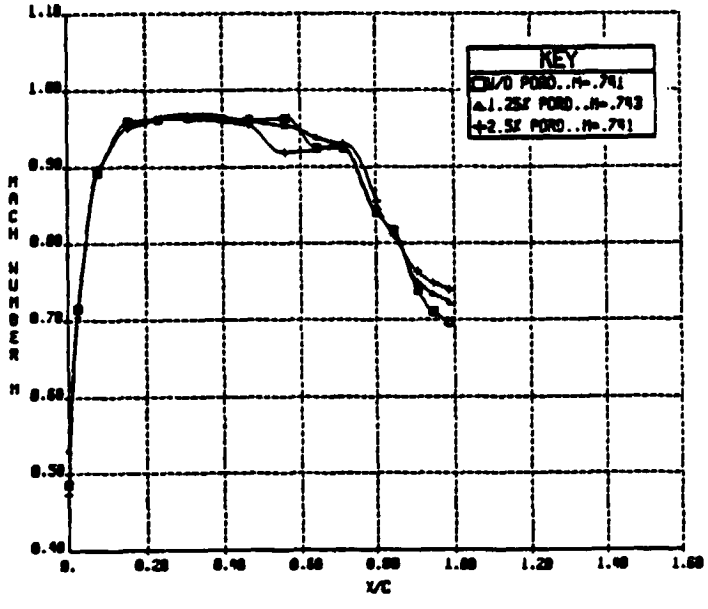

Fig.50c Mach number distributions over 14-percent-thick supercritical airfoil without,with 1.25 and 2.5 percent porosity,3/4-inch deep cavity

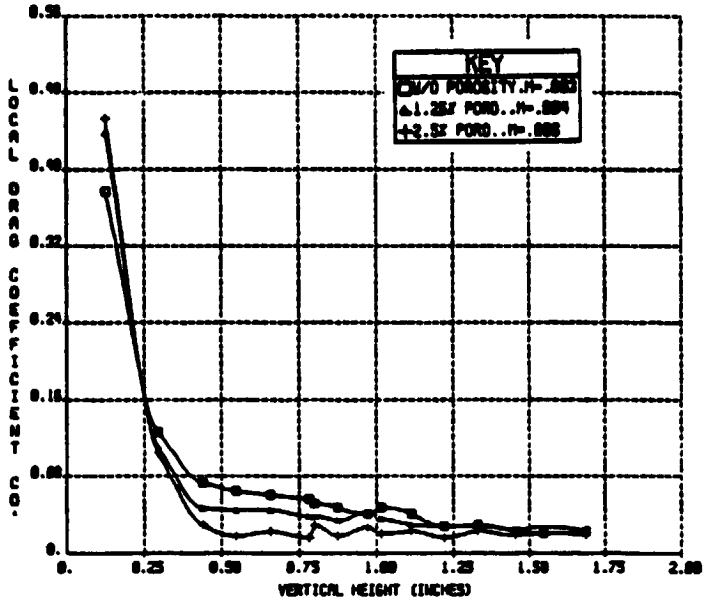

Fig.51a Local drag coefficient distributions for 14-percent-thick supercritical airfoil without, with 1.25 and 2.5 percent porosity,3/4-inch deep cavity

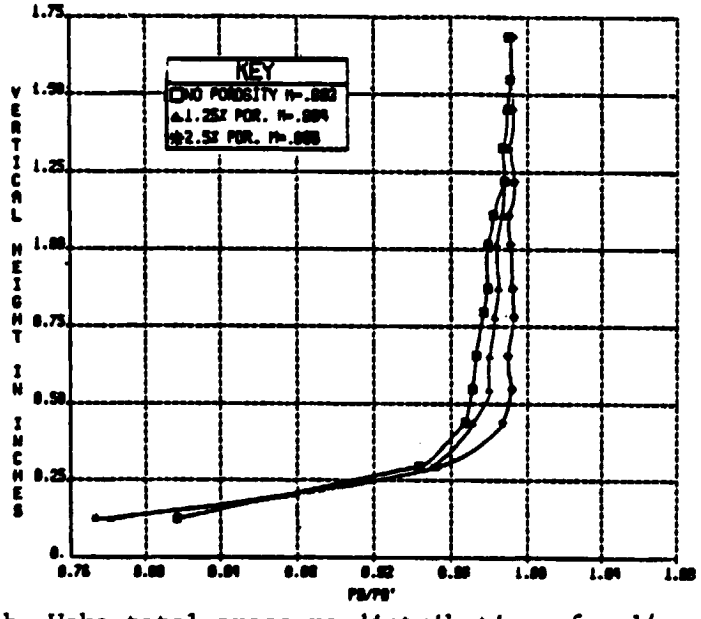

Fig.51b Wake total pressure distributions for 14-percent-thick supercritical airfoil without,with 1.25 and 2.5 percent porosity,3/4-inch deep cavity

The reduction of the wave drag was greater with the 2.5 percent porosity, eventhough the corresponding free stream Mach number was slightly higher than the 1.25 percent and the no porosity cases. The three drag distributions coincided at a height of approximately 1.65 inches. The numerical integration of the point drag coefficients throughout the wake survey height, showed a net drag reduction over the airfoil upper surface of approximately 14 percent with the 2.5 percent porosity, and 5 percent reduction for the 1.25 percent case. Corresponding total pressure ratio distributions are presented in Fig. 51b.

For a lower free stream Mach number of 0.78, Fig. 51c, the increase in porosity increased the local drag coefficient within the first 0.25 inch of the wake survey height. However, over the remaining height, the 1.25 percent porosity led to a better drag reduction than the 2.5 percent case. For this low free stream Mach number, the porosity induced a reduction in the wave drag, but a slight increase in the total drag.

A further decrease in the free stream Mach number to 0.74 established an entire subsonic flow over the model without wave drag. Within the boundary layer, the increase in porosity increased the local drag, as shown in Figs. 51d. A corresponding total pressure ratio increase is shown in Fig. 51e.

6.2.3 Effect of Model Porosity with Small Cavity

For further investigation of the passive drag control concept, the depth of the cavity beneath the porous surface was reduced and experimental data with the 2.5 percent and 1.25 percent porosity were obtained. The results will be discussed in the next two sections.

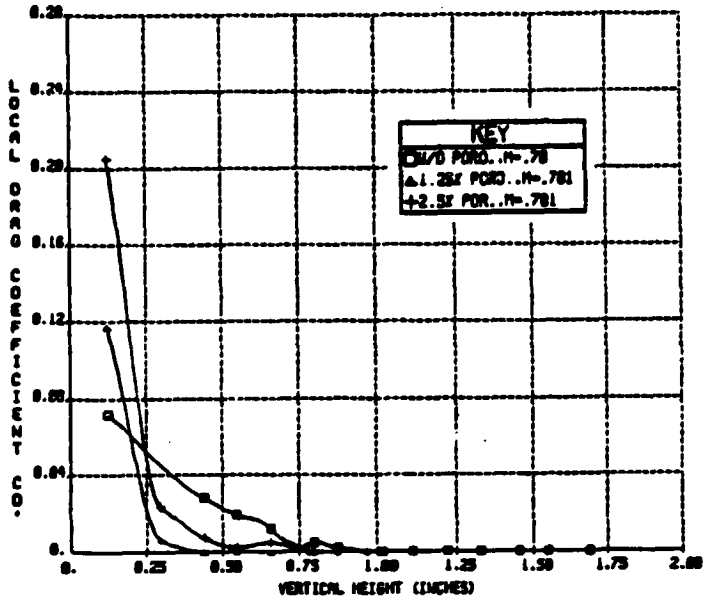

Fig.51c Local drag coefficient distributions for 14-percent-thick supercritical airfoil without, with 1.25 and 2.5 percent porosity, 3/4-inch deep cavity

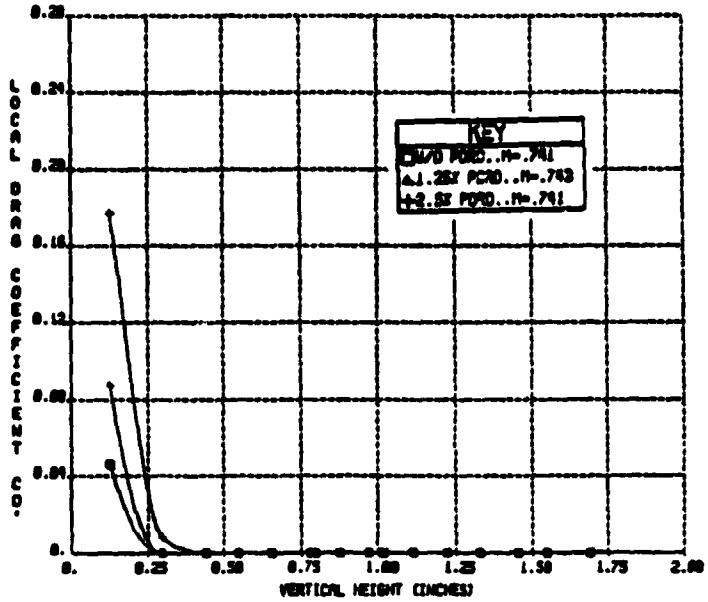

Fig.51d Local drag coefficient distributions for 14-percent-thick supercritical airfoil without,with 1.25 and 2.5 percent porosity,3/4-inch deep cavity

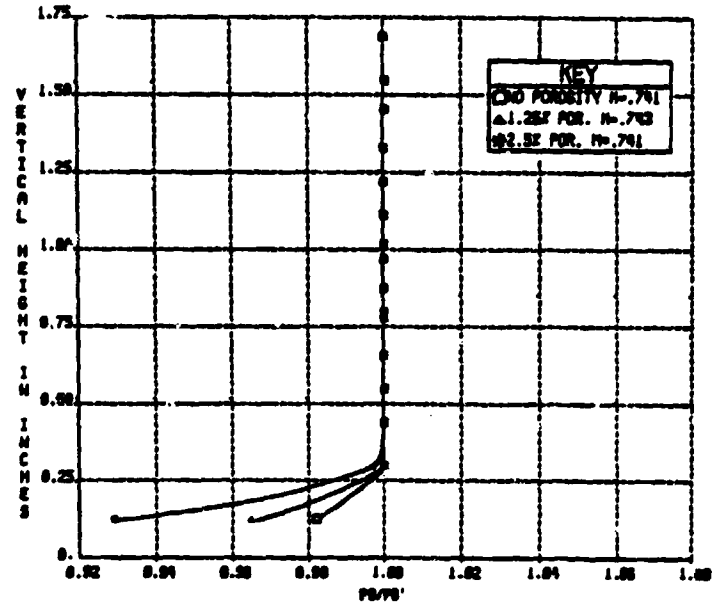

Fig.51e Wake total pressure distributions for 14-percent-thick supercritical airfoil without,with 1.25 and 2.5 percent porosity,3/4-inch deep cavity

2.5 Percent Porosity

To investigate the effect of the cavity size on the shock wave/boundary layer interaction and on the flow field, the 3/4-inch cavity depth was reduced to 1/4-inch. The rest of the cavity dimensions remained the same. The 2.5 percent porosity was selected first, because it induces a higher drag reduction at high Mach numbers.

Schlieren photographs and pressure data, as well as impact pressure wake surveys, were obtained for a range of free stream Mach numbers. The Schlieren photograph, Fig. 52a, obtained with M_∞ equal to 0.807, shows the effect of the porosity and cavity, on the shock wave shape.

The difference in pressure across the terminating shock wave caused a part of the decelerated flow downstream from it to flow upstream through the porous surface, sending compression waves into that region. Consequently, a new oblique shock wave was produced at the porous surface leading edge, which joins the terminating shock wave at a point 0.73 inch above the model surface. The effect of the porosity and the cavity on the shock wave terminating the supersonic region was visible compared to the no porosity case presented in Fig. 41b. The shock wave with porosity was normal and weak over the 0.73-inch portion close to the model surface. Under the porosity effect, the shock wave moved from 79 percent of the chord to 73 percent. Expansion waves could be seen between the 24 percent chord point and the normal terminating shock wave. Directly downstream from this normal shock wave, at a location of 78 percent of the chord from the leading edge, a very weak shock wave of approximately .58 inch

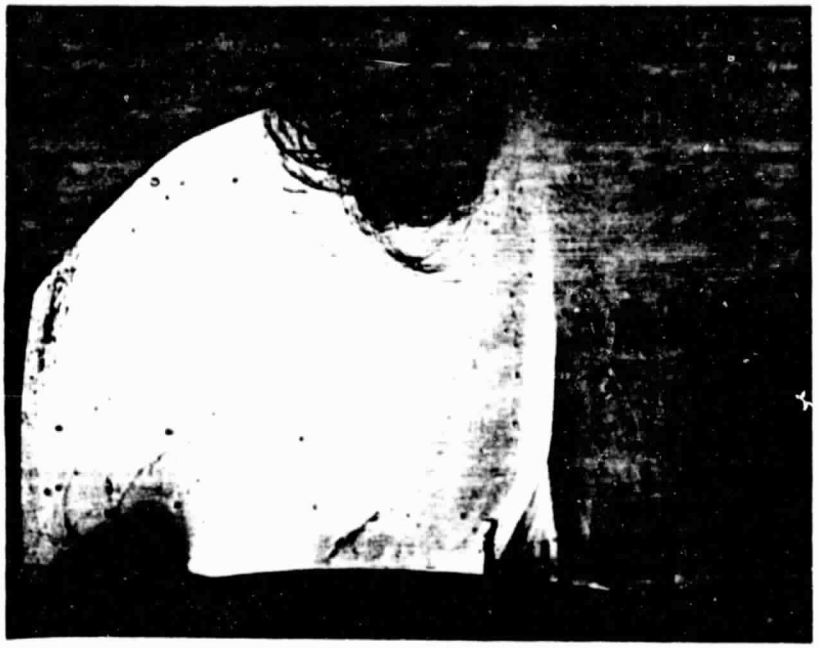

Fig.52a Schlieren photograph of flow over 14-percent-thick supercritical airfoil,with 2.5% porosity,1/4-inch deep cavity,M_∞=0.807

Fig.52b Schlieren photograph of flow over 14-percent-thick supercritical airfoil.with 2.5% porosity,1/4-inch deep cavity, M_∞=0.803

occurred over the porous surface. The Lambda shape seemed to be a characteristic of the porosity effect on the shock wave at transonic speeds.

The tests were repeated under the same conditions with M_∞ equal to 0.803, Fig. 52b. This figure shows a series of strong compression waves upstream of the terminating shock wave, produced by the circulation of the removed flow through the porous surface. The effect of those compression waves on the flow field became obvious by simply observing the perfectly normal terminating shock wave. Compared to the no porosity case, Fig. 47a, the shock wave moved slightly upstream to a location of approximately 77.6 percent of the chord instead of 79 percent, while the shock wave height of 2.42 inches remained the same. Expansion waves within the embedded supersonic region are visible in the Schlieren photograph.

With M_∞ equal to 0.78, Fig. 52c shows a weak shock wave at approximately 53 percent of the chord, whereas with no model porosity, the location was at 62 percent of the chord, Fig. 42a. The shock wave height was decreased from 1.45 inches to 0.73 inch, as was the size of the expansion waves. Consequently, the size of the supersonic region, as well as the local supersonic Mach numbers, were reduced under the porosity effect.

The Schlieren photograph obtained for a subsonic free stream Mach number of 0.74 indicates an entirely subsonic flow over the model without any shock wave. The boundary layer is not visible because the photograph was taken with a vertical knife edge. Attempts have been made (though without much success) to obtain Schlieren photographs with a horizontal knife edge to show the boundary layer behavior. The deficiency

Fig.52c Schlieren photograph of flow over 14-percent-thick supercritical airfoil,2.5% porosity, 1/4-inch cavity, M_∞=0.78

was caused mainly by the thickness of the side wall plexiglass which creates a distortion of the incident light beam through the test section. Similar results were obtained with a free stream Mach number of 0.65.

Pressure data were obtained for a range of free stream Mach numbers. Fig. 53a shows the comparison of the model Mach number distribution without and with 2.5 percent porosity for respective free stream Mach numbers of 0.806 and 0.807. From the model's leading edge to the mid-chord, the distribution remained unaffected. However, from 50 percent of the chord to the trailing edge, the Mach number was lower in the case of 2.5 percent porosity. The effect of the porosity was greater over the porous surface. The difference in the Mach number across the shock wave was smaller with the 2.5 percent porosity, corresponding to a lower jump in pressure across the shock wave. Since the Mach number, or the corresponding pressure, just downstream of the shock wave was the same for both with and without porosity, as indicated in Fig. 53a, the ratio of the static pressure, P_2/P_1, across the shock wave was lower with 2.5 percent porosity. The static pressure ratio, P_2/P_1, in Eq. (15), defined the strength of the shock wave, and thus the shock wave was weaker with the porosity. A weaker shock wave implied a lower entropy increase, as indicated by Eq. (17), or a lower total pressure loss, Eq. (18), causing a wave drag reduction. The corresponding distributions of the pressure coefficient data are presented in Fig. 53b. A similar observation is obtained with a free stream Mach number of 0.804.

For a lower M_∞ of 0.78, Fig. 53c, the effect of the porosity on the decrease of the Mach number was less severe than at a higher free

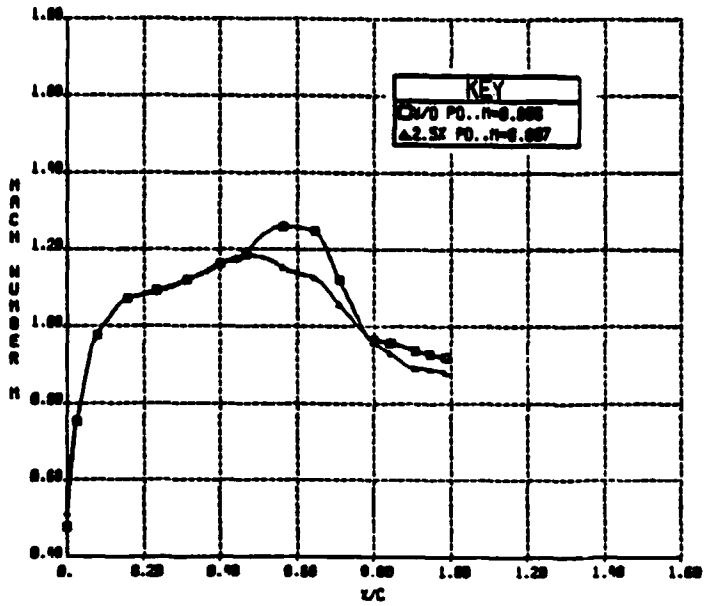

Fig.53a Mach number distributions over 14-percent-thick supercritical airfoil without and with 2.5 percent porosity ,1/4-inch deep cavity

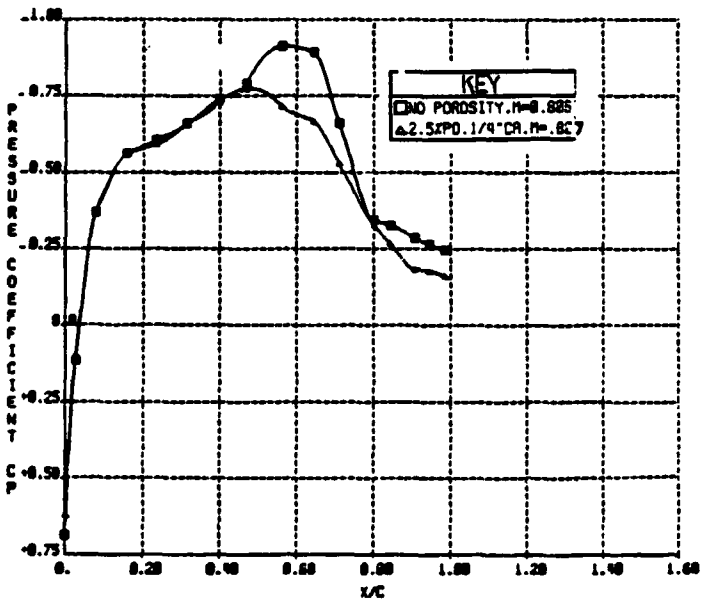

Fig.53b Pressure coefficient distributions over 14-percent-thick supercritical airfoil without and with 2.5 percent porosity,1/4-inch cavity

stream Mach number. The Mach number distribution with porosity, was slightly lower than without porosity between approximately 33 percent of the chord and the shock wave location at 53 percent and slightly higher between 53 percent and 65 percent of the chord. From 65 percent of the chord to the trailing edge, the porous case was again lower, with approximately a constant difference between the two cases.

At a free stream Mach number of 0.74, the flow was entirely subsonic, as shown in Fig. 53d, and the effect of the porosity extended to the leading edge. However, the effect was greater over the porous surface location. The two distributions with and without porosity coincided between approximately 77 percent of the chord and 90 percent. At the trailing edge the porosity induced a higher Mach number. A similar observation of the porosity effect on the Mach number distribution was obtained at a free stream Mach number of 0.65. However, the porosity in this case was slightly less effective. For a transonic Mach number of 0.807, the data on the drag obtained from the impact pressure wake survey shows a drag reduction with 2.5 percent porosity throughout the wake survey height. The local drag coefficient vanished at approximately 1.30 inches height with porosity, while with no porosity, it was still non-zero at that location. Consequently, the strength of the shock wave as well as its height were decreased by the porosity. The integration of the local drag coefficients with and without porosity indicated a net upper surface drag reduction of 35 percent.

For a free stream Mach number of 0.804, the 2.5 percent porosity and the 1/4-inch cavity reduced the drag throughout the wake survey

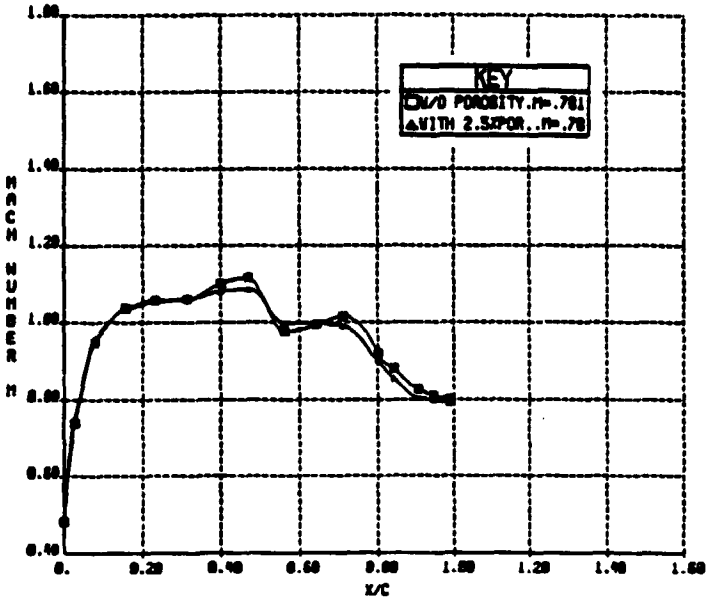

Fig.53c Mach number distributions over 14-percent-thick supercritical airfoil without and with 2.5 percent porosity,1/4-inch deep cavity

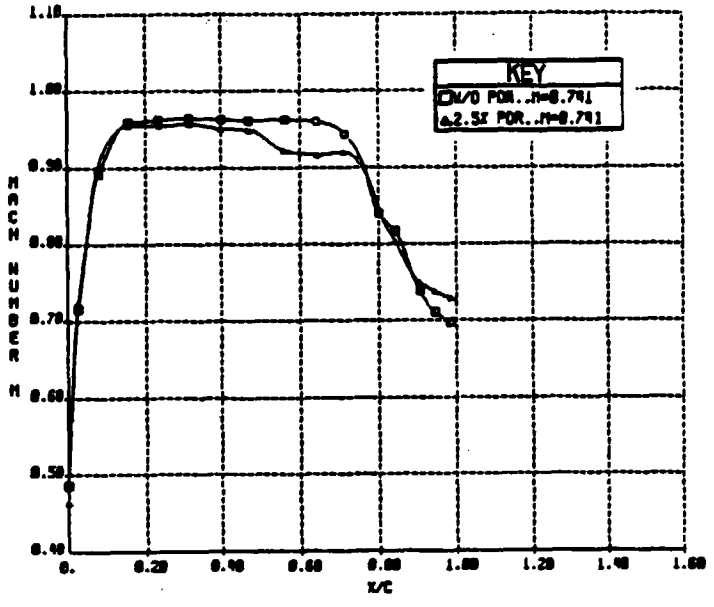

Fig.53d Mach number distributions over 14-percent-thick supercritical airfoil without and with 2.5 percent porosity,1/4-inch deep cavity

height, as shown in Fig. 54a. The drag reduction was minimum within the first 0.25 inch above the model surface, and a maximum between 0.25 inch and 0.50 inch, and then decreased within the rest of the wake survey height. The local drag coefficient with porosity vanished at 1.70 inches from the airfoil surface, a shorter distance than without porosity, corresponding to a reduction in the height of the shock wave. The summation of the local drag coefficients throughout the wake height showed a total upper surface drag reduction of approximately 38 percent. A corresponding reduction in total pressure due to the porous surface is shown in Fig. 54b.

The decrease in the free stream Mach number to 0.78 resulted in higher drag with 2.5 percent porosity than without porosity over the 0.25 inch region just above the model surface, as shown in Fig. 54c. However, for the rest of the height, the porosity reduced the drag. The point drag coefficient vanished at 1.00 inch height in the no porosity case and at 0.40 inch with the 2.5 percent case. The calculation indicates a slight increase in the total drag, although there is a local wave drag reduction.

For a lower M_∞ of 0.74, the drag was higher with the porosity up to a height of 0.30 inch from the airfoil surface, as shown in Fig. 54d. Within this height, the local drag coefficient for both with and without porosity, decreased and vanished beyond that height limit. A similar drag distribution was obtained with a free stream Mach number of 0.65.

The results obtained so far demonstrated that the concept of the passive drag reduction at transonic speeds is truly promising, but seeking a better porous surface effectiveness, further investigation and testing were done with a 1.25 percent porosity.

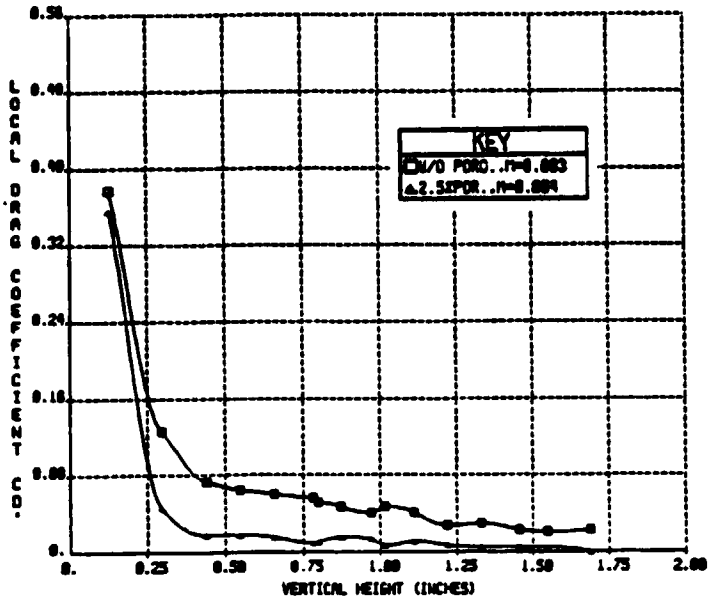

Fig.54a Local drag coefficient distributions for 14-percent-thick supercritical airfoil without and with 2.5 percent porosity,1/4-inch deep cavity

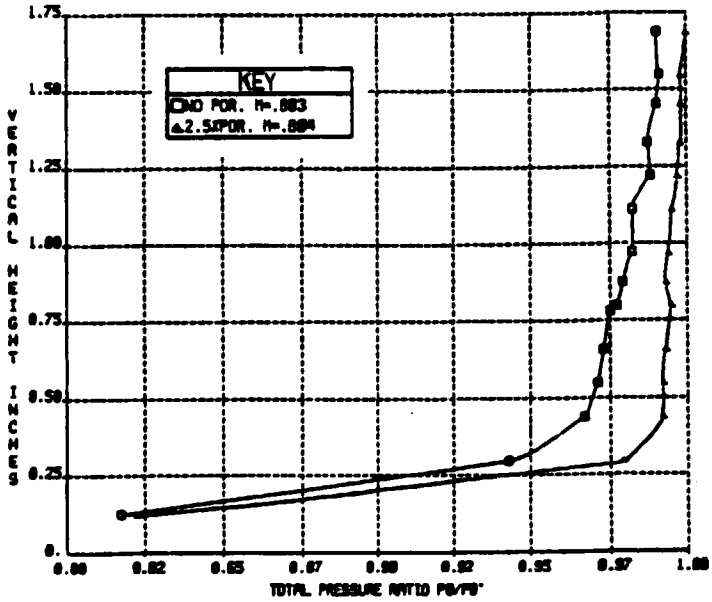

Fig.54b Wake total pressure distributions for 14-percent-thick supercritical airfoil without and with 2.5 percent porosity,1/4-inch deep cavity

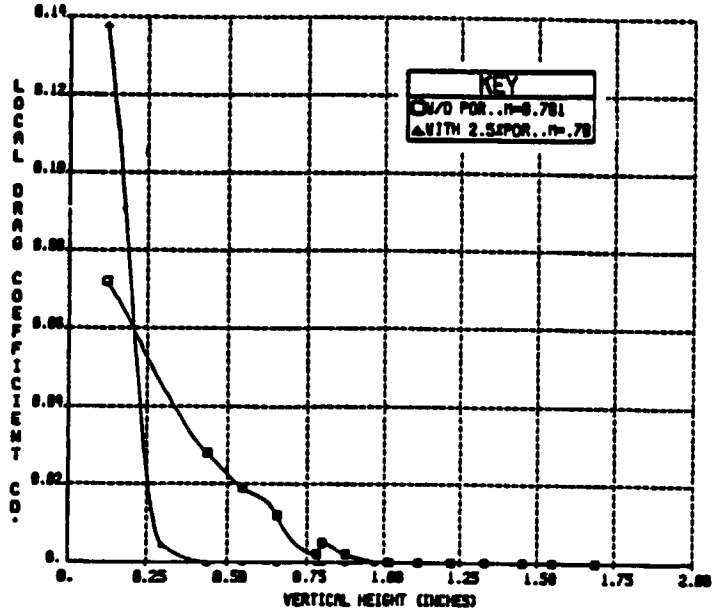

Fig.54c Local drag coefficient distributions for 14-percent-thick supercritical airfoil without and with 2.5 percent porosity,1/4-inch deep cavity

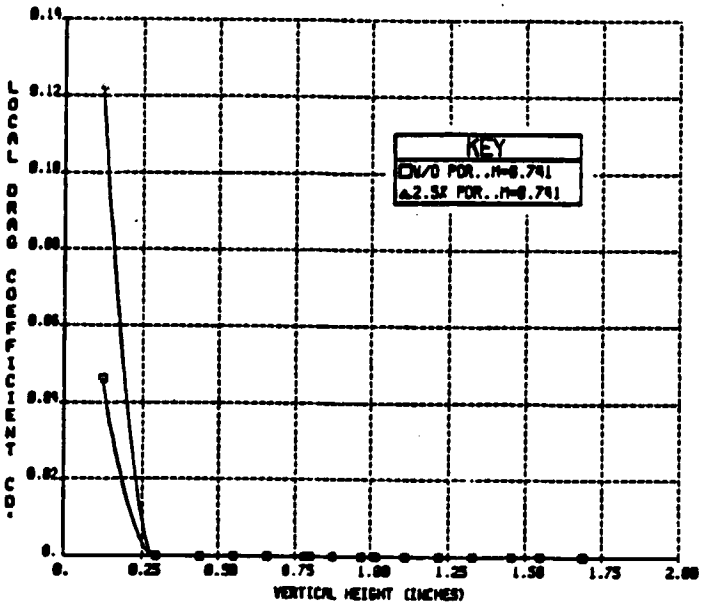

Fig.54d Local drag coefficient distributions for 14-percent-thick supercritical airfoil without and with 2.5 percent porosity,1/4-inch deep cavity

1.25 Percent Porosity

The 2.5 percent porosity was reduced to 1.25 percent by sealing every other hole of the model porous surface. The tests were conducted with the 1/4-inch cavity depth. Schlieren photographs were obtained for a range of free stream Mach numbers. The effect of the porosity on the shock wave can be seen by referring to the Schlieren photograph in Fig. 55a, obtained for a Mach number 0.804. Compression waves produced by the flow circulation through the porous surface emerge upstream of the terminating shock wave and affected its shape. Expansion curves between the airfoil leading edge and the shock wave were visible in the same figure. The shock wave height indicated the presence of a large local supersonic region over the airfoil surface. The 1.11-inch portion of the shock wave close to the model surface became normal under the compression waves effect. Consequently, the entire terminating shock wave changed from a nearly normal shape, as seen in Fig. 47a for the no porosity case, to a completely normal one. The location of the shock wave at 79 percent of the chord, as well as its height, remained unaffected by the porosity.

For a lower subsonic Mach number of 0.78, the Schlieren photograph in Fig. 55b showed a small supersonic region defined by the expansion waves and a small normal shock wave. The height of this terminating shock wave decreased from 1.45 inches to 0.97 inch by the porosity effect, and its location moved slightly forward from 63 percent of the chord to 61 percent.

The Schlieren photographs obtained for free stream Mach numbers of 0.74 and 0.65 show the flow field over the model surface without any

Fig.55a Schlieren photograph of flow over 14-percent-thick supercritical airfoil,with 1.25 % porosity,1/4-inch deep acvity, M_∞=0.804

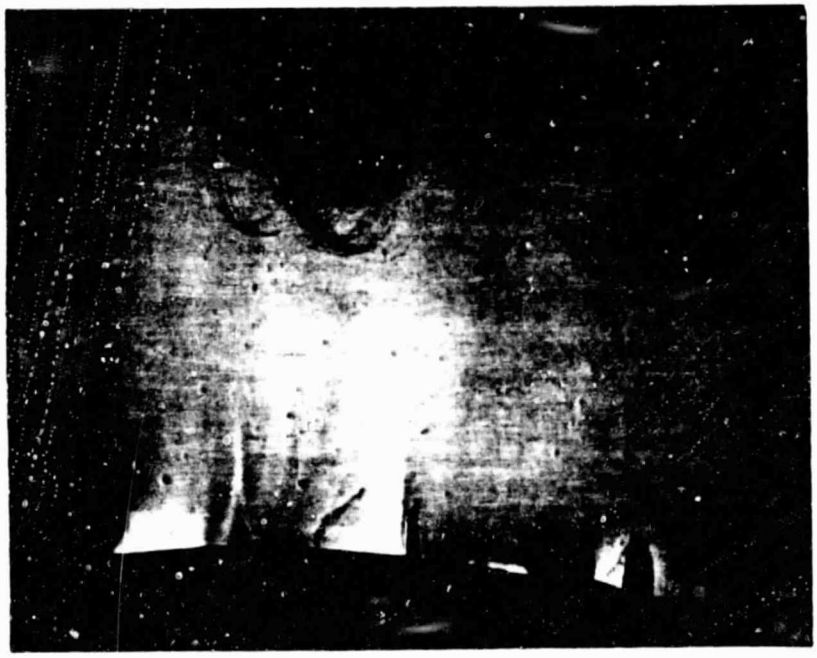

Fig.55b Schlieren photograph of flow over 14-percent-thick supercritical airfoil,with 1.25 % porosity, 1/4-inch deep cavity,M_∞=0.78

shock wave. The flow is entirely subsonic and the boundary layer behavior is the only optical information left which can predict the porosity effect. Unfortunately, this boundary layer is not visible on the Schlieren photographs taken with a vertical knife edge. Attempts have been made to obtain it with the knife edge in the horizontal position. The thickness of the side wall plexiglass produces a non-uniform contrast of the flow field picture with the horizontal knife edge. Therefore, the Schlieren photographs obtained did not provide enough information about the boundary layer. Improvements on this situation will be made in the near future.

6.2.4 Effect of Cavity Depth

To investigate the most effective of the two cavity depths, Mach number distributions as well as local drag coefficient distributions were compared for the 3/4-inch and 1/4-inch cavities with the same model porosity of 2.5 and 1.25 percent.

2.5 Percent Porosity

The Mach number distributions for M_∞ of 0.806 and 0.807 are presented in Fig. 56a. The distributions were similar upstream of the porous surface. However, from the porous surface leading edge to the model trailing edge, the 1/4-inch depth induced a lower Mach number. The difference in the Mach number was larger at the trailing edge. The corresponding drag distributions for the same free stream conditions are presented in Fig. 56b. The 1/4-inch cavity depth gave a lower drag than the 3/4-inch. As the vertical height increased, the drag decreased to a zero value at a height of 1.30 inches for the 1/4-inch case, while it was still non-zero for the 3/4-inch case.

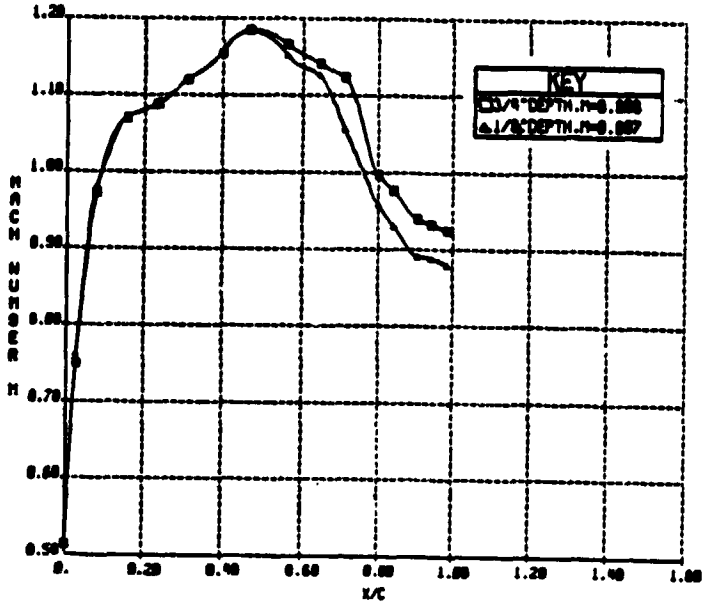

Fig.56a Mach number distributions over 14-percent-thick supercritical airfoil with 3/4-inch and 1/4-inch deep cavity,2.5 percent porosity

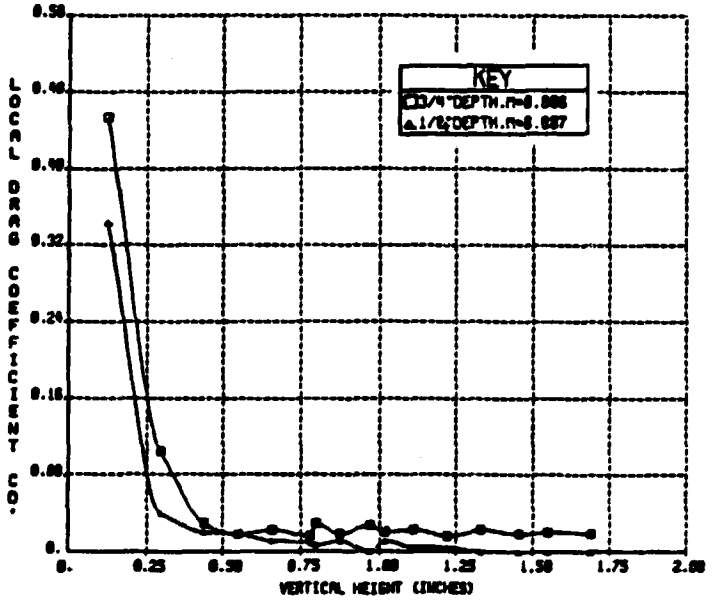

Fig.56b Local drag coefficient distributions for 14-percent-thick supercritical airfoil with 3/4-inch and 1/4-inch deep cavity,2.5 percent porosity

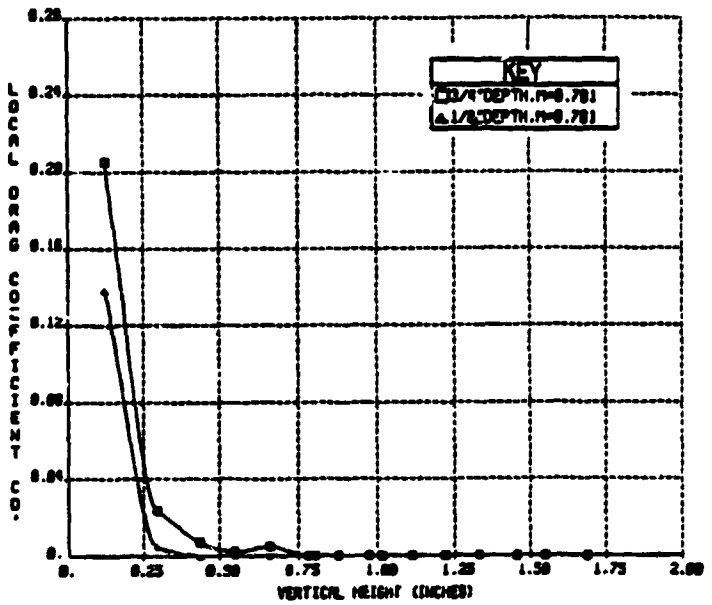

Fig.56c Local drag coefficient distributions for 14-percent-thick supercritical airfoil with 3/4-inch and 1/4-inch deep cavity,2.5 percent porosity

For a free stream Mach number of 0.78, the data of the drag presented in Fig. 56c, indicate that the 1/4-inch cavity induced a lower drag distribution than the 3/4-inch depth. The local drag coefficient of the 1/4-inch depth vanished at 0.40 inch while that of the 3/4-inch vanished at 0.75 inch.

The results showed that there was a better drag reduction with the 1/4-inch cavity depth, with little loss of lift, as compared to the 3/4-inch case. To verify this deduction, both depth cases were compared again, but this time for a different model porosity of 1.25 percent.

1.25 Percent Porosity

The comparison of the Mach number distributions obtained with M_∞ of 0.807 is presented in Fig. 57a. The distributions with the 3/4-inch and the 1/4-inch cavity were similar over the first half of the airfoil profile as well as over the last 20 percent of the chord. Between 50 and 65 percent of the chord, the 1/4-inch cavity caused a lower Mach number than the 3/4-inch. However, between 65 and 80 percent, it induced a higher Mach number. Indeed, the loss in the corresponding lift obtained between 50 and 65 percent of the chord was compensated by the gain in lift between 65 and 80 percent.

For a free stream Mach number of 0.78, Fig. 57b shows absolutely no difference between the Mach number distribution for these two cavity depths. Comparison of the drag distribution between the two cavity depth for M_∞ of 0.804 is presented in Fig. 57c. The 1/4-inch cavity produced a lower drag throughout the wake survey height. A similar result was obtained with the free stream Mach numbers of 0.78, Fig. 57d, and 0.74,

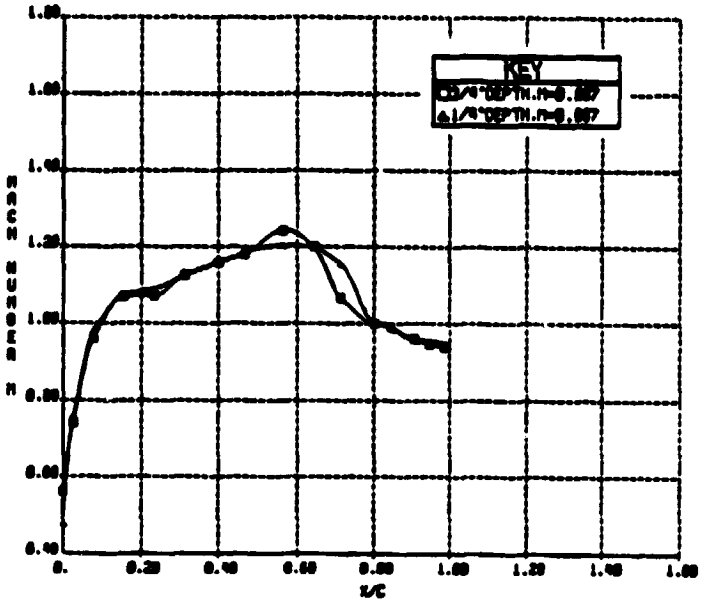

Fig.57a Mach number distributions for 14-percent-thick supercritical airfoil with 3/4-inch and 1/4-inch deep cavity,1.25 percent porosity

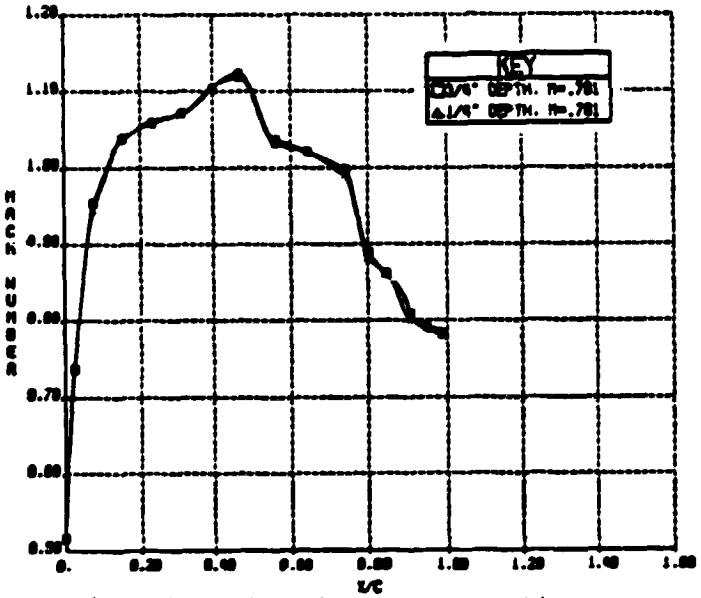

Fig.57b Mach number distributions over 14-percent-thick supercritical airfoil with 3/4-inch and 1/4-inch deep cavity,1.25 percent porosity

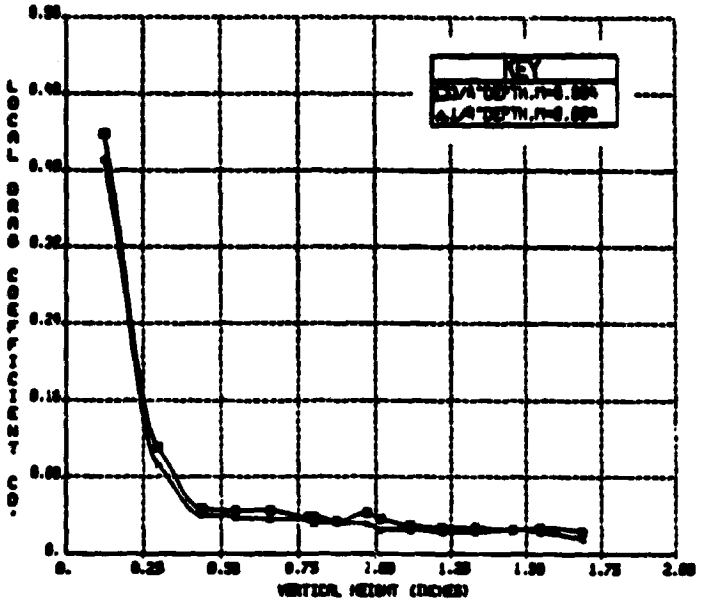

Fig.57c Local drag coefficient distributions for 14-percent-thick supercritical airfoil with 3/4-inch and 1/4-inch deep cavity,1.25 % porosity

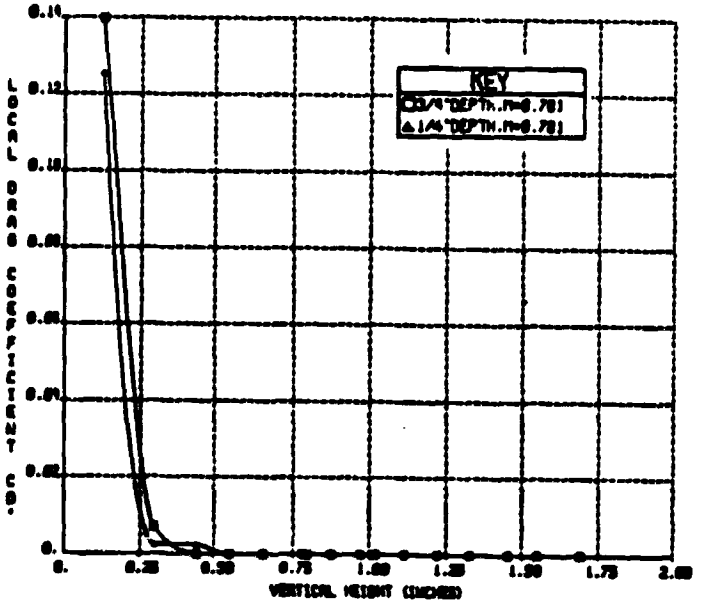

Fig.57d Local drag coefficient distributions for 14-percent supercritical airfoil with 3/4-inch and 1/4-inch deep cavity,1.25% porosity

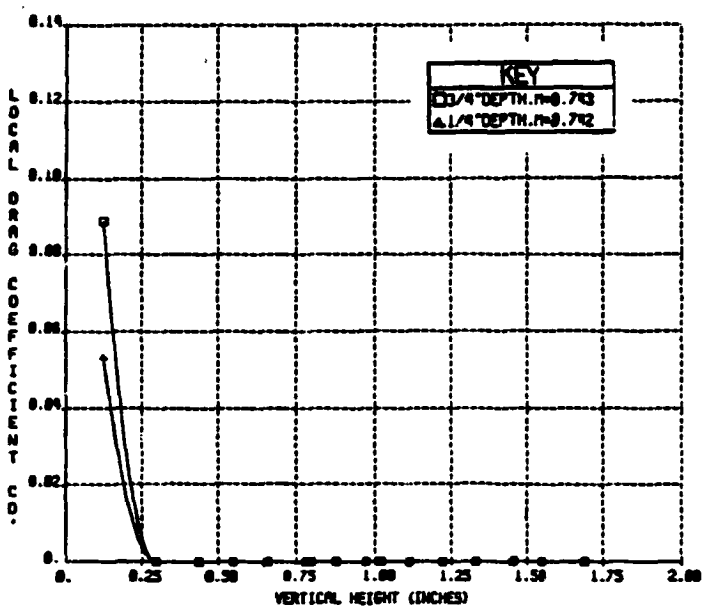

Fig.57e Local drag coefficient distributions for 14-percent-thick supercritical airfoil with 3/4-inch and 1/4-inch deep cavity, 1.25 percent porosity

Fig. 57e. With the 1.25 percent porosity, the 1/4-inch deep cavity produced a lower drag with no loss in lift as compared to the 3/4-inch case.

6.2.5 Effect of Humidity

To investigate the humidity effect on the flow field, the dryer located at the entrance of the Transonic Wind Tunnel, as shown in Fig. 1, was reactivated to bring the relative humidity from around 50 percent down to around 23 percent. Schlieren photographs, pressure distributions and impact pressure wake survey obtained without model porosity, before and after the dryer reactivation were compared.

To best simulate free flight conditions in the Transonic Wind Tunnel, the humidity was brought to a lower range by reactivating the dryer for a period of approximately 48 hours. The Schlieren photograph in Fig. 58a, obtained for a free stream Mach number of 0.806, shows a displaced shock wave from 79 percent to 76 percent of the chord due to the decrease in the relative humidity. However, the shock wave height and shape remained unaffected.

The Mach number distributions before and after dryer reactivation are compared in Fig. 58b, with no model porosity and with a free stream Mach number of 0.806. The decrease in humidity increased the local maximum Mach number located at approximately 55 percent of the chord, and produced a slightly lower Mach number distribution between 65 percent of the chord and the airfoil trailing edge. However, over the first half of the model chord, the distribution was unaffected.

The corresponding drag distributions obtained under the same conditions are presented in Fig. 58c. The increase in humidity decreased

Fig.58a Schlieren photograph of flow over 14-percent-thick supercritical airfoil, without porosity, after dryer reactivation, $M_\infty = 0.806$

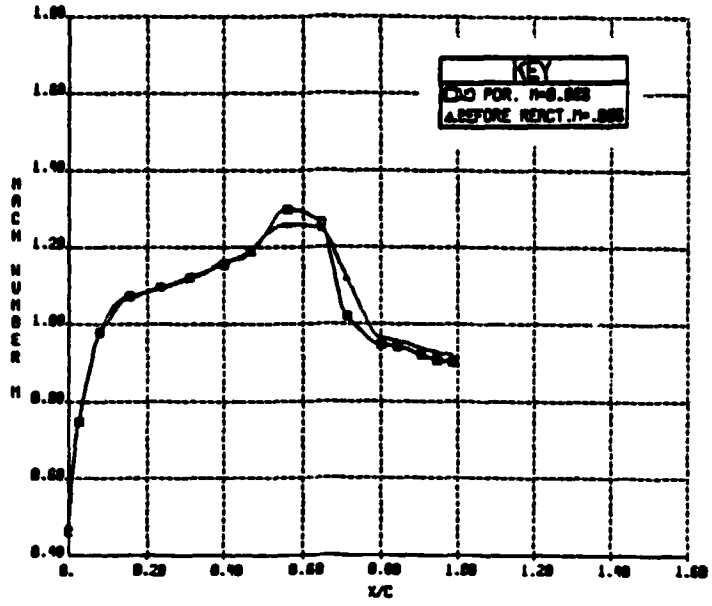

Fig.58b Mach number distributions over 14-percent-thick supercritical airfoil before and after dryer reactivation, without porosity, M_∞=0.806

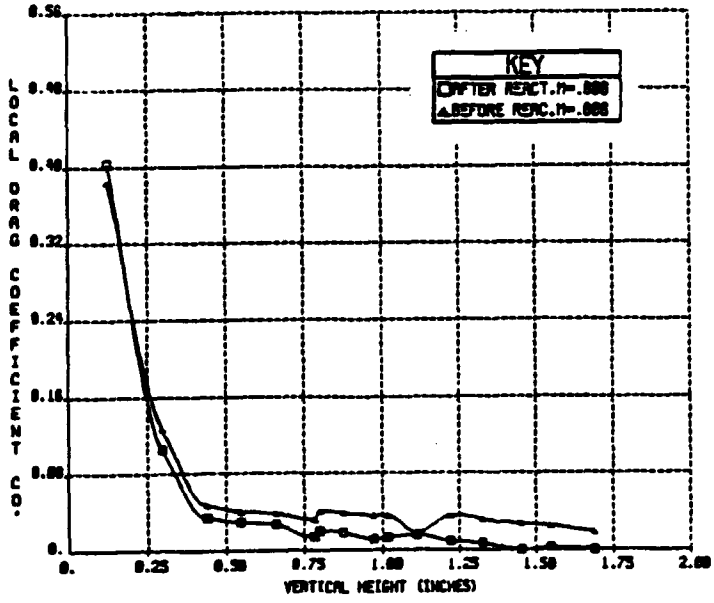

Fig.58c Local drag coefficient distributions for 14-percent-thick supercritical airfoil before and after dryer reactivation, without porosity, M_∞=0.806

the drag throughout the height of the wake survey and brought it to zero at a smaller height of 1.45 inches. The difference in the drag between the two distributions before and after the dryer reactivation was negligible within the first 0.25 inch, and thereafter increased with increasing height.

To investigate the humidity effect on the drag reduction, data were obtained after the dryer reactivation, with 2.5 percent porosity and 1/4-inch deep cavity as well as with no porosity. The choice of the 2.5 percent porosity and 1/4-inch cavity sizes for a comparison with the no porosity case was based on the previous test results.

A Schlieren photograph obtained with the 2.5 percent porosity and a free stream Mach number 0.806 is shown in Fig. 59a. Compared to the no porosity case, Fig. 58a, the terminating shock wave was once again affected by the porosity in its shape as well as in its height. New compression waves produced by the flow circulation through the porous surface as discussed previously, transformed the existing shock wave into a normal one. A decrease in the shock wave height from 2.28 inches to 2.13 inches was also produced. However, the shock wave location at 76 percent of the chord remained unaffected by the porosity. The compression waves departing from the model porous surface reached the terminating shock wave within a height of 0.97 inch.

The Mach number distribution under the same conditions as above is presented in Fig. 59b. The distribution remained unaffected by the 2.5 percent porosity from the model leading edge to approximately half of the chord. Between 50 and 70 percent of the chord, the porosity de-

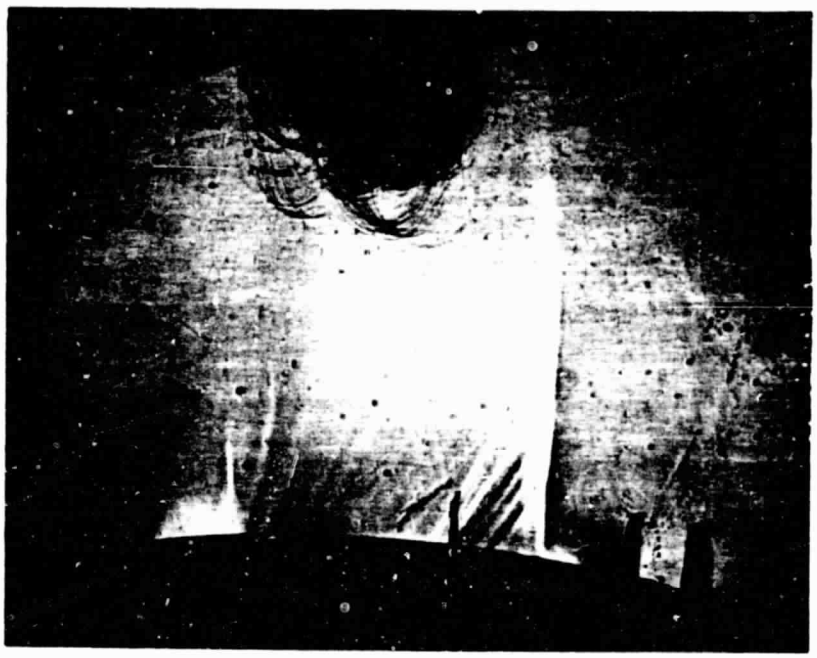

Fig.59a Schlieren photograph of flow over 14-percent-thick supercritical airfoil, with 2.5 % porosity and 1/4-inch cavity, after dryer reactivation, M_∞=0.806

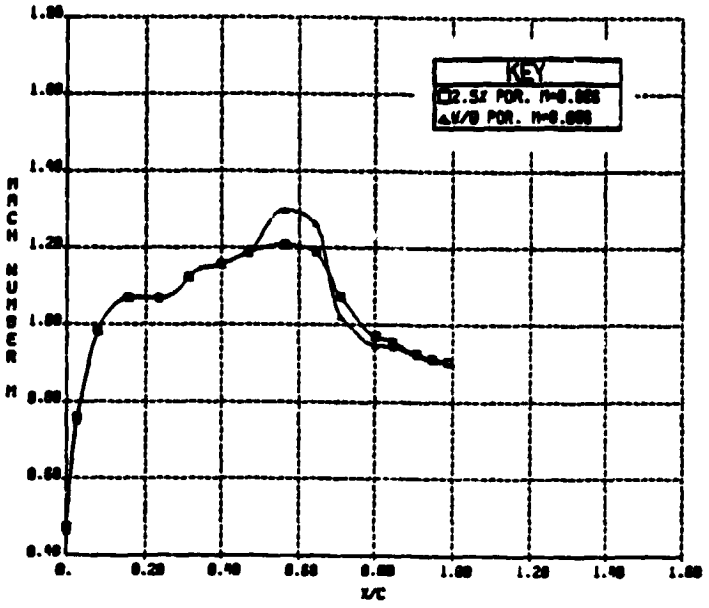

Fig.59b Mach number distributions over 14-percent-thick supercritical airfoil without and with 2.5 percent porosity,1/4-inch cavity after dryer reactivation

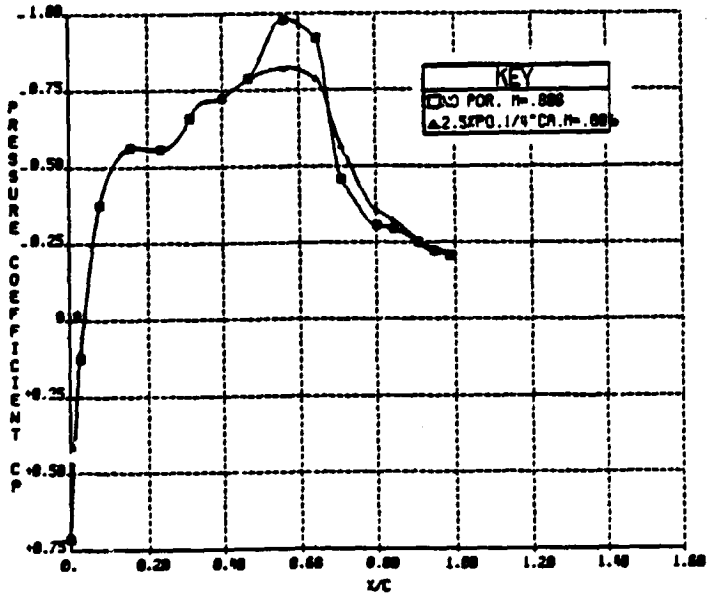

Fig.59c Pressure coefficient distributions over 14-percent-thick supercritical airfoil without and with 2.5 % porosity,1/4-inch cavity,after dryer reactivation

creased the Mach number, while between 70 and 90 percent, it increased it. The two distributions of with and without porosity coincided at the airfoil trailing edge. The porosity decreased the Mach number over the portion of the porous surface upstream of the shock wave and increased it downstream. The corresponding pressure coefficient distributions are presented in Fig. 59c.

The drag distribution with the previous test conditions, is presented in Fig. 59d. The 2.5 percent porosity caused a lower drag distribution throughout the survey height, with approximately zero drag beyond 0.50 inch height. The maximum drag reduction occurred between the heights of approximately 0.25 and 0.75 inch. This reduction was mainly a wave drag reduction, which occurred within the compression waves influence region. The summation of the local drag coefficients showed a net upper surface drag reduction of approximately 18 percent. The corresponding total pressure distribution is shown in Fig. 59e.

6.2.6 Effect of Test Section Top Wall Porosity

The preceding tests were conducted with the test section porous top wall fully closed. To investigate the effect of this top wall porosity on the flow field and the drag reduction, half of the full porosity was selected. The full porosity, based on the total area of the top wall, was approximately 10 percent.

Schlieren photograph, pressure distributions and impact pressure wake surveys were obtained without and with 2.5% porosity and 1/4-inch cavity for a free stream Mach number 0.806. The Schlieren photograph obtained with no model porosity is presented in Fig. 60a. A strong shock wave located at 76 percent of the chord, with a 2.23-inch height terminated

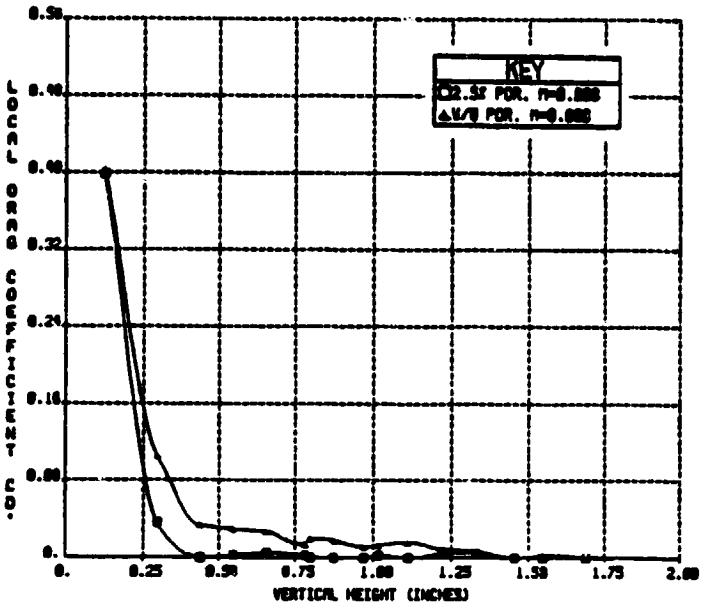

Fig.59d Local drag coefficient distributions for 14-percent-thick supercritical airfoil without and with 2.5 percent porosity,1/4 inch deep cavity,after dryer reactivation

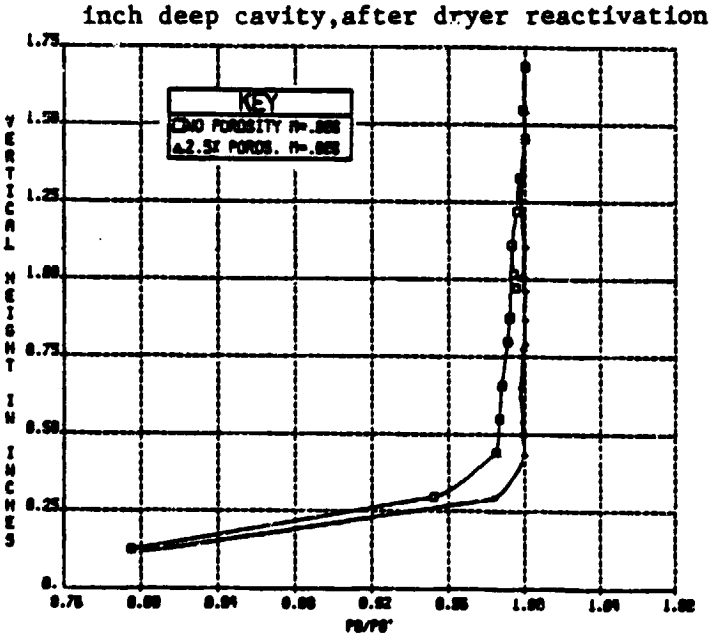

Fig.59e Wake total pressure distributions for 14-percent-thick supercritical airfoil without and with 2.5 % porosity,1/4-inch deep cavity after dryer reactivation

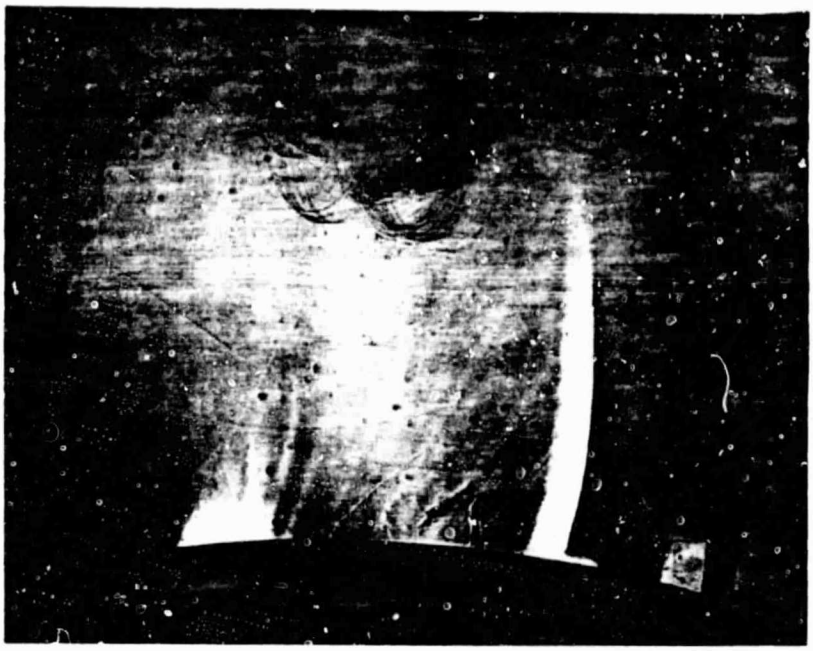

Fig.60a Schlieren photograph of flow over 14-percent-thick supercritical airfoil,without porosity,1/2 top wall porosity,M_∞=0.806

Fig.60b Schlieren photograph of flow over 14-percent-thick supercritical airfoil,2.5 %porosity and 1/4-inch cavity, 1/2 top wall porosity,M_∞=0.806

a large supersonic zone within which expansion waves could be seen. The effect of the porosity is evident in Fig. 60b, where the shock wave has been changed into a normal one under the influence of the compression waves. The shock wave location was not affected by either the model or the top wall porosities. However, its height decreased to 2 inches due to the model porosity effect.

With the same half top wall porosity and M_∞ of .806, the Mach number distributions were obtained with and without model porosity. The trends shown in Fig. 60c are similar to those in the previous Mach number figures. The distribution remained unaffected by the model porosity over the first half of the airfoil surface. Between 50 and 70 percent of the chord, the model porosity decreased the Mach number while between 70 percent and the airfoil trailing edge, it slightly increased it. The decrease in the Mach number was produced over the portion of the porous surface upstream of the shock wave, while the increase was downstream. The corresponding pressure coefficient distribution is presented in Fig. 60d.

The drag distributions with 2.5 percent and without model porosity for a free stream Mach number of .806 are presented in Fig. 60e. The porosity induced a drag reduction throughout the wake survey height. The reduction was again maximum between approximately 0.25 and 0.75 inch, the region of the compression waves' influence. The estimated net upper surface drag reduction was 8 percent.

6.2.7 Analysis of Shock Wave Losses

To confirm the experimental wave drag reduction results, a

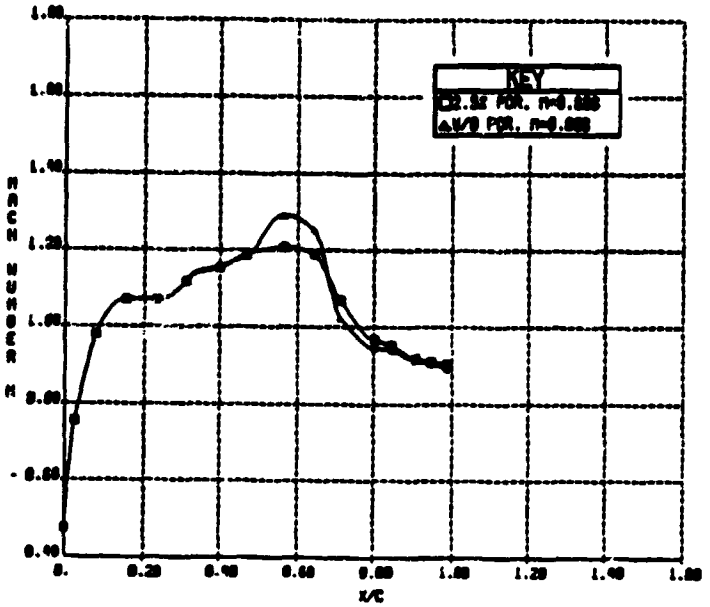

Fig.60c Mach number distributions over 14-percent-thick supercritical airfoil without and with 2.5 % porosity,1/4-inch cavity,1/2 top wall porosity, M_∞=0.806

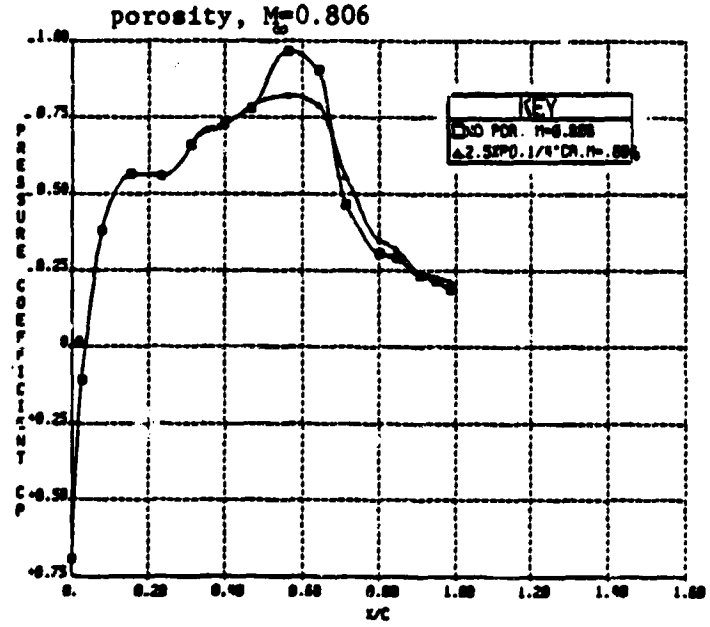

Fig.60d Pressure coefficient distributions over 14-percent-thick supercritical airfoil without and with 2.5 % porosity,1/4-inch cavity, 1/2 top wall porosity , M_∞=0.806

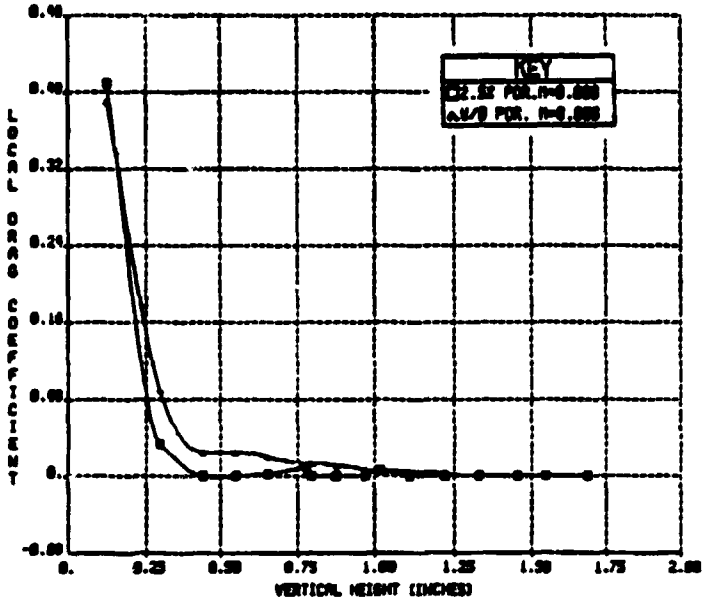

Fig.60e Local drag coefficient distributions for 14-percent-thick supercritical airfoil without and with 2.5 percent porosity, 1/4-inch deep cavity, 1/2 top wall porosity, M_∞=0.806

brief theoretical analysis was applied to the flow across the shock wave over the model surface with and without porosity. By assuming, in the case of no porosity, that the terminating shock wave has a normal shape, the normal shock wave relations indicate the following results

$$\frac{P_{o2}}{P_{o1}} = \left[\frac{\gamma+1}{2\gamma M_1^2-(\gamma-1)}\right]^{\frac{1}{\gamma-1}} \left[\frac{(\gamma+1)M_1^2}{(\gamma-1)M_1^2+2}\right]^{\frac{\gamma}{\gamma-1}}, \quad (19)$$

$$\frac{S_2-S_1}{R} = Pn\,\frac{P_{o1}}{P_{o2}}, \text{ and} \quad (18)$$

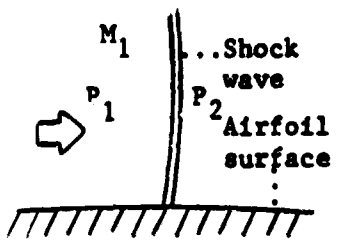

$$\frac{P_2}{P_1} = 1 + \frac{2\gamma}{\gamma+1}(M_1^2-1) \quad (15)$$

where P_{o1} and P_{o2} are the total pressures ahead and behind the shock wave; P_1 and P_2 the static pressures and S_1 and S_2 the entropy per unit mass.

With the porous surface model at transonic Mach number, the experiments showed the following Lambda Shock Wave System consisting of an oblique and a normal shock wave.

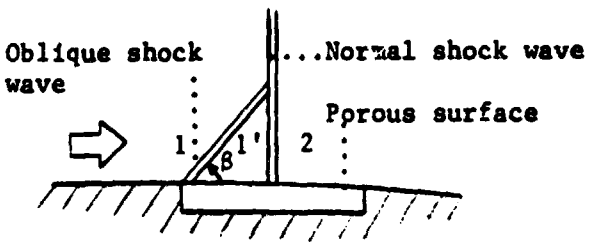

Using the oblique shock wave relations between 1 and 1', and the normal relations between 1' and 2, we obtain

$$\frac{P_{o1'}}{P_{o1}} = \left[\frac{\gamma+1}{2\gamma M_1^2\sin^2\beta-(\gamma-1)}\right]^{\frac{1}{\gamma-1}} \left[\frac{(\gamma+1)M_1^2\sin^2\beta}{(\gamma-1)M_1^2\sin^2\beta+2}\right]^{\frac{\gamma}{\gamma-1}} \text{ and} \quad (24)$$

$$\frac{P_{o2}}{P_{o1'}} = \left[\frac{\gamma+1}{2\gamma M_1'^2-(\gamma-1)}\right]^{\frac{1}{\gamma-1}} \left[\frac{(\gamma+1)M_1'^2}{(\gamma-1)M_1'^2+2}\right]^{\frac{\gamma}{\gamma-1}}$$

where M_1' is given by Eq. (20.

$$M_1'^2\sin^2(\beta-\theta) = \frac{[1 + \frac{\gamma-1}{2} M_1^2\sin^2\beta]}{[\gamma M_1^2\sin^2\beta - \frac{\gamma-1}{2}]} \qquad (20)$$

If we assume the flow deflection angle θ after the shock wave to be negligible compared to the shock wave angle β, we obtain

$$M_{1'} = \frac{1}{\sin\beta}\left[\frac{2+(\gamma-1)M_1^2\sin^2\beta}{2\gamma M_1^2\sin^2\beta-(\gamma-1)}\right]^{\frac{1}{2}}$$

The entropy increase is given by the following equations

$$\frac{S_{1'}-S_1}{R} = \ln\frac{P_{o1}}{P_{o1'}} \quad \text{and}$$

$$\frac{S_2-S_{1'}}{R} = \ln\frac{P_{o1'}}{P_{o2}}$$

Consequently, the entropy increase between 1 and 2 is given by

$$\frac{S_2-S_1}{R} = \ln\frac{P_{o1}}{P_{o2}}$$

The static pressure increase is given by

$$\frac{P_{1'}}{P_1} = 1 + \frac{2\gamma}{\gamma+1}(M_1^2\sin^2\beta-1) \quad \text{and} \qquad (22)$$

$$\frac{P_2}{P_{1'}} = 1 + \frac{2\gamma}{\gamma+1}(M_{1'}^2-1) \qquad (15)$$

This yields the pressure increase across the shock wave system

$$\frac{P_2}{P_1} = [1 + \frac{2\gamma}{\gamma+1}(M_1'^2-1)][1 + \frac{2\gamma}{\gamma+1}(M_1^2 \sin^2\beta-1)]$$

By using the experimental value of the local Mach number M_1 ahead of the shock wave, for the cases of with and without porosity, and by measuring β from the Schlieren photographs, the above equations give the following results:

	No Porosity	With Porosity
M_∞	.806	.806
M_1	1.26	1.26
M_1'	1.26	1.06
P_{02}/P_{01}	.9857	.9989
$S_2-S_{1/R}$	.014	.0011
P_2/P_1	1.686	1.402

It follows from these results that the total pressure loss, the entropy increase and the static pressure increase are all less with porosity than without. Indeed, the theory confirms the experimental wave drag reduction results. The flow circulation through the porous surface and the cavity had provided a new oblique shock wave which lowered the local Mach number just upstream of the shock wave terminating the embedded supersonic region, thus weakening the strength of the shock. Figs. 61a and b with and without porosity respectively show a good agreement between the theoretical and experimental total pressure loss results.

The 1/4-inch deep cavity was expected to provide larger pressure difference between the flow upstream of the terminating shock wave and the flow within the cavity than the 3/4-inch cavity. This was confirmed by the cavity pressure measurements. Therefore, the smaller cavity produces

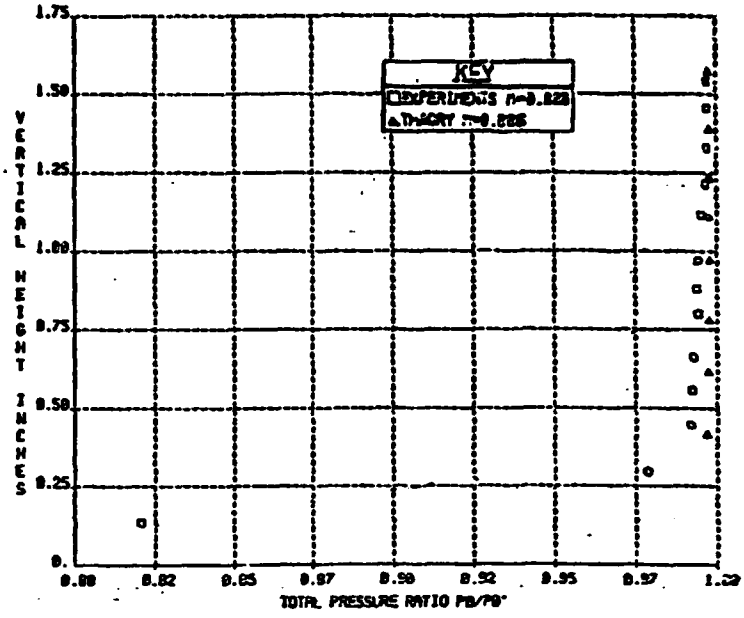

Fig.61a Experimental and theoretical pressure losses across shock wave, with porosity, M_∞=0.806

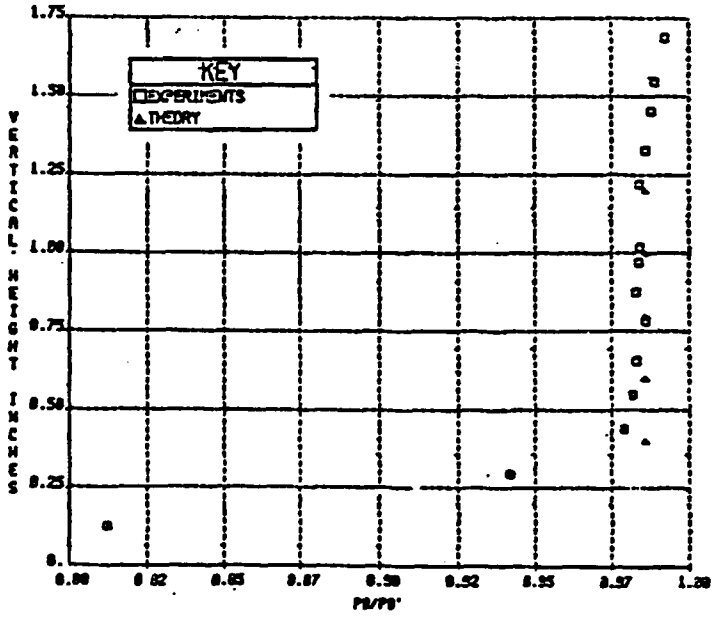

Fig.61b Experimental and theoretical pressure losses across shock wave without porosity, M_∞=0.80

a stronger oblique shock wave and consequently, weakens the normal shock wave strength more than the larger cavity. Since the main total pressure losses are produced across the normal shock wave rather than across the oblique shock, the weaker terminating shock wave associated with the 1/4-inch cavity produces larger drag reduction, as shown in Fig. 56b.

Although there is an undesirable compression effect on the lift due to the oblique shock wave upstream of the terminating shock wave, the porous surface has, on the other hand, the desirable lift increase effect over the region downstream from the shock, caused by the decelerated flow circulation as shown in Fig. 59b. This flow mechanism which produces a lift decrease upstream of the shock wave and an increase downstream from it tends to keep the net lift unchanged with and without porosity.

For smaller model porosity of 1.25 percent, compression waves are produced instead of an oblique shock wave, lowering the local Mach number just ahead of the terminating shock, but not as low as with the oblique shock in the 2.5 percent porosity case. Therefore, the drag reduction with the 1.25 percent model porosity is less, as shown in Fig. 51a.

The data with the 2.5 percent porosity and 1/4-inch cavity showed an appreciable drag reduction associated with the Lambda Shock Wave System and with the decelerated flow circulation with or without a negligible loss in lift. The section drag distribution with and without porosity, presented in Fig. 40b, shows the porosity effect at transonic Mach numbers, causing either a drag reduction or a speed increase.

PART 7

CONCLUSION

A 3-inch by 15.4-inch Transonic Wind Tunnel was designed, constructed,and calibrated to operate over a Mach number range of 0.5 to 0.95. Modifications of the test section were made to account for the boundary layer growth along the tunnel walls.The flow Mach number in the test section was controlled by the adjustable wedges located on the top and bottom walls of the diffuser.

The bottom wall boundary layer just ahead of the circular arc or supercritical airfoil was removed by a transverse slot across the wall. A valve was installed in the suction piping to regulate the amount of boundary layer that was removed.

To minimize the wall interference effects on the flow field over the airfoil, a variable porosity top wall was installed. By sliding the movable backside of two porous plates while the airside plate remained stationary, it was possible to vary the opening from zero to 10 percent.

A quick-acting pneumatic valve, located downstream from the diffuser section, was used to establish the flow in approximately one second. The static and impact pressures in the test section and over the models were measured by mercury manometers, which had a solenoid valve for each manometer bank. The duration of the test flow, and the recording of the static pressures, and the Schlieren photographs were all controlled by a timer system. Thus, the pressures and the Schlieren photograph were taken simultaneously.

Lucite side walls were installed on the test section, over which were fastened thick aluminum plates with cut-outs to permit the observation of the boundary layer and the shock waves over the airfoils by the Schlieren system. The Schlieren photographs were taken by a camera which was triggered by the timer system used to operate the tunnel. It was possible to take the Schlieren photographs with either a horizontal or a vertical knife edge position.

The impact pressure distributions downstream from the airfoil trailing edge were measured with a narrow cross-sectional rake of 8 impact pressue probes. With this rake it was possible to measure the vertical impact pressures and calculate the upper surface profile drag for the various porosities, cavity depths, and flow Mach numbers.

Investigations of the passive drag control concept were conducted with a 12-percent-thick circular arc and a 14-percent-thick supercritical airfoil, which were placed on the bottom wall of the test section. The porous surface with the cavity beneath it was positioned at the shock wave location at transonic Mach numbers. The porosities of 1.25 and 2.5 percent,over a large and a small cavity, were investigated to determine the optimum size of porosity and cavity.

At transonic speeds, the airfoil porous surface with the cavity beneath it produced a lambda shock wave system consisting of an oblique and a normal shock wave. The oblique shock wave lowered the local Mach number just upstream the normal shock terminating the embedded supersonic region, thus weakening the strength of the normal shock wave. In addition, the circulation of the decelerated flow through the porous surface from the downstream to the upstream terminating shock wave location

lowered the pressure distribution over the downstream region, minimizing the flow separation.

The wake impact pressure surveys showed an appreciably lower impact pressure loss and a drag reduction for the airfoils with the porous surface, with or without a negligible loss in the lift. A higher drag reduction was obtained with 2.5 percent porosity and the small cavity at transonic Mach numbers. At low subsonic speeds where there was no shock wave over the airfoil surface, the porosity increased the drag. To overcome this shortcoming at low Mach numbers, an anticipated solution is to seal the porous surface.

To determine the overall merit of the concept and to apply the idea in future aircraft generations, more development and testing must be done. A full-scale program is also needed to demonstrate that the concept is truly ready for civil and military applications. Such full-scale programs usually involve flight testing, which is beyond our capabilities.

Many economic factors may limit technological development, but the present concept appears to be economically feasible because of its simplicity, and the fact that it needs no additional power to function.

The results of the present research show that such a passive drag reduction concept will be feasible for applications to future aircraft design, since any drag reduction represents either a direct saving in fuel or an increase in performance.

PART 8

LITERATURE CITED

1. D. Nixon, "Design of Transonic Airfoil Sections Using a Similarity Theory," NASA Ames Research Center, Moffeh Field, CA, 17th Aerospace Sciences Meeting, New Orleans, LA/ January 15-17, 1979.

2. N.D. Malmuth, W.D. Murphy, V. Shanker, J.D. Cole, and E. Cumberbatch, "Upper Surface Blown Airfoils in Incompressible and Transonic Flows," AIAA, Vol. 19, No. 12, December, 1981.

3. L. Maestrello, "Initial Results of a Porous Plug Nozzle for Supersonic Jet Noise Suppression," NASA Tech. Memo 78802, Nov. 1978.

4. D. Lee and U. Yashihara, "A Wind Tunnel Investigation of Two Transonic Airfoil Concepts," USAF Flight Dynamics Laboratory, Dept. No. AFFDL-TM-77-51, May, 1977.

5. S.P. Wilkenson, "An Experimental Investigation of a Turbulent Boundary Layer with Suction Through Closely Spaced Streamwise Slots," Old Dominion University Report, NASA Grant NCR-47-003-052, 1978.

6. A.H. Nayfeh and N.M. El-Hady, "An Evaluation of Suction Through Porous Strips for Laminar Flow Control," Virginia Polytechnic Institute and State University, Blacksburg, VA, AIAA 12th Fluid and Plasma Dynamics Conference, July 23-25, 1979/ Williamsburg, Virginia.

7. M. Nandanan, E. Stanewsky, and G.R. Inger, "Airfoil-Flow Analysis with a Special Solution for Shock/Boundary-Layer Interaction," AIAA, 80-1389R, Vol. 19, No. 12, December, 1981.

8. Rachel Gordon and Josef Rom, "Transonic Viscous-Inviscid Interaction Over Airfoils for Separated Laminar and Turbulent Flows," AIAA, Vol. 19, No. 5, May, 1981.

9. K.P. Burdges, "Experimental Measurements of Shock/Boundary Layer Interaction on a Supercritical Airfoil," Lockheed-Georgia Co., Marietta, GA, AIAA 12th Fluid and Plasma Dynamics Conference, July 23-25, 1979/ Williamsburg, Virginia.

10. F.W. Spaid and W.D. Bachalo, "Experiments on the Flow About a Supercritical Airfoil Including Holographic Interferometry," Journal of Aircraft, Volume 14, No. 4, April, 1981.

11. "Investigation of Passive Shock Wave/Boundary Layer Control for Transonic Airfoil Drag Reduction," 1st Annual Report for the Period October 1, 1979 to September 30, 1980, NASA Grant No NSG-1624,

NASA Langley Research Center.

12. Charles D. Harris, Robert J. McGhee, and Dennis O. Allison, "Low-Speed Aerodynamic Characteristics of a 14-Percent-Thick NASA Phase 2 Supercritical Airfoil Designed for lift Coefficient of 0.7," December, 1980, NASA TM 81912.

13. Scott K. Marble, "Transonic Wind Tunnel Blockage Minimization Using a Variable Porosity Plate," Master Thesis, R.P.I., May 1981

14. G.E Bartlett and J.W. Peterson, " Wind Tunnel Investigation of a Double Wedge Airfoil at Subsonic Speeds," Report No. AF. 360-A-6, Cornell aeronautical Laboratory, August, 1946.

15. J.B. Caroll and C.F. anderson, "Boundary-layer Effect on Local Mach Number Measurements on a Circular Arc Half Profile," Jour. of Aero. Sci., Vol. 25, pp. 603-605, June, 1956.

16. H.W. Liepmann,"The Interaction Between the Boundary Layer and Shock Waves in Transonic Flow," Jour. of Aero. Sci., Vol. 13, pp. 623-638, Dec. 1946.

17. Charles D. Harris,"Aerodynamic Characteristics of the 10-Percent-Thick NASA Supercritical Airfoil 33 Designed for a Normal-Force Coefficient of 0.7," NASA TM X-72711, February, 1981.

18. Charles D. Harris,"Aerodynamic Characteristics of a 14-Percent-Thick NASA Supercritical Airfoil Designed for a Normal-Force Coefficient of 0.7," NASA TM X-72712, February, 1981.

19. Frances Bauer, Paul Garabedian, David Korn, and Antony Jameson, "Supercritical Wing Sections II," Volume 108 of Lecture Notes in Economics and Mathematical Systems, Springer-Verlag, 1975.

20. H.T Nagamatsu, R.E. Geiger, and R.E. Sheer, Jr.,"Hypersonic Shock Tunnel," Am. Rocket Soc. Jour., Vol. 29, pp. 332-338, 1959.

21. K. Tuzla, D.A. Russel, and J.C. Wai,"Effect of Specific Heat Ratio on Two-Dimensional Transonic Aerodynamics," AIAA, Vol. 18, pp. 1025-1026, September, 1980.

22. Ames Research Staff,"Equations, Tables, and Charts for Compressible Flow," NACA TR 1135, 1953.

23. G.Y. Nieuland, B.M. Spee,"Transonic Airfoils: Recent Developments in Theory, Experiment, and Design," Amsterdam, Netherland, 1973.

24. Liepmann and Roshko,"Elements of Gasdynamics," John Wiley & Sons, Inc., New York, 1957.

25. R.C. Pankhurst and D.W. Holder,"Wind-Tunnel Technique," Sir Isaac Pitman & Sons Ltd., London, p.276, 1965.

26. Hermann Schlichting,"Boundary Layer Theory," McGraw-Hill Book Co. Inc., 1960.

27. J. Scheiman and J.D. Brooks,"Comparison of Experimental and Theoretical Turbulence Reduction from Screens, Honeycomb, and Honeycomb-Screen Combinations," Journal of Aircraft, Vol. 18, No. 8, August, 1981.

28. J.L. Jacocks,"Aerodynamic Characteristics of Perfored Walls for Transonic Wind Tunnels," ARO Inc., AEDC-TR-77-61, June, 1977.

29. R.W. Barnwell,"Design and Performance Evaluation of Slotted Walls for Two-Dimensional Wind Tunnels," NASA TM 78648, Feb. 1978.

30. R.W. Barnwell,"Similarity Rule for Side Wall Boundary-Layer Effect in Two-Dimentional Wind Tunnels," AIAA Jour., Vol. 18, pp.1149-1151, Sept. 1980.

31. B. Satyanarayana, E. Schairer, and S. Davis,"Adaptive-Wall Wind-Tunnel Development for Transonic Testing," Journal of Aircraft, Vol. 18, No. 4. March 1980.